Geophysical Surveys in the Blue Nose Mine Area, Patagonia Mountains, Arizona

Geophysics Field Camp 2019

Laboratory for Advanced Subsurface Imaging

LASI-19-1

May 12, 2019

Osvaldo S. P. Bambi, Ryan K. Brock, Elsa D. Domingos, Figueiredo C. K. Evaristo, Kenneth C. Gourley, Michael T. Hanna-Wilson, Miguel Alberto Kilezi, Tyler S. Kuehn, Echo Li, Ivo Lima, Richard Marcelain, Rui T. Mariamba, Jonas Joaquim Mulato, Charles K. Nault, Lucas M. Pedro, Venancio Fernando J. Pedrosa, Sean P. M. Purdy, Farid Najmi Rosli, Brianna Rupkalvis, Nicholas R. Shea, Ben K. Sternberg

Abstract

The US Geological Survey and the US Forest Service requested an investigation of the sediment and groundwater properties of the Blue Nose Mine in the Patagonia Mountains of southern Arizona to help with future remediation efforts due to historical mining of the area. Information on the depth of the existing tailings piles was also requested to aid in determining the best removal strategy. The surveys carried out in this investigation include direct current (DC) resistivity, transient electromagnetics (TEM), EM-31 and EM-38, total-field magnetism, and petrophysical laboratory analysis. The 20m TEM loop and DC resistivity data revealed low-resistivity regions, less than 10 Ohm-m, surrounded by several-thousand Ohm-m resistive features, indicating a large conductive zone around the existing mine workings. The 10 m TEM loops, as well as the EM-31, and EM-38 data, collected on the tailings piles indicate a conductive layer reaching 8 m in depth from the surface. These help to delineate the conductive tailings material from the surrounding hillside. The total-field magnetic survey was useful in determining several linear features and magnetic trends, including the Harshaw Creek Fault on the eastern edge of the study site. The petrophysical analysis aimed to help refine subsurface interpretations, but due to the small sample size only provides a limited correlation to the DC resistivity and TEM data. Correlations between magnetic and resistive datasets reveal three zones with differing electromagnetic properties, one of which may correlate with the Blue Nose ore deposit.

Table of Contents

Acknowledgements

The University of Arizona Field Geophysics class (GEN/GEOS 416/516), would like to thank the United States Geological Survey (USGS) for providing funding and support for this project. Jamie Macy has played a vital role in our Geophysics Field classes for many years, providing the required equipment, teaching us how to operate the equipment, and processing the data. We would like to thank Floyd Gray from the USGS for giving us a detailed introduction to the area and the project before our first weekend in the field. Without the assistance of the USGS this project would not have been possible. Finally, we would like to thank Zonge International for their 33 years of support of this class as well as providing relevant information for the report and presentation.

1. Introduction

1.1 History

The Blue Nose Mine resides within the Bisbee Formation and was a former underground and small surface mine located on the west side of Harshaw Creek, about 10 km south of Patagonia, AZ and 25 km northeast of Nogales, AZ. The mine had four previous owners and was operated on-and-off from 1884 to 1956. The mineralization in the area is primarily composed of pockets of argentiferous galena and other sulfides. These are located in a northwest-trending fault zone in Jurassic-Triassic volcanic rocks interbedded with limy, siliceous sediments (Mindat, 2015). The limestone contains intrusive lenses of rhyolite, which has small crystals of pyrite and chalcopyrite with white, talc-like ore pockets. The vein dips 40° to the northwest and was mined to a depth of about 60 m with tunnel operations totaling 440 m in length (Schrader and Hill, 1915).

1.2 Project Background

The U.S. Geological Survey, in cooperation with the U.S. Forest Service, is undertaking a study on the environmental effects of historical mining on the current water and sediment properties. This study is focused on the Harshaw Creek watershed, upstream of Patagonia, AZ, which is in the vicinity of Blue Nose Mine. The removal of the tailings piles from Blue Nose Mine is also of concern. This study was set in motion because of the observation of bright orange sludge discharge from mines within the area after strong, monsoon-related precipitation in September of 2014 (Figure 1.1).

The University of Arizona, in conjunction with the USGS, conducted a field study during the days of February 9, 10, 16, and 17 of 2019. Data were collected 300 m from the main entrance of Blue Nose Mine to the southwest and approximately 270 m from a creek adjacent to the tailings plies. During these days, subsurface measurements were performed using the TEM (transient electromagnetic), DC (direct current) resistivity, ground conductivity (EM-31/38), and total field magnetic methods. The primary objective of this report is to compile geophysical data on the

area for the identification of fracture networks. These networks may transport water into the Harshaw Creek watershed from naturally occurring deposits and the tailings piles, because they lead directly to Harshaw Creek. The results from this study will give a better understanding of the subsurface properties of the mine, allowing for a more informed response in reducing possible discharge recurrence.

Figure 1.1. Pictures of orange precipitate discharge from tailing piles around the Patagonia Mountains, AZ in September of 2014 after a monsoon. Photos courtesy of Glen E. Goodwin.

1.3 Geologic Background

A geologic map of the Patagonia Mountains (Figure 1.2) is reproduced from Vikre et al. (2014). Blue Nose Mine is located within the Cretaceous Bisbee Formation which overlies Jurassic – Triassic volcanic and sedimentary rocks. In addition, we saw lenses of rhyolite dikes flare out at the surface at points that could correlate to the Laramide batholith that more noticeably exists in other portions of the Patagonia mountains. The mine also exists within the intersection of the Harshaw Creek and Blue Nose faults to the East and West, respectively. This faulting and fracturing allowed hydrothermal water to travel through the subsurface and mineralize sulfide deposits, as the mine exists within the intersection of pyrite and shear zones.

1.4 Hydrology and Heavy Metal Concentrations

Inactive and abandoned mines, once rich in mineral and ore deposits, now have emerging safety, health, and environmental risks. These include heavy metal contamination of groundwater, surface water, and soils. This geophysical investigation focused heavily on mineralogical, geologic, and hydrologic effects caused by mining. Emerging hydrologic questions include (1) whether or not contaminants are leaching into the groundwater; (2) whether or not they are contaminating the groundwater source; and (3) whether or not contaminants are being transported in surface runoff. By examining the groundwater and surface water conditions, the impacts from this abandoned mine can be examined and possibly remediated in the future.

Mountain terrains occupy 20% of the Earth's land surface, and their hydrologic characteristics are defined by fractures and faults. Surface water elevation in these regions are dependent on lower hydraulic conductivity, nested flow systems, and ephemeral streams with abundant losing reaches. With limited access to the subsurface, certain geologic structures limit groundwater flow between aquifers, increase seepage, and produce higher streamflow (Garfias, 2009; Ball et al., 2014). Any regional increase in precipitation can lead to drastic runoff and stream discharge in Harshaw Creek, especially with rising water heights within the Patagonia Mountains.

In 1915, the Blue Nose Mine had an estimated 60 m depth to groundwater (Schrader and Hill 1915). Over the next 100 years, the groundwater elevation changed due to well installation, pumping, climate, and changing surface conditions. Water levels, based on the Arizona Department of Water Resources (ADWR) Wells 55 Registry, were interpolated using kriging (Figure 1.3) and inverse distance weighted spatial analysis. Based on these analyses, the current level at the Blue Nose Mine Site is approximately 25 m below the surface (Figure 1.4). Floyd Gray at the USGS approximated the water level at an abandoned shaft to be 22 m below the surface. The ADWR also provides Groundwater Site Inventory (GWSI), which uses water levels from the Hydrology Division's Basic Data Section, the USGS, and other agencies. A GWSI livestock well, located approximately 5 m from the northeast extent of the field survey, observed 7 m depth to water on December 10, 1987 (Figure 1.5). Another GWSI well, located in the

central Cienega Creek Groundwater Basin, had a 5% difference between modeled and observed water levels in 2016 (Figure 1.6). Continuous distributions of water between measured points are assumed for the calculated model. A spatial correlation matrix was used to analyze the interpolated water levels and the 5 m digital elevation model (DEM) raster from the USGS (Figure 1.7). The matrix gave a correlation of -0.53, implying that elevation and water levels have a moderately negative relationship in the Cienega Creek Basin. The interpolation does not account for the complex geology at this site. Thus, the geophysical survey will improve on the simple geometric shape assumption of the aquifer.

The Blue Nose Mine lies within the Santa Cruz watershed in southeastern Arizona (Figure 2.3). Harshaw Creek, one of the primary tributaries of the Santa Cruz River, is the nearest alluvial system to the mine. The study site has a long history of mining activity which has produced moderate concentrations of heavy metals including antimony, cadmium, cobalt, chromium, copper, iron, lead, manganese, molybdenum, and zinc (Eddleman, 2012). Included in this report are modern concentration samples of aluminum (Figure 1.8) and cadmium (Figure 1.9). At 20°C, aluminum has a resistivity of 2.82×10^{-8} ohm-m and a conductivity of 3.5×10^{7} S/m. At 20°C, cadmium has a resistivity of 6.84×10^{-8} ohm-m and a conductivity of 1.46×10^{7} S/m. An understanding of the hydrological and geochemical processes that resulted in the mineralization, transport, and infiltration of these heavy metals into the soil, as well as their effect on the subsurface conductivity, will lead to a better understanding of geophysical data retrieved at the study site.

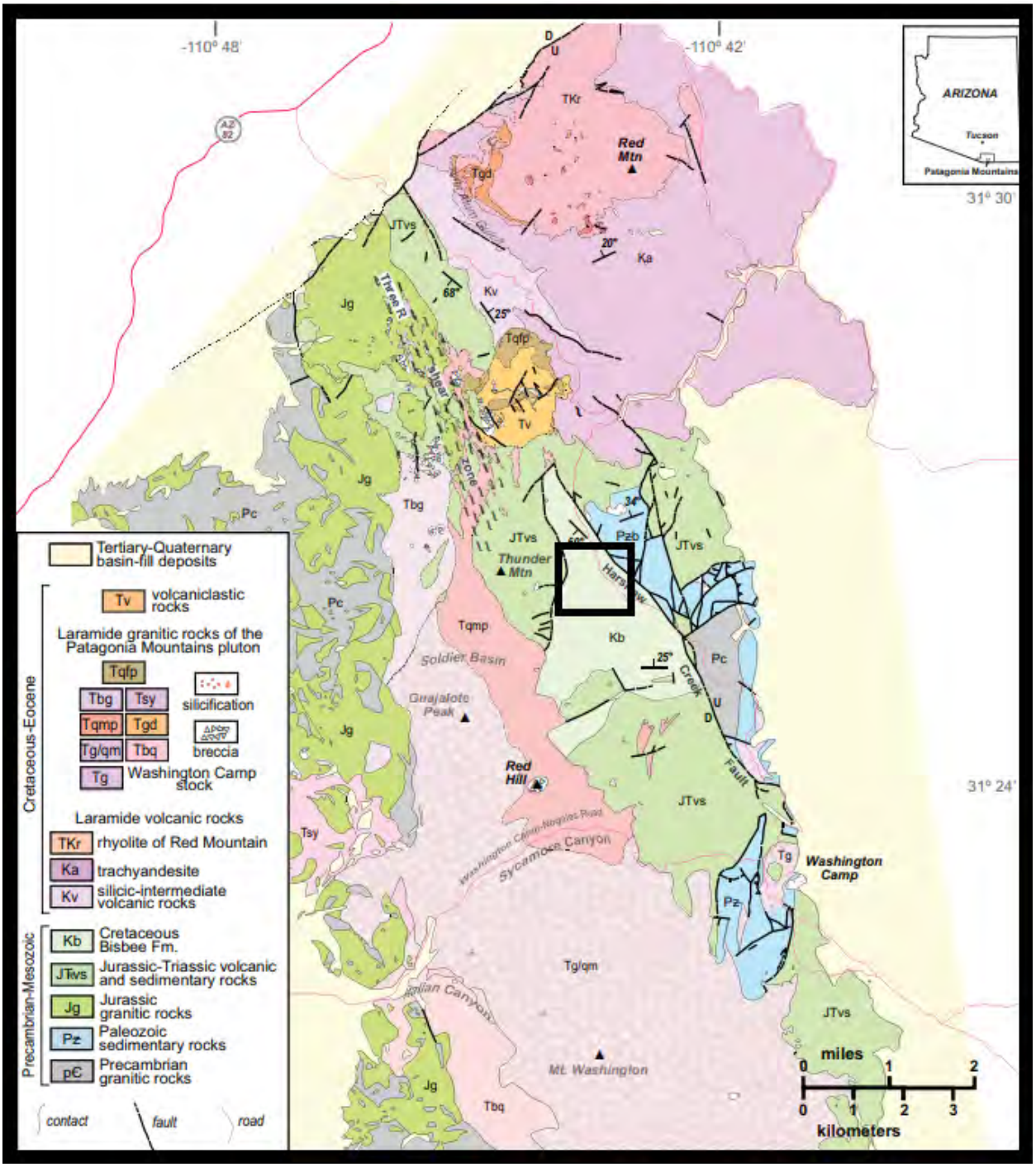

Figure 1.2. Geologic map of the northern Patagonia Mountains. Inset square shows location of study area. Modified from Vikre et al., (2014).

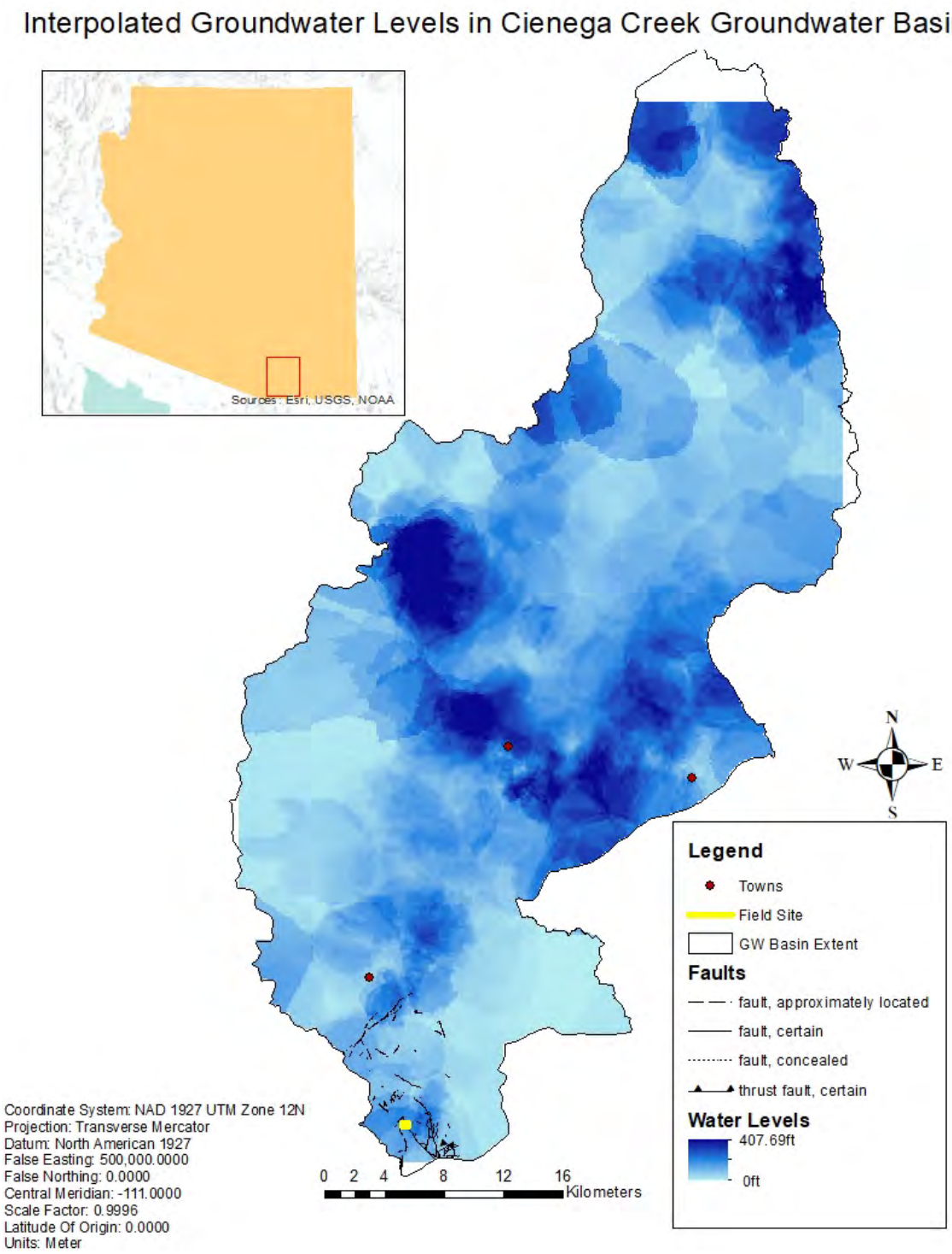

Figure 1.3. Interpolated depth to groundwater levels (ft) using kriging. Water level data was obtained from the ADWR Wells 55 Registry.

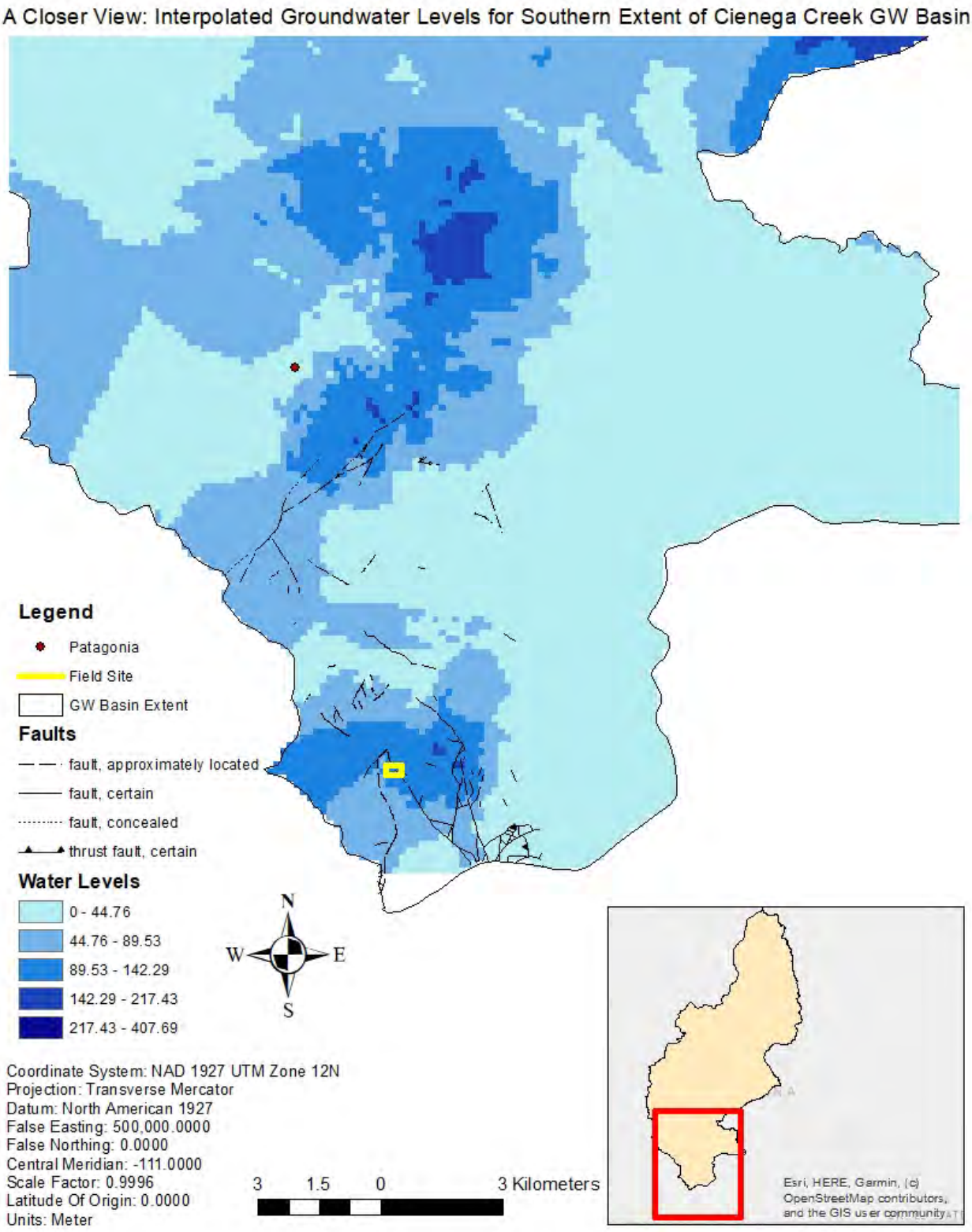

Figure 1.4. Same as Figure 1.3, but zoomed into the study area.

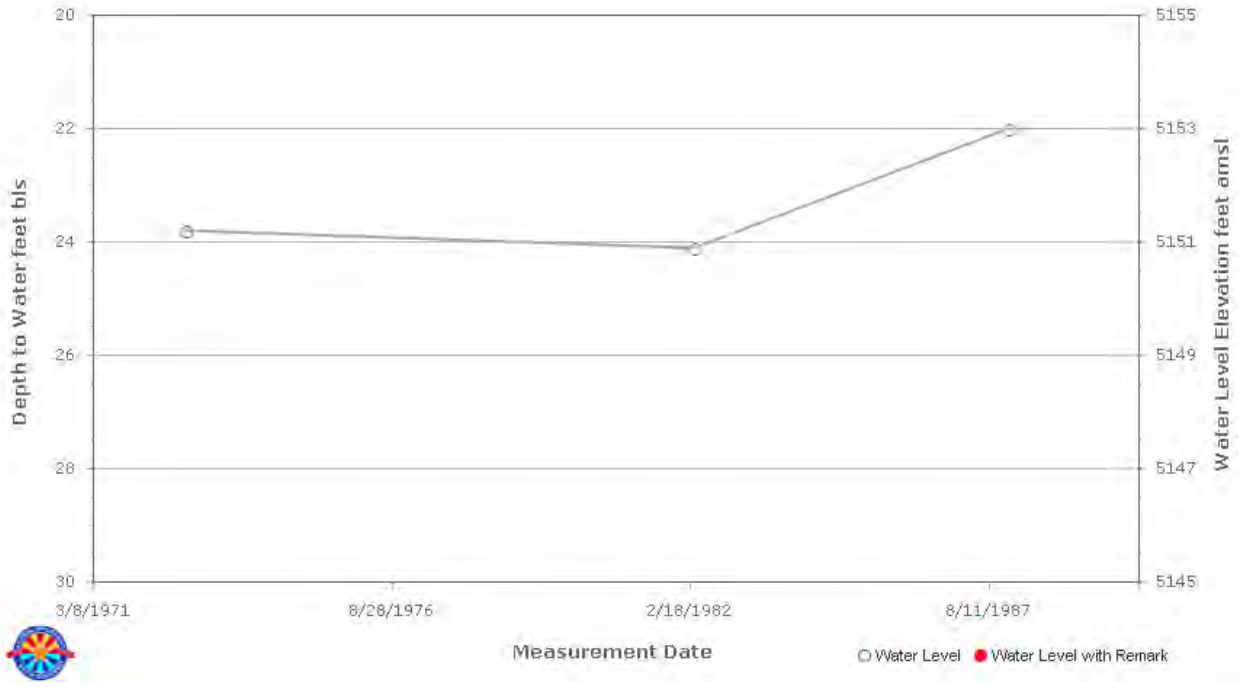

Figure 1.5. Hydrograph for GWSI well 637238, which is one of the closest wells to the field site.

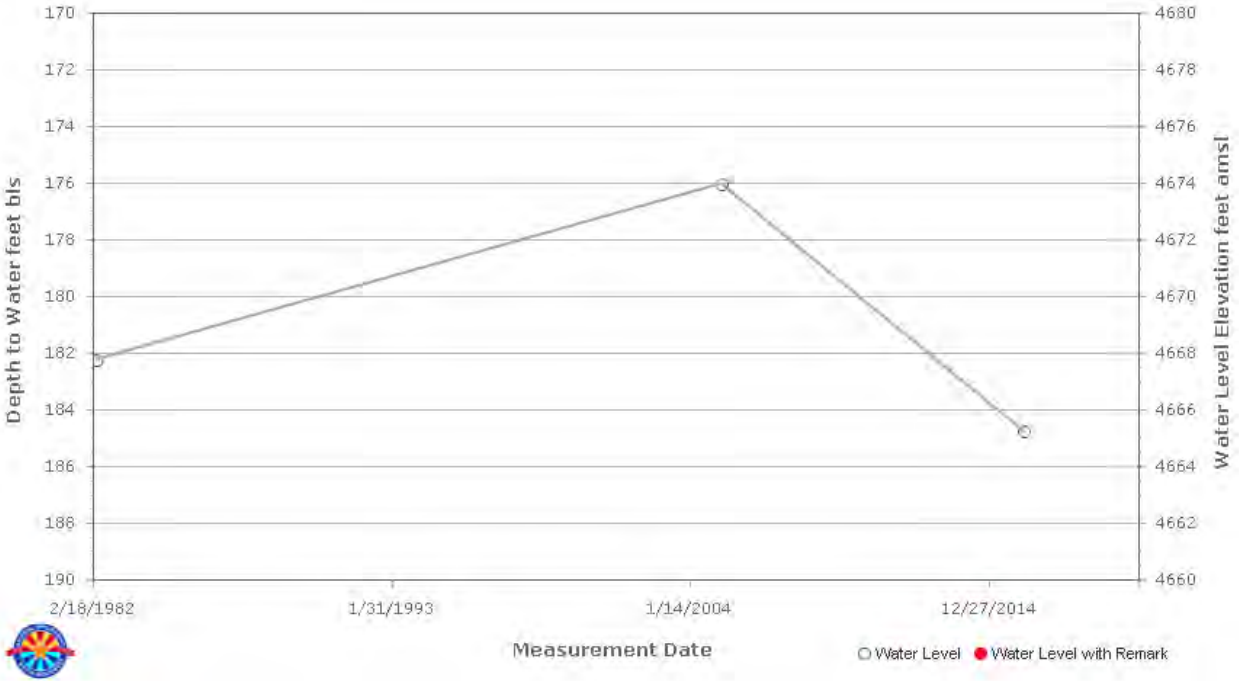

Figure 1.6. Hydrograph for GWSI well 604551, which is one of the closest wells to the field site.

STATISTICS of INDIVIDUAL LAYERS

Layer	MIN	MAX	MEAN	STD
1	0.0000	407.6904	78.8134	59.9787
2	1050.7981	2867.9238	1473.0584	184.4491

COVARIANCE MATRIX

Layer	1	2
1	1791.94323	-3574.30035
2	-3574.30035	-24998.88845

CORRELATION MATRIX

Layer	1	2
1	1.00000	-0.53403
2	-0.53403	1.00000

Figure 1.7. Statistical analysis of the interpolated water levels from ADWR (layer 1) and 5 m DEM from the USGS (layer 2). The correlation matrix between the two raster layers indicates a moderately negative relationship between water level and elevation.

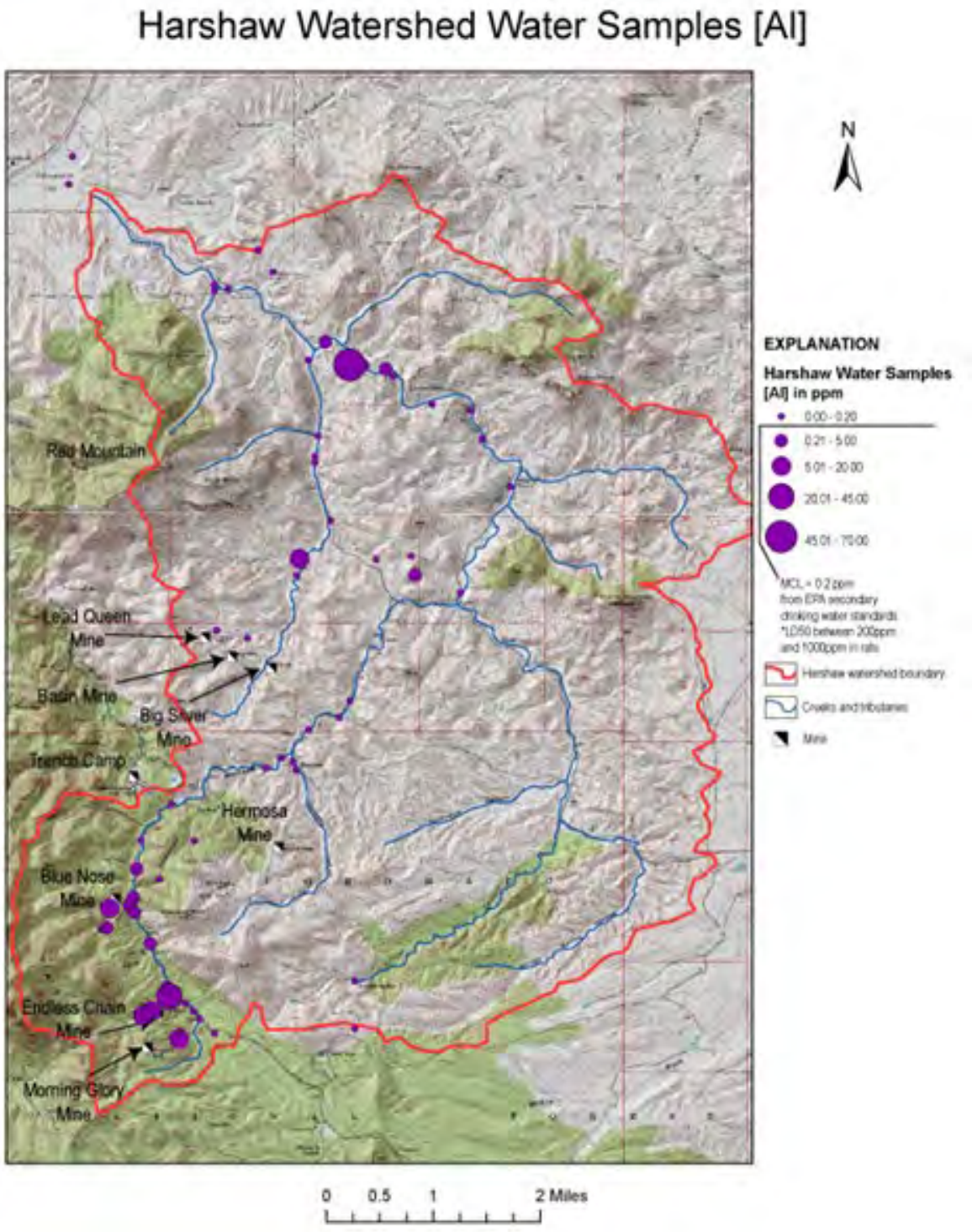

Figure 1.8. Map of Harshaw Watershed samples tested for aluminum concentration. Blue Nose mine is located at the bottom left of the figure. Courtesy of Floyd Gray (USGS).

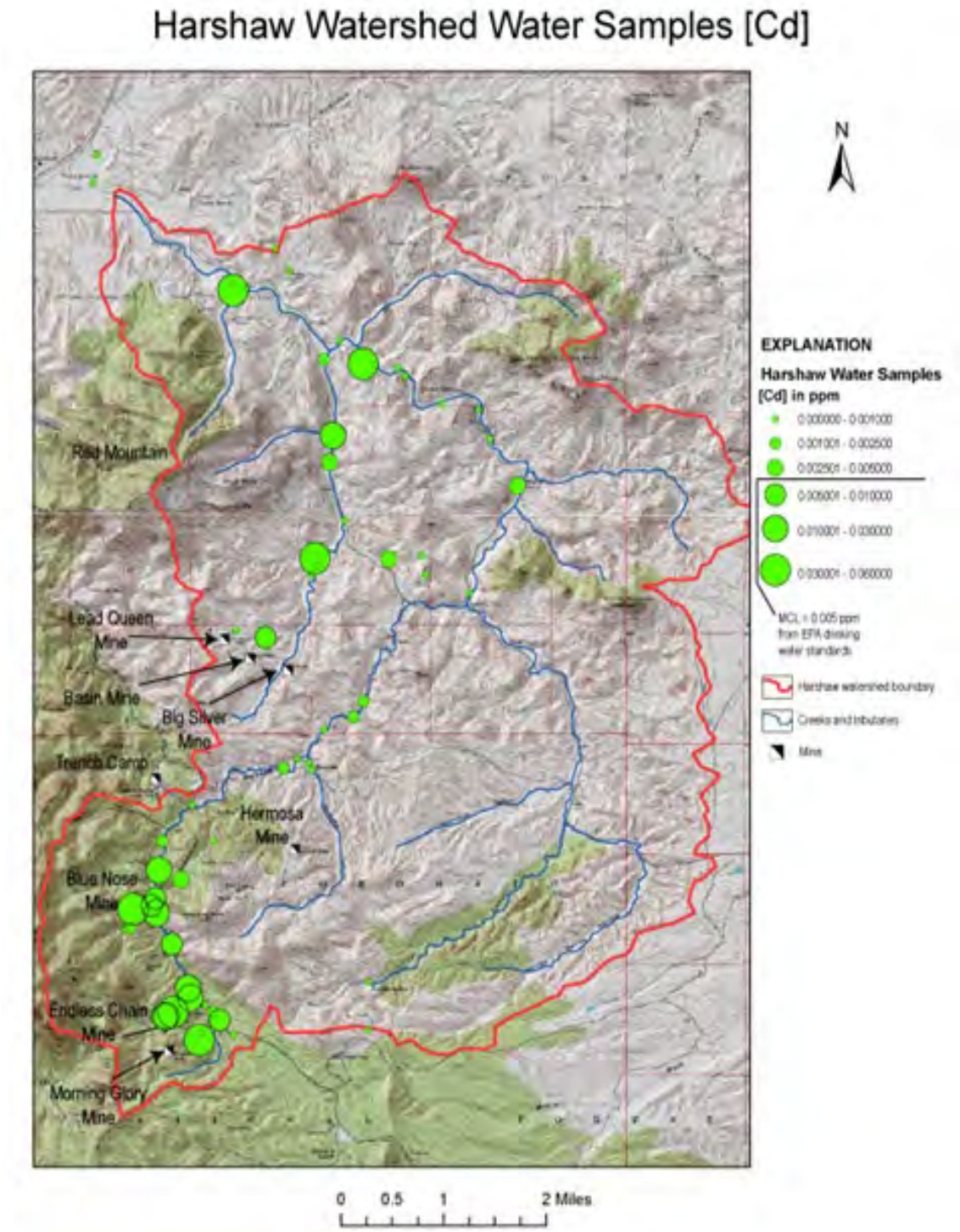

Figure 1.9. Map of Harshaw Watershed samples tested for cadmium concentration. Blue Nose mine is located at the bottom left of the figure. Courtesy of Floyd Gray (USGS).

1.5 References

Ball, L.B., Caine, J.S., and S. Ge, 2014, Controls on groundwater flow in a semiarid folded and faulted intermountain basin, Water Resources, **50**, 6788-6809.

Eddleman, K., 2012, Bioaccumulation of heavy metals from soils to plants in watersheds contaminated by acid mine drainage in SE Arizona, Unpublished Master's Thesis, The University of Arizona, Tucson, Arizona.

Garfias, J., 2009, Groundwater in mountain regions, In Groundwater: Vol. I, EOLSS Publishers, Oxford, UK.

Mindat, 2015, Blue Nose Mine (Abe Lincoln Mine; War Horse Mine; Big Chief Mine; Big Jim Mine; Blue Nose Extension Mine; Home Again Virginia Hay claims), Harshaw, Harshaw District, Patagonia Mts, Santa Cruz Co., Arizona, USA, https://www.mindat.org/loc-33875.html, accessed April 15, 2019.

Schrader, F.C. and J.M. Hill, 1915, Mineral deposits of the Santa Rita and Patagonia Mountains, Arizona, USGS Bulletin 582, 278-279 & 373.

Vikre, P.G., Graybeal, F.T., Fleck, R.J., Barton, M.D., and E. Seedorff, 2014, Succession of Laramide magmatic and magmatic-hydrothermal events in the Patagonia Mountains, Santa Cruz County, Arizona, Economic Geology, **109**, no. 6, 1667–1704.

2. Location Maps and Elevation Profiles

2.1 Geographic Location Information

The overall location of the study area is shown in Figure 2.1. Location data for each geophysical method station was collected using Garmin 64st GPS units. Proper headings for each line survey were maintained using each GPS unit's internal compass. The recorded coordinates were imported into ArcMap and Google Earth Pro in order to facilitate georeferencing. The UTM coordinates fall within zone 12R with the range of eastings 0525350 to 0525750 and northings 3479250 to 3479500.

2.2 Elevation Data

The elevation of the field site and surrounding area is seen in Figure 2.2. Elevation data came from four different sources: multiple Garmin 64st GPS units, a Nikon Forestry Pro laser rangefinder, Google Earth Pro, and the Shuttle Radar Topography Mission (SRTM). While the Garmin GPS tended to be largely unreliable for accurate elevations, Google Earth Pro, the SRTM data and the laser rangefinder proved more dependable. Elevation profiles from all four sources are provided.

2.3 Geophysical Survey Locations

Thirteen TEM loops, 20m on each side, were laid roughly East to West with a 235º/55º trending azimuth for Line 1 (Figure 2.4). Five TEM loops, 10m on each side, were laid over the tailings piles, roughly East to West for Line 2 (Figure 2.5). This adds up to around 5200m^2 of study area for Line 1, and 500m^2 of study area for Line 2. In order to avoid excessively steep terrain and minimize the disruption of ground vegetation, some of the loops were shifted off the center axis of each line.

There were two DC Resistivity lines, Line 1 and 2, that were parallel to each other and 280m in length (Figure 2.6). Each line consists of 28 electrodes, each spaced 10m apart, the true locations of which are plotted as red dots in Figure 2.6.

EM-31 and EM-38 surveys consisted of two lines above the tailings piles, one (Line 1) running roughly East to West, the other (Line 2) running roughly North to South (Figure 2.7).

The total field magnetic survey consisted of ten East to West lines of measurements, each line consisting of twenty-two stations, making for 220 data points (Figure 2.8). Almost every data point is evenly spaced 15m apart, except where rough terrain required a station to be shifted. This survey covers over 3150m^2, which is most of the field area.

2.4 Location and Elevation Error

The Garmin 64st GPS unit has a positional accuracy of up to 3.09m over a 60s average (US Forest Service, 2017), but elevation readings can have much higher errors. Comparing the GPS unit data to that from Google Earth Pro, elevation at DC Resistivity Line 1 is consistently lower in measurements from Google Earth Pro (Figure 2.11). For DC Resistivity Line 2, the GPS units show consistently lower elevations (Figure 2.12). Elevations for the TEM Loops are similar for both the GPS units and Google Earth Pro. The maximum difference for the 20m TEM Loops is at 70m: Google Earth Pro shows an elevation about 10m higher than the GPS measurements (Figure 2.9). The elevation measured by the GPS units is very similar to that from Google Earth Pro for the 10m TEM loops (Figure 2.10). Elevations measured at both lines for EM-31/38 are very similar. On Line 2, elevation measurements from the two sources follow the same trend, but measurements from the GPS units are always about 5-10m lower than those from Google Earth Pro (Figure 2.14). It is important to note that on Line 1, GPS unit measurements fluctuate a lot, but they are close to the measurements from Google Earth Pro (Figure 2.13).

Figure 2.1. Overview map of the Blue Nose Mine site, located south of Patagonia, Arizona, as shown in the red circle. Reproduced from Patagonia Alliance (2016).

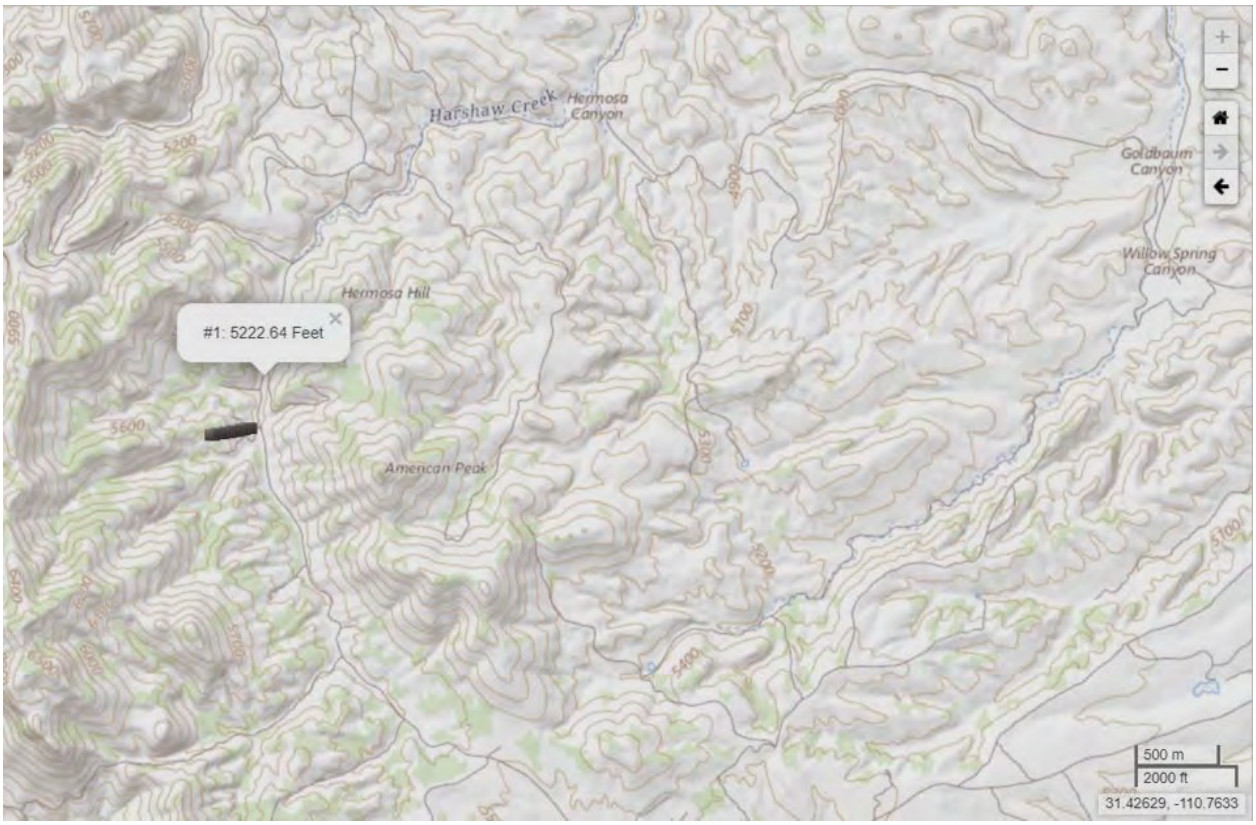

Figure 2.2. Regional elevation map of the Patagonia Mountains. Field site is marked by black rectangle.

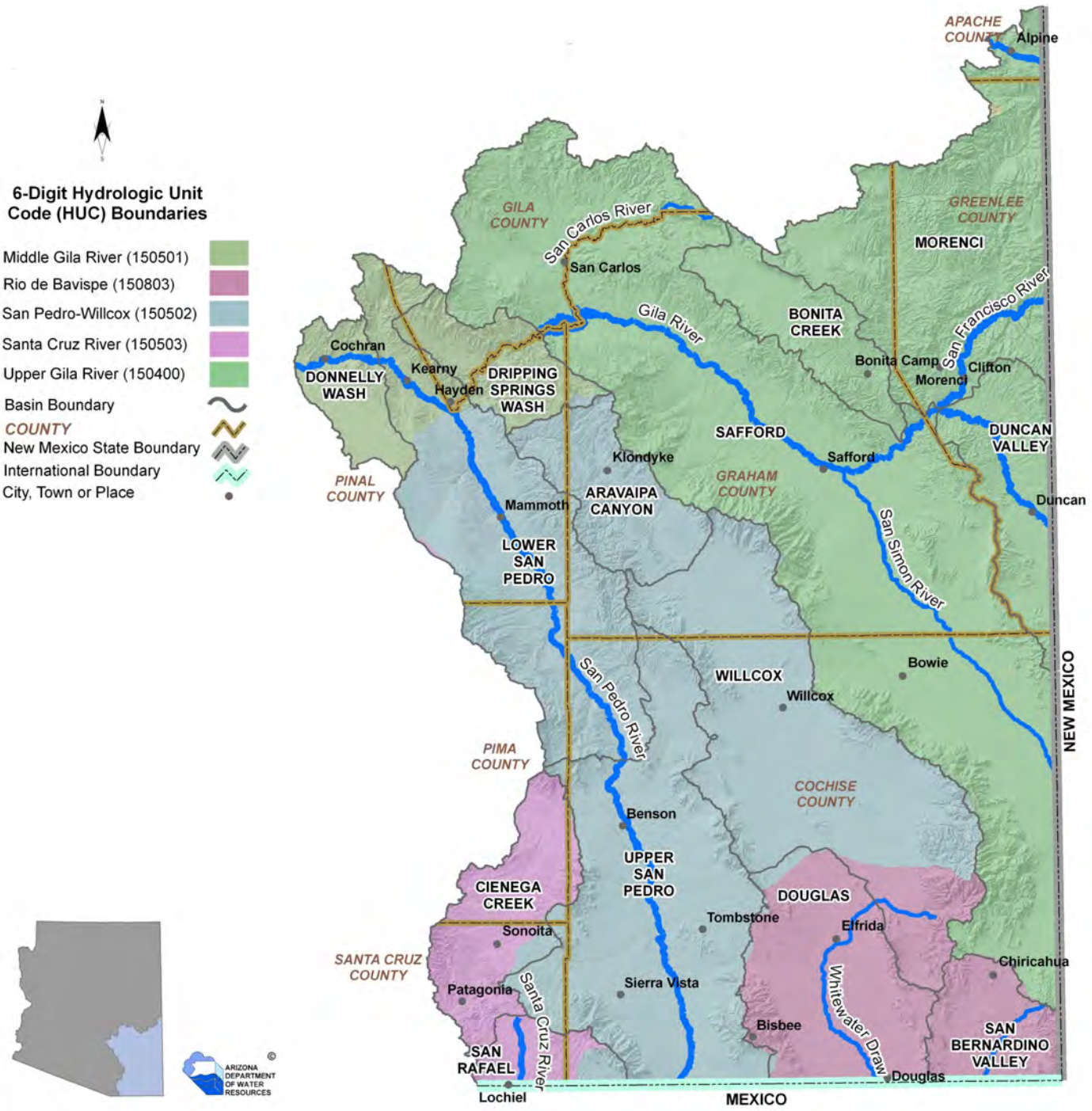

Figure 2.3. Map of southeastern Arizona watersheds. The study area lies within the Santa Cruz watershed (bottom left corner), which consists of the San Rafael Basin, Santa Cruz River, and its tributaries.

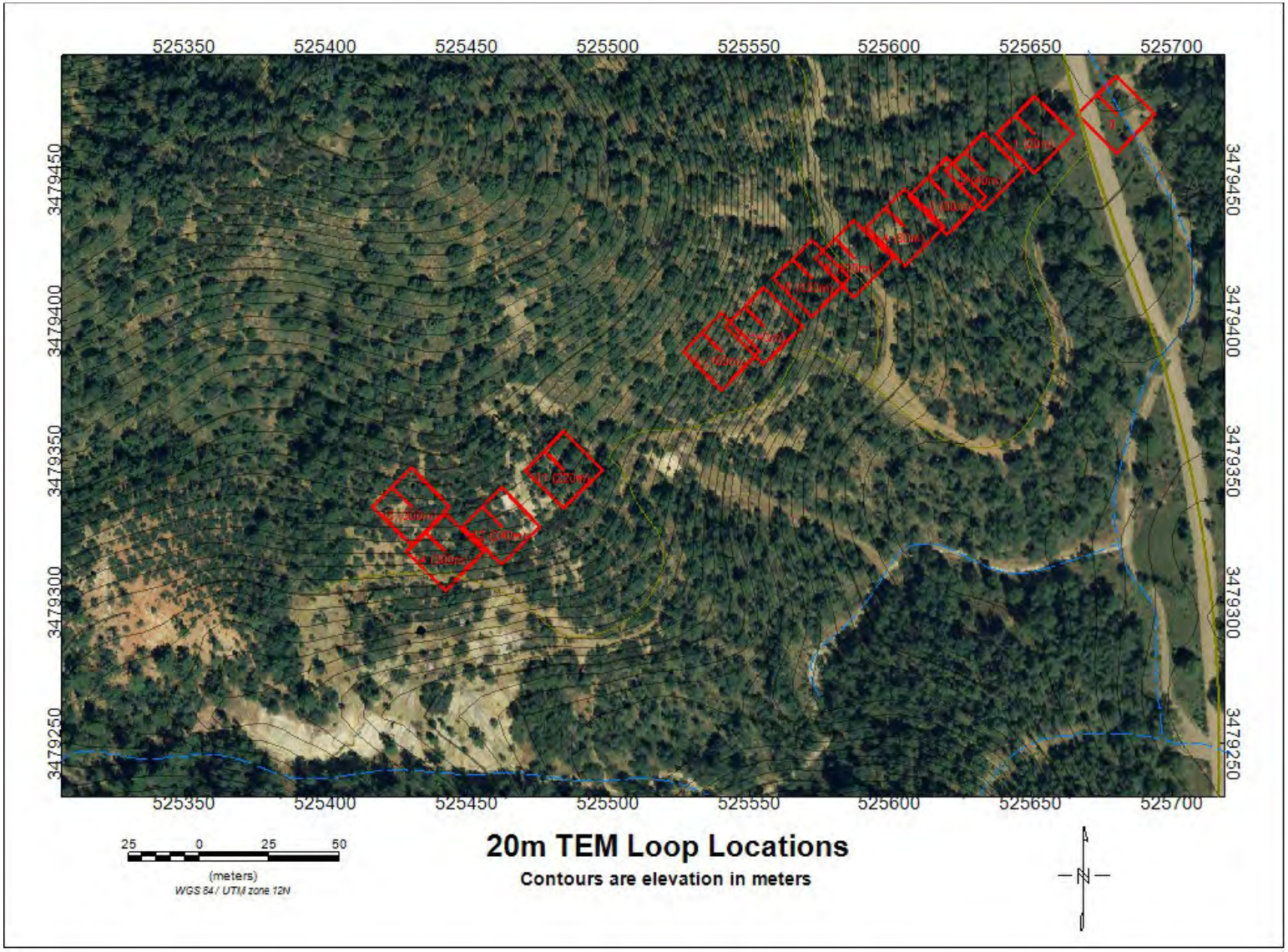

Figure 2.4. Location map for the 20m TEM loops along Line 1. Note that Loop 15 was not used in the inversion modeling.

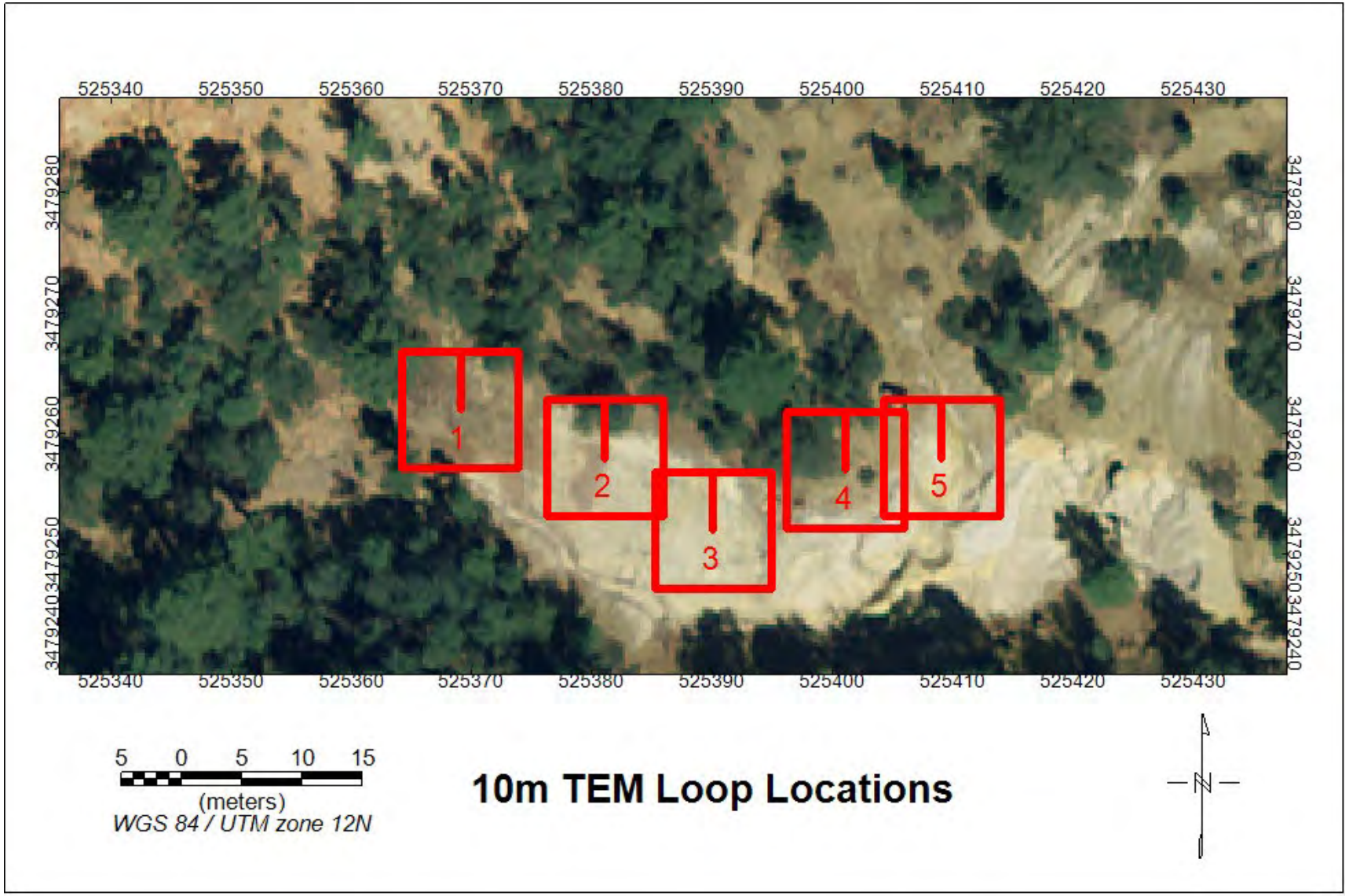

Figure 2.5. Location map for the 10m TEM loops along Line 2 on the surface of the tailings piles. Note that Loop 5 was not used in the inversion modeling.

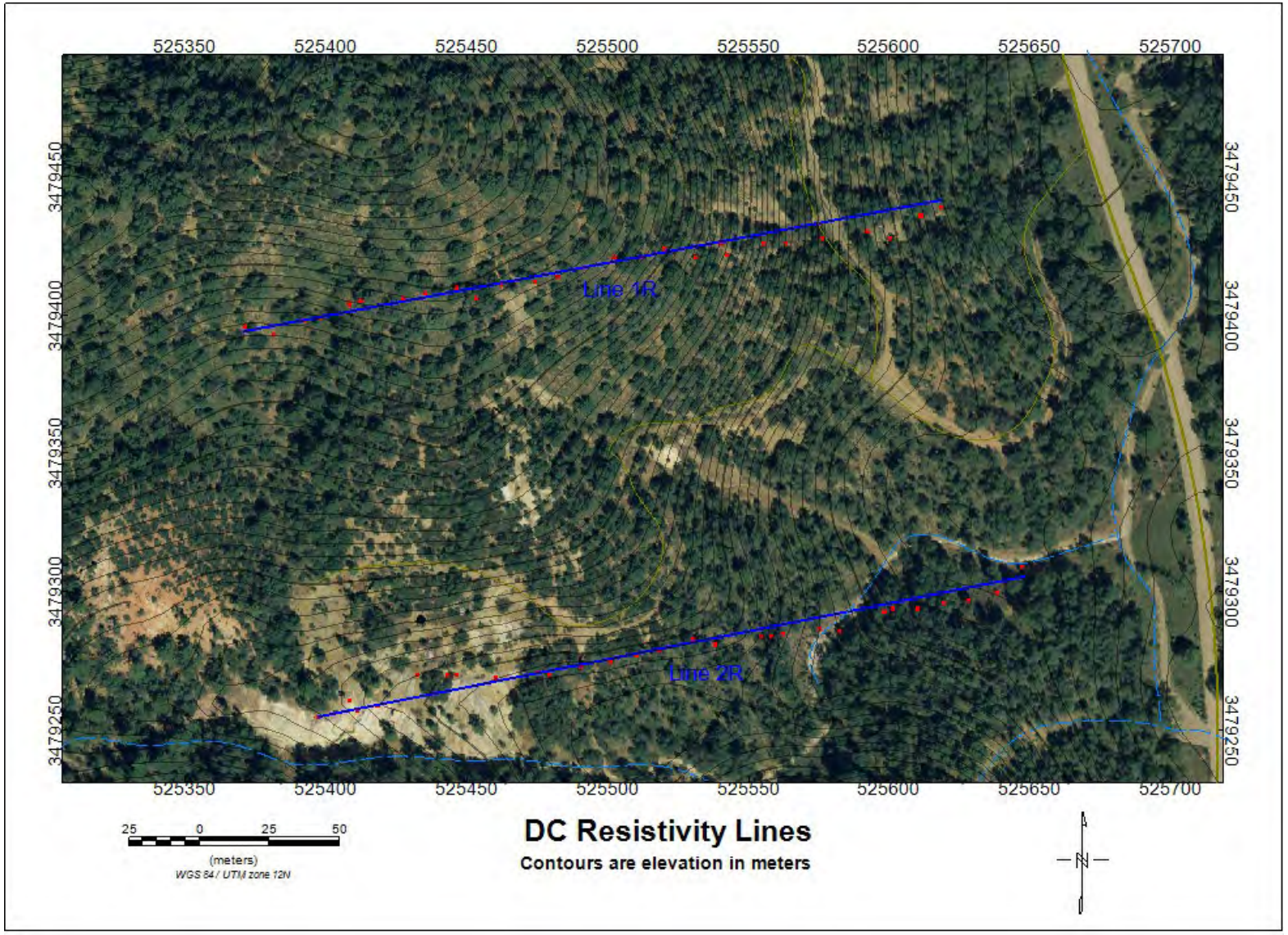

Figure 2.6. Location map showing the DC resistivity lines in blue. The red data points are GPS locations collected at each electrode.

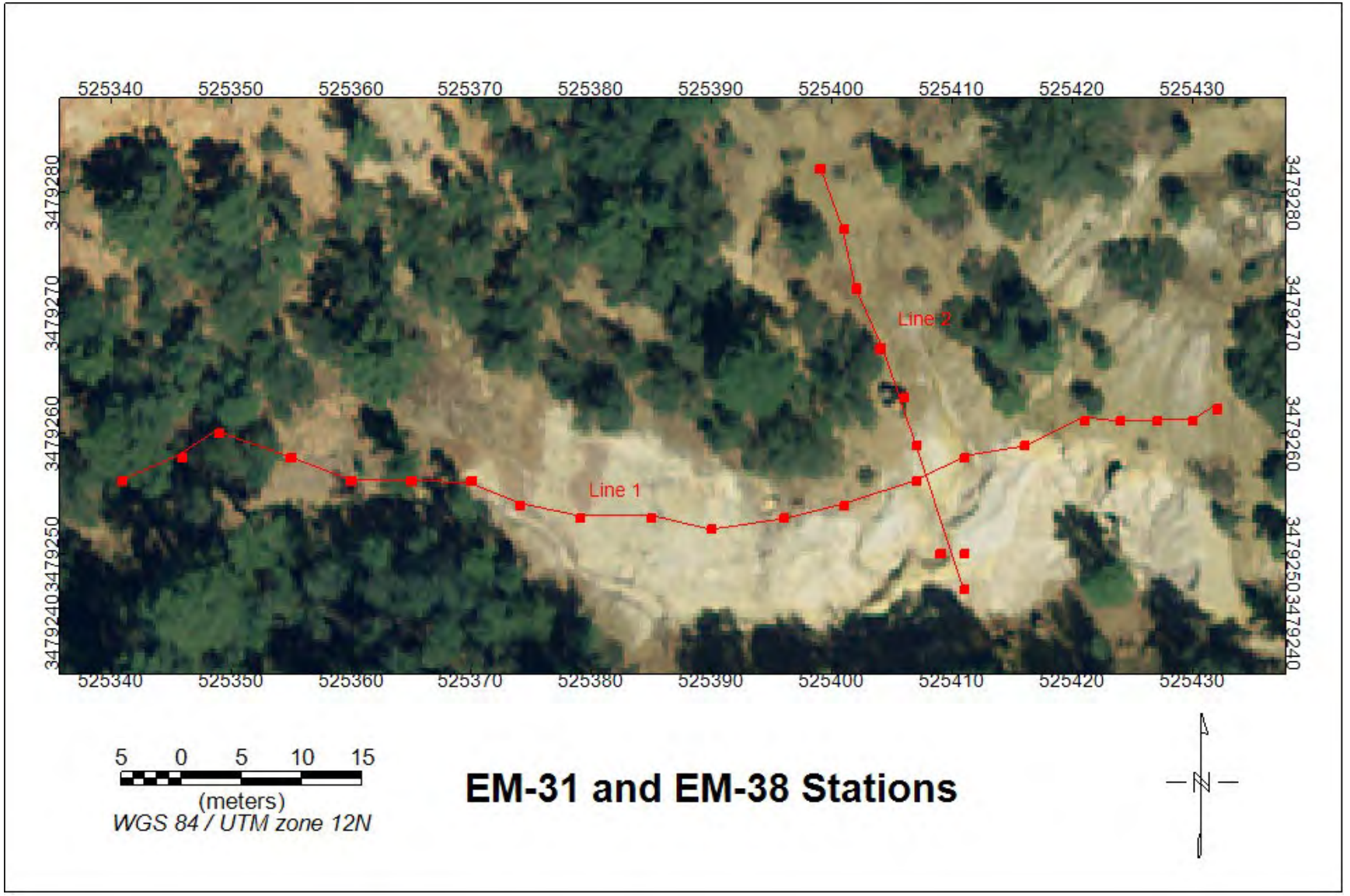

Figure 2.7. Location map of the tailings area showing the EM-31 and EM-38 data collection points.

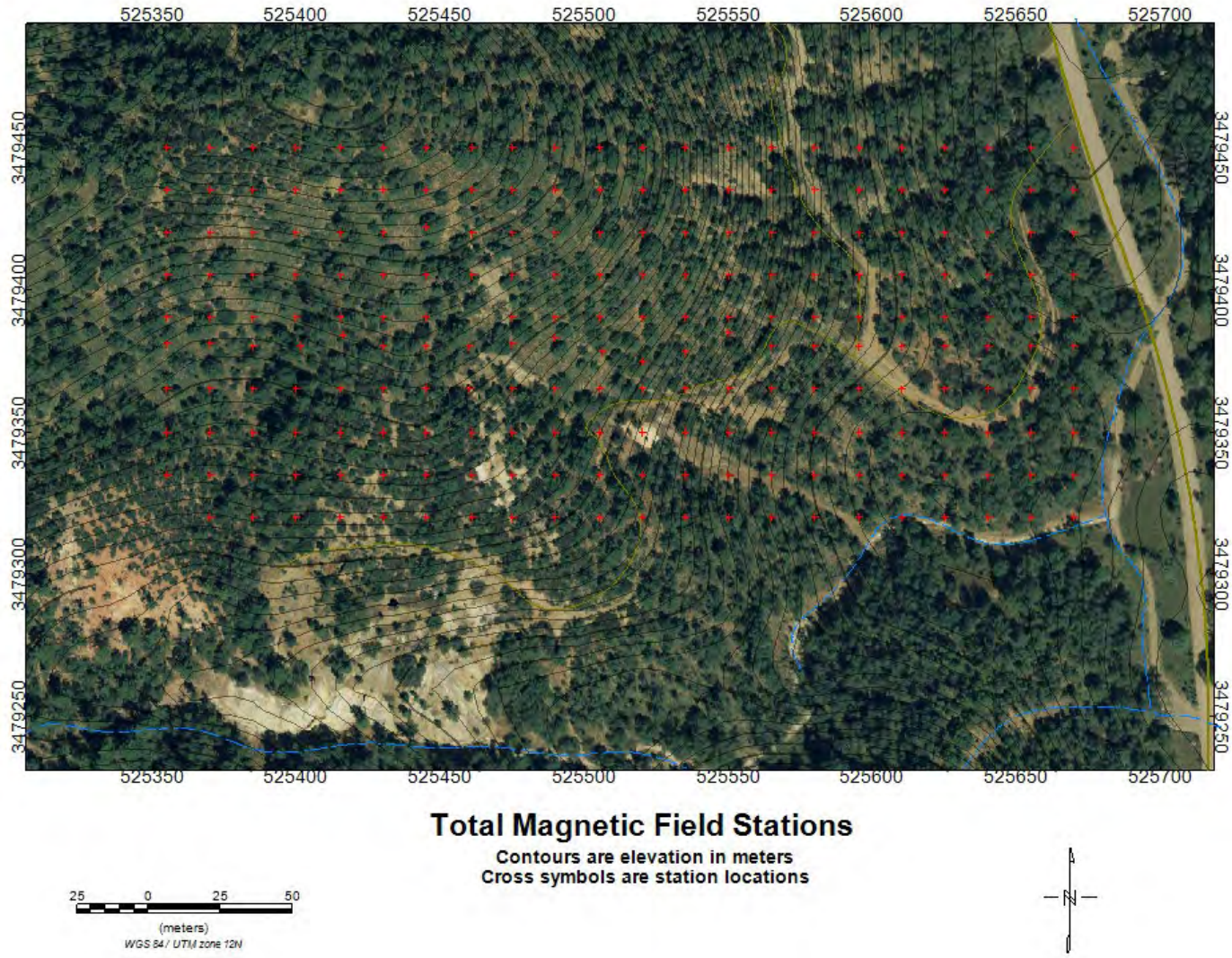

Figure 2.8. Location map with all magnetic field stations represented as red dots.

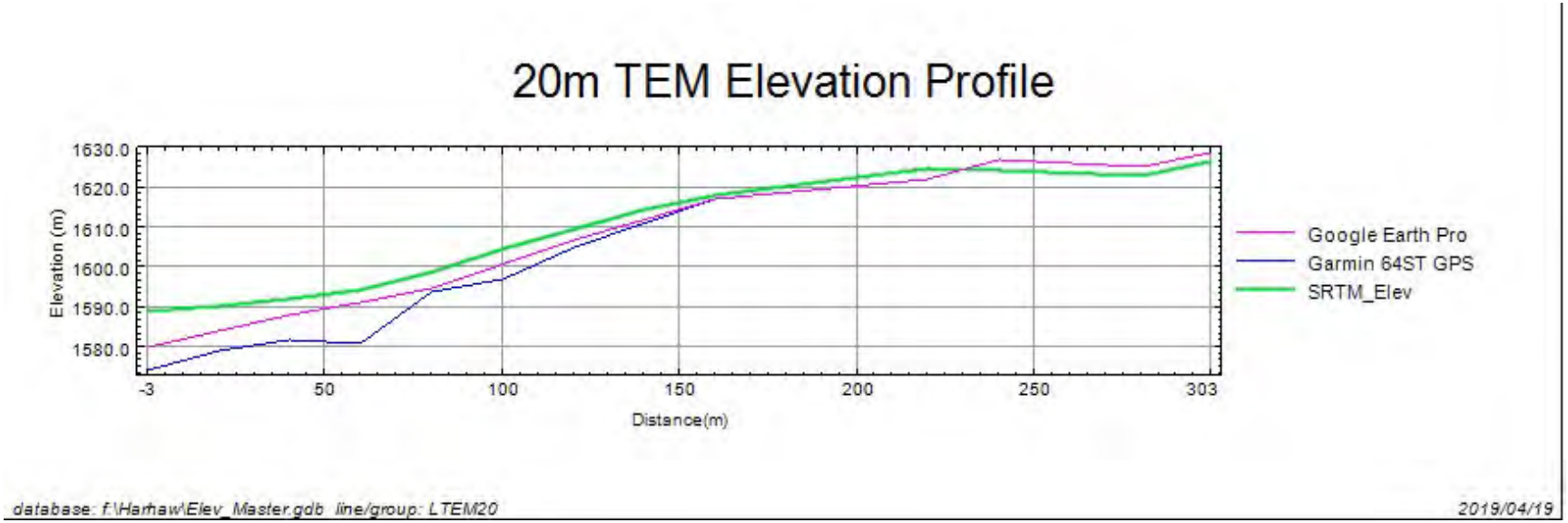

Figure 2.9. Elevation profiles of DC Resistivity Line 1 from East (left) to West (right).

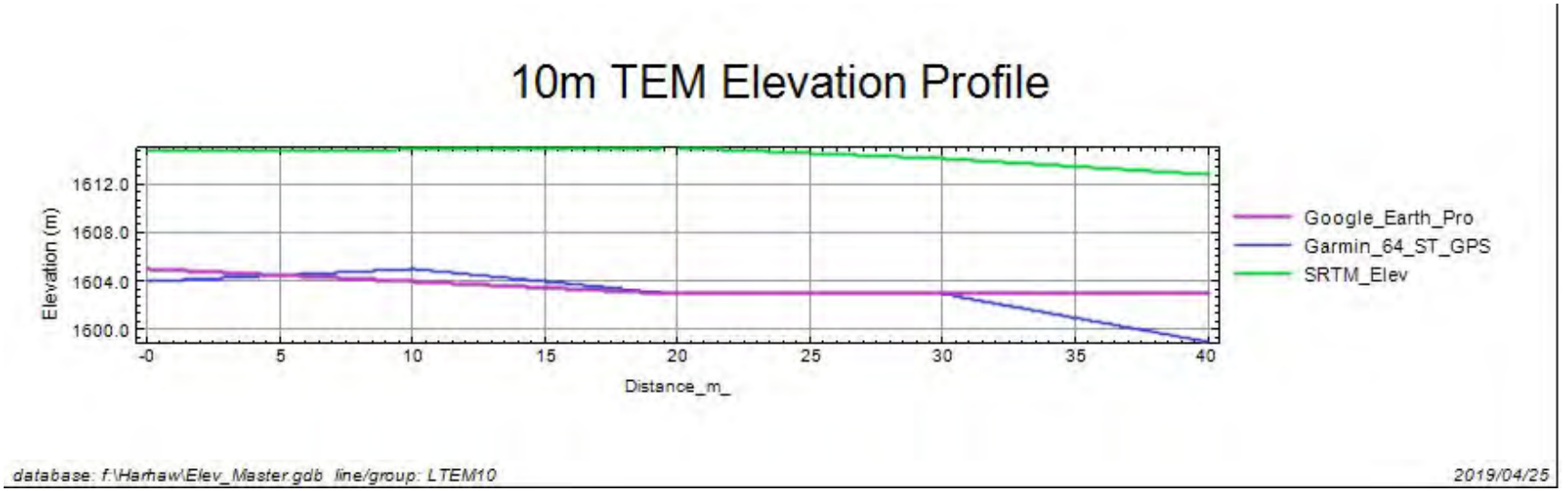

Figure 2.10. Elevation profiles of DC Resistivity Line 2 from East (left) to West (right).

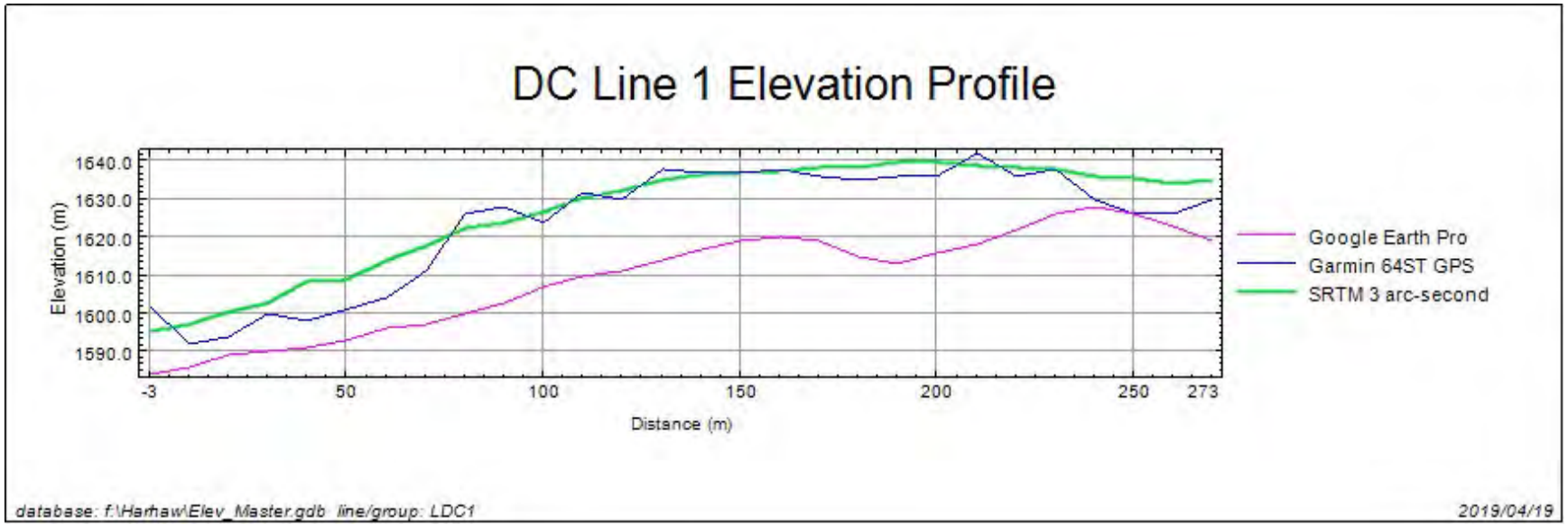

Figure 2.11. Elevation profiles of 20m TEM loops from East (left) to West (right).

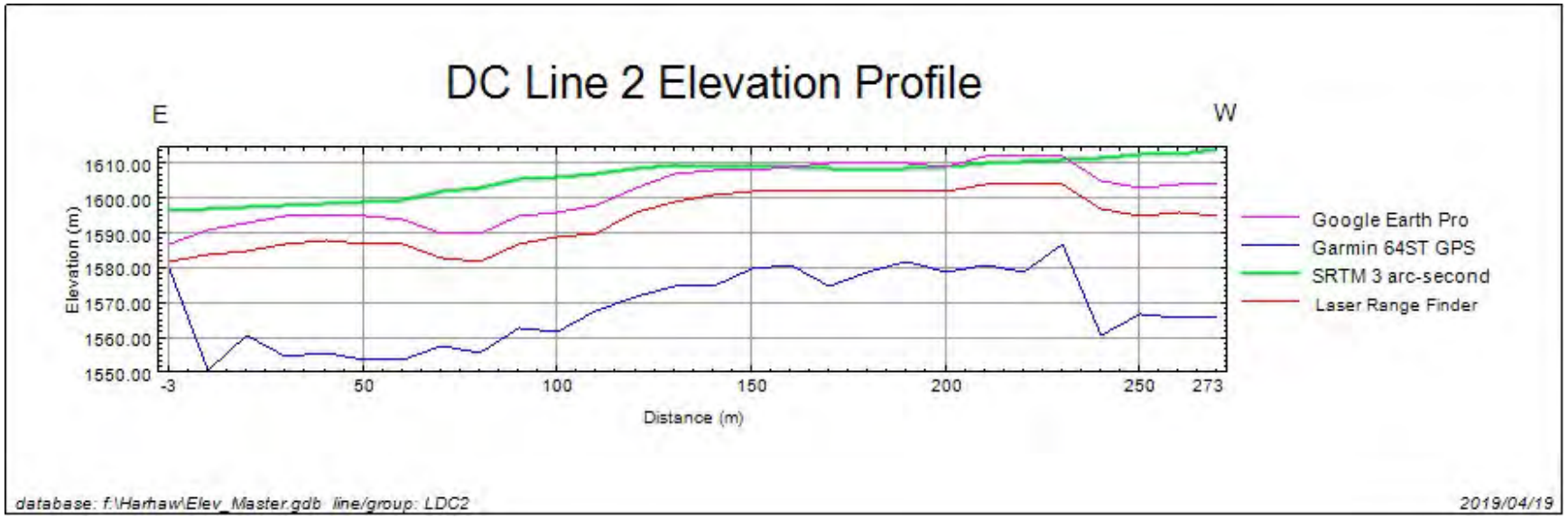

Figure 2.12. Elevation profiles of 10m TEM loops from East (left) to West (right).

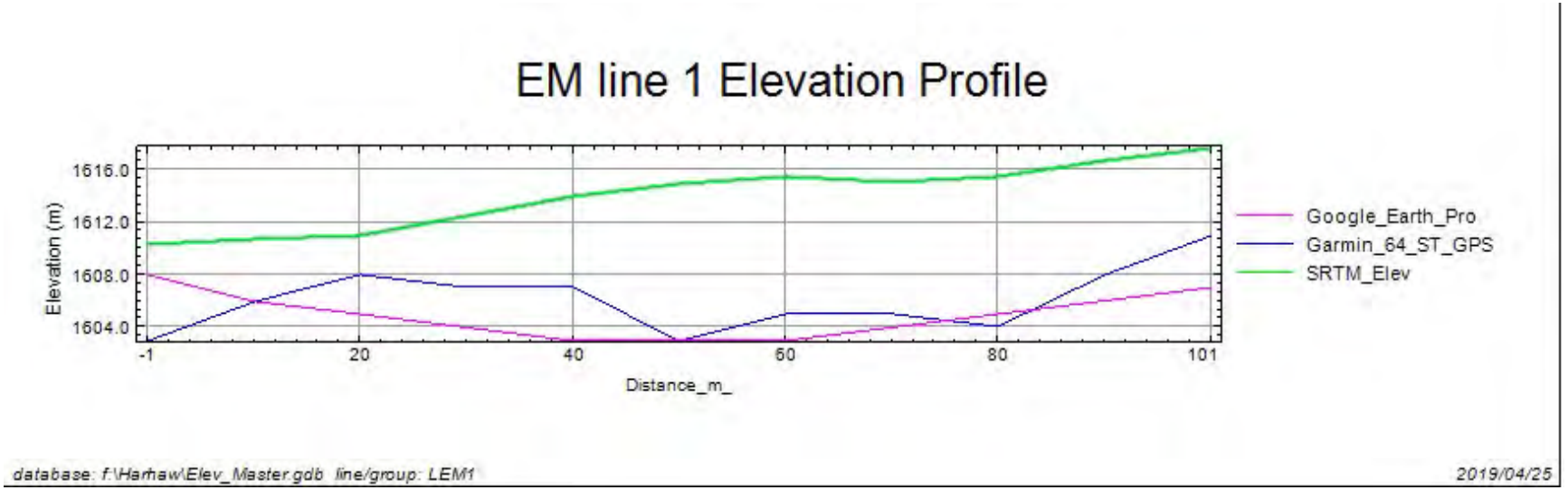

Figure 2.13. Elevation profiles of EM-31/38 Line 1 on tailings from East (left) to West (right).

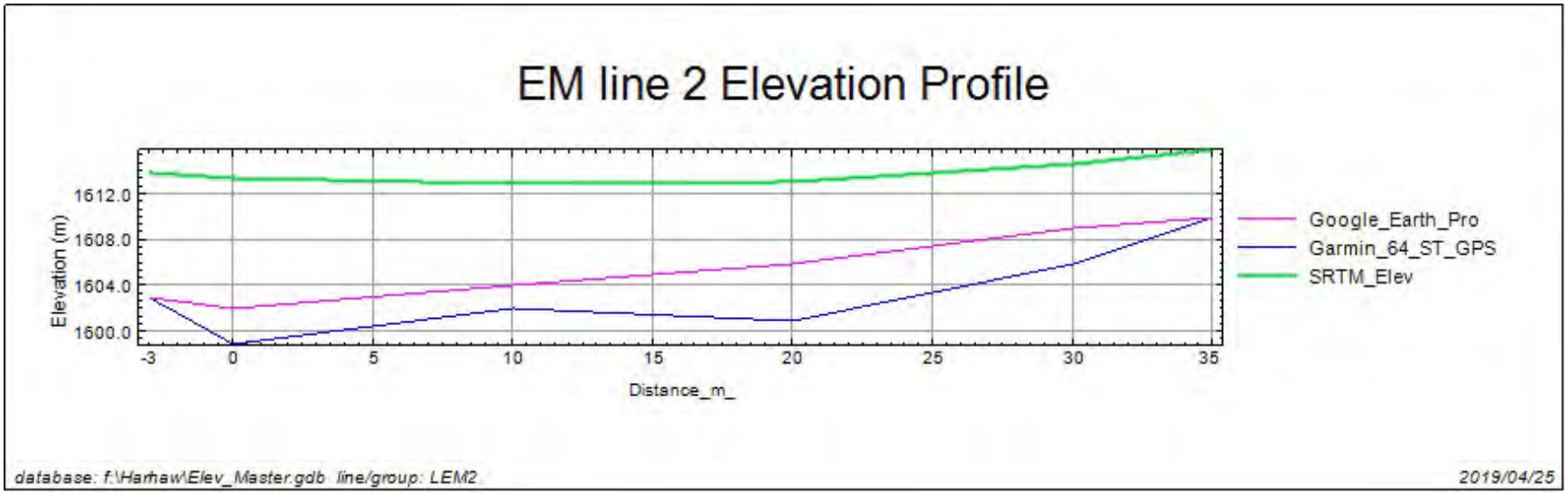

Figure 2.14. Elevation profiles of EM-31/38 Line 2 on tailings from South (left) to North (right).

2.6 References

Patagonia Alliance, 2016, Southern Arizona's Mountain Empire: Sanctuary for Rare and Unusual Species, http://www.patagoniaalliance.org/southern-arizonas-mountain-empire-sanctuary-rare-unusual-species/, accessed April 15, 2019.

US Forest Service, 2017, Tested Accuracies, https://www.fs.fed.us/database/gps/mtdcrept/accuracy/documents/accuracy.pdf, accessed April 15, 2019.

3. Transient Electromagnetic (TEM) Survey

3.1 Introduction and Methods

The Transient Electromagnetic (TEM) method is a geophysical technique used to image subsurface resistivity or conductivity. It can be used for subsurface geophysical investigations on scales of meters to kilometers in depth. The goals of the survey used for this location are to identify zones of high and low resistivity and to provide information on the depth of the tailings piles.

Two ungrounded loops are positioned on the ground, and a time-varying current flowing through the outer (transmitter) loop generates an electromagnetic wave that diffuses through the subsurface (Figure 3.1). Induced eddy currents from subsurface conductive layers produce secondary EM fields, which are picked up by the inner (receiver) loop. These eddy currents decay rapidly after the current is shut off. Depending on the conductivity of the material, the decay can be fast or slow, where conductive materials have slower decay times. When the current is turned off, the instrument records the resulting decay curves using the receiver loop in 31 windows from approximately 1.5 µs to 3 ms after the current is turned off. The instrument begins recording 1.5 µs after the current is turned off, because there is still a small amount of current flowing in the transmitter loop (Zonge International, 2019).

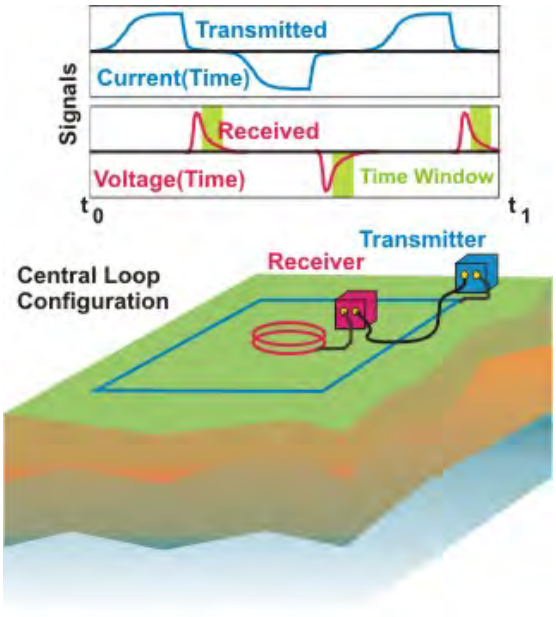

Figure 3.1. Representation of TEM arrangement and the signal response in time domain (BGR, 2019).

3.2 Instrumentation and Field Procedures

The data were collected on two consecutive weekends, February 9-10 and February 16-17 of 2019. The instrumentation included the Zonge International GDP-32 II, a multi-function receiver, along with the Zonge International NT-20 transmitter, referred to as a Zonge NanoTEM system. The receiver records multiple transient surroundings per loop, and computer modeling translates the time to depth. The square wave repletion frequency used in this case was 32 Hz. Other parameters set on the transmitter were SEM (Standard Error of the Mean) 1-3, and 512 cycles at 3 A.

The TEM data were taken on two different lines. Line 1 (Figure 3.2) consisted of 20 m by 20 m square transmitter loops with a 5 m by 5 m square receiver loop in the center of each transmitter loop. The arrays for Line 2 (Figure 3.3) consisted of 10 m by 10 m square transmitter loops, each with a 2.5 m by 2.5 m square receiver loop. A guideline to determine the maximum depth of investigation is multiplying the loop size by a factor of three to five, depending on the lithologic properties such as fluid content and conductivity (Zonge International, 2019). Based on this approximation, a rough maximum depth of investigation for Line 1 is 60-100 m, and the maximum depth of investigation for Line 2 is 30-50 m. Center point locations were recorded using Garmin GPSMAP 64ST handheld GPS units, which may deviate from the actual center point locations by a few meters due to GPS error (Garmin, 2019).

Line 1 (Figure 3.2) consisted of thirteen loops with center points trending on an azimuth of 235°/55°. Loops 0 through 8 were placed along the azimuth covering a distance of 0 to 160 m along the line. Due to terrain conditions and time constraints, 40 m was skipped, and Loop 11 was placed covering a distance of 220 to 240 m along the survey line. Another 20 m was skipped, and Loop 14 was placed at 280 m. Loop 15 was placed parallel to and north of the line, but the data from this loop was not included in the inversion model (Figure 3.4) because of its poor quality (Figure 3.6l).

Line 2 (Figure 3.3), consisted of five loops trending west to east, along the surface of the tailings piles. The line went from the starting point of 0 m, labeled Loop 1, to 25 m eastwards ending with Loop 5. The data from Loop 5 was not included in the inversion model (Figure 3.5) due to high noise.

3.3 Data Processing

The nanoTEM data collected in the field were downloaded from the GDP-32 II receiver and processed using the Zonge International's DATPRO suite of geophysical software, consisting of two main programs: TEMAVG and STEMINV. Field measurements at each loop consist of three repeated measurements, referred to as 'blocks.' TEMAVG combines these three measurements and computes the average value from them, which is then processed and inverted by the STEMINV program. The inversion data were then compared with the measured data to determine whether or not the modeled results were accurate. The data were plotted using the 1D smooth-model tool in STEMINV and can be seen in Figures 3.4 and 3.5.

3.4 Interpretation and Conclusions

The inversion model of the 20 m nanoTEM survey shows a large conductor between 160 and 220 m along transect, starting approximately 45 m below the surface and extending down below the section (Figure 3.4). Additionally, two prominent resistive features that extend beyond our depth of investigation were detected on the east and west flanks of this conductive body. There is another conductive area around 35 m below the surface that extends to the bottom of the section at the beginning of the survey, below Loop 0. It is possible that this low resistivity region could be related to a fault, particularly in the area of the Harshaw creek fault (Figure 1.2). Based on Archie's Law, the faulting could have created an area of high porosity and water saturation, making the area more electrically conductive.

The inversion model of the 10 m nanoTEM survey indicates a relatively conductive region extending to about 8 m below the surface. This may not indicate the depth of the tailings material, however, as field observations of the area note that the height of the tailings compared to the bottom of the drainage was no more than 5 m. The greater depth of the TEM conductive region may be due to conductive fluids moving through the bedrock fractures below the tailings.

Potentially, there are a few factors that could have influenced the nanoTEM recordings. The first is that the survey was carried out over an abandoned mine location, and as such had a high probability of detecting buried and surface pieces of metal. Also, some sections of the 20 m loop wires in areas of high relief were often suspended off the ground by up to a meter, which may have skewed the instrument readings.

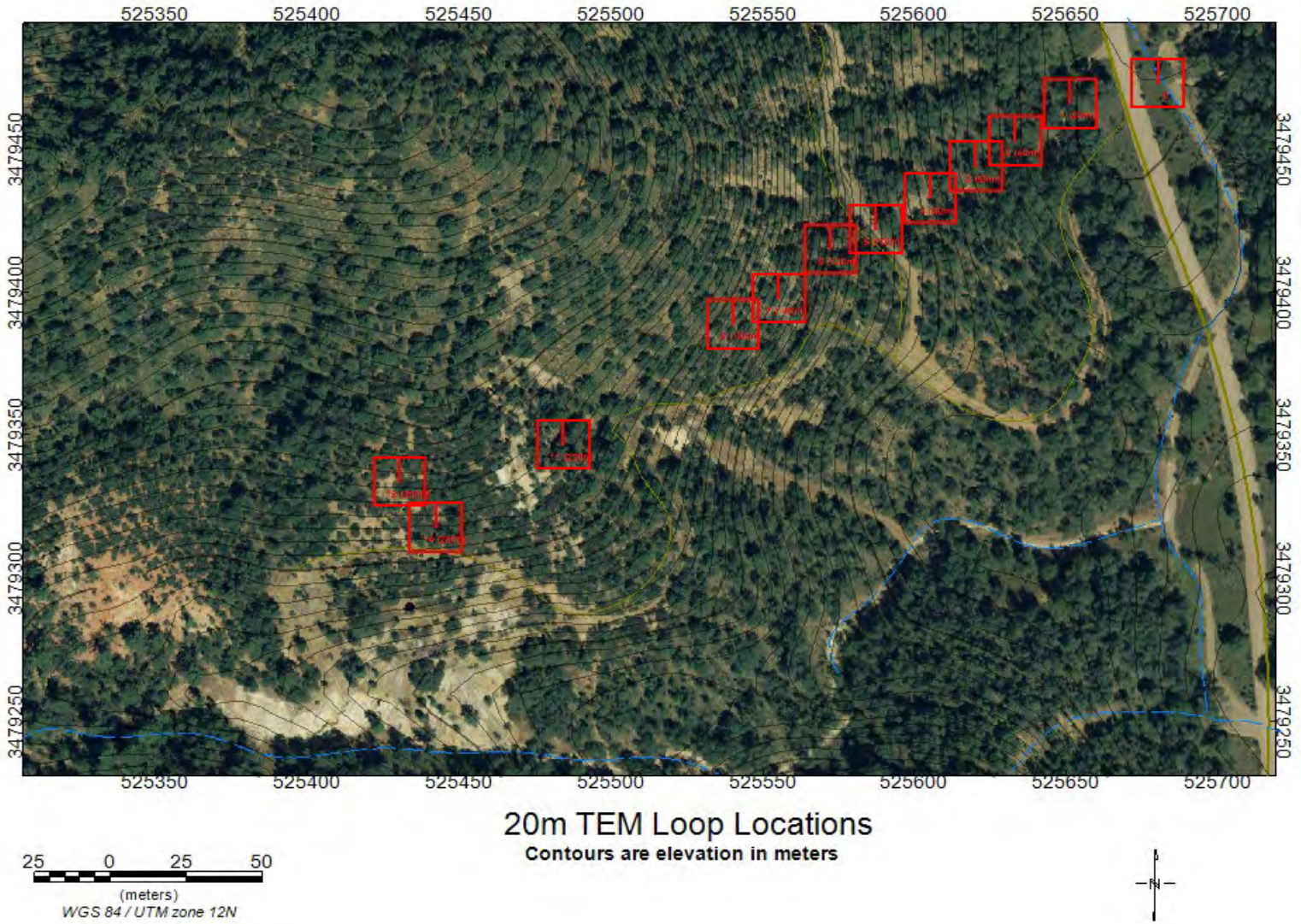

Figure 3.2. Location map for the 20 m TEM loops along Line 1. Note that Loop 15 was not used in the inversion modeling.

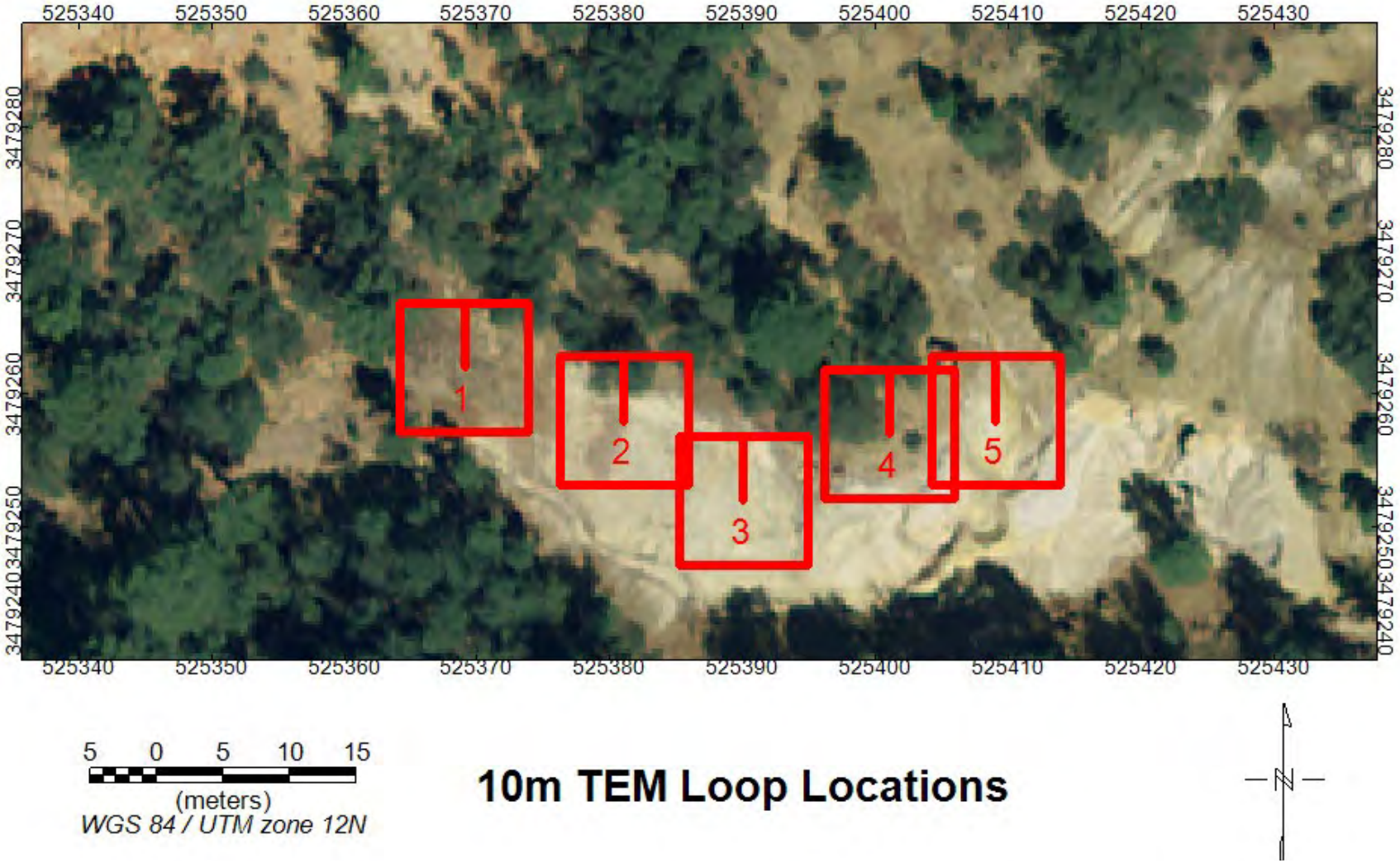

Figure 3.3. Location map for the 10 m TEM loops along Line 2 on the surface of the tailings piles. Note that Loop 5 was not used in the inversion modeling.

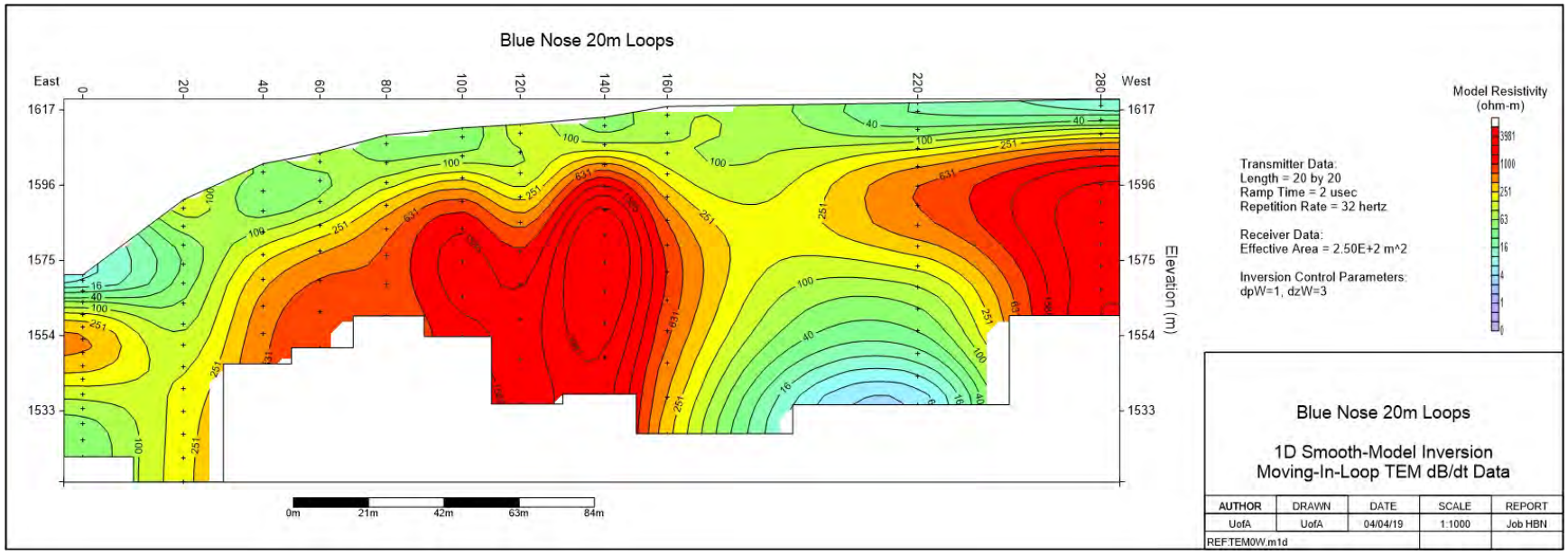

Figure 3.4. Modeled inversion of the 20 m loop (Line 1) data. Note that warm colors indicate high resistivity and cool colors indicate low resistivity. Image provided by Jamie Macy (USGS).

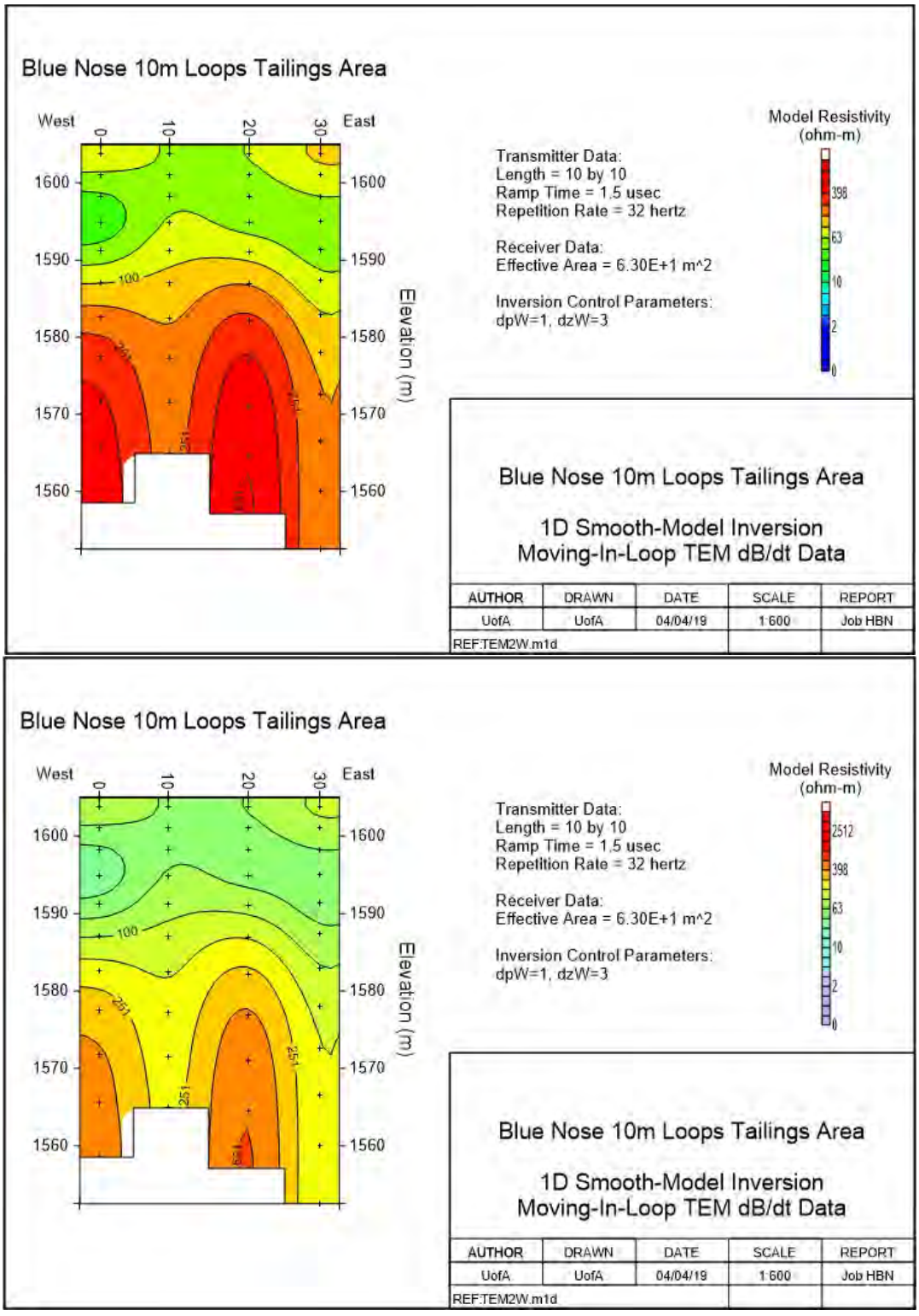

Figure 3.5. Modeled inversion of the 10 m loop (Line 2) data. The top image has a color scale that makes the resistive body stand out better, while the bottom image has the same color scale as the modeled data in Figure 3.4. Images provided by Jamie Macy (USGS).

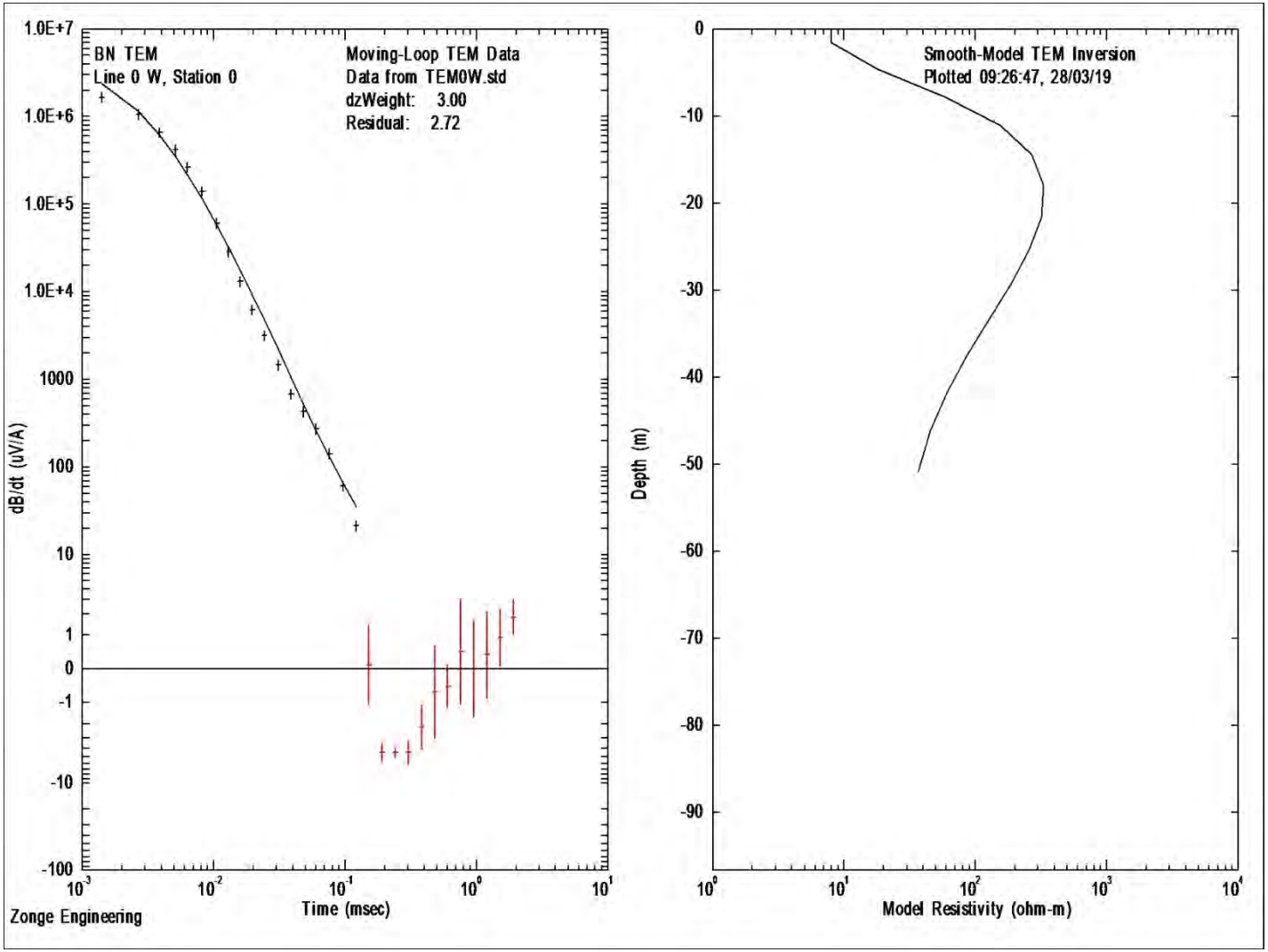

Figure 3.6a. Modeled and transient curve for Line 1, Loop 0.

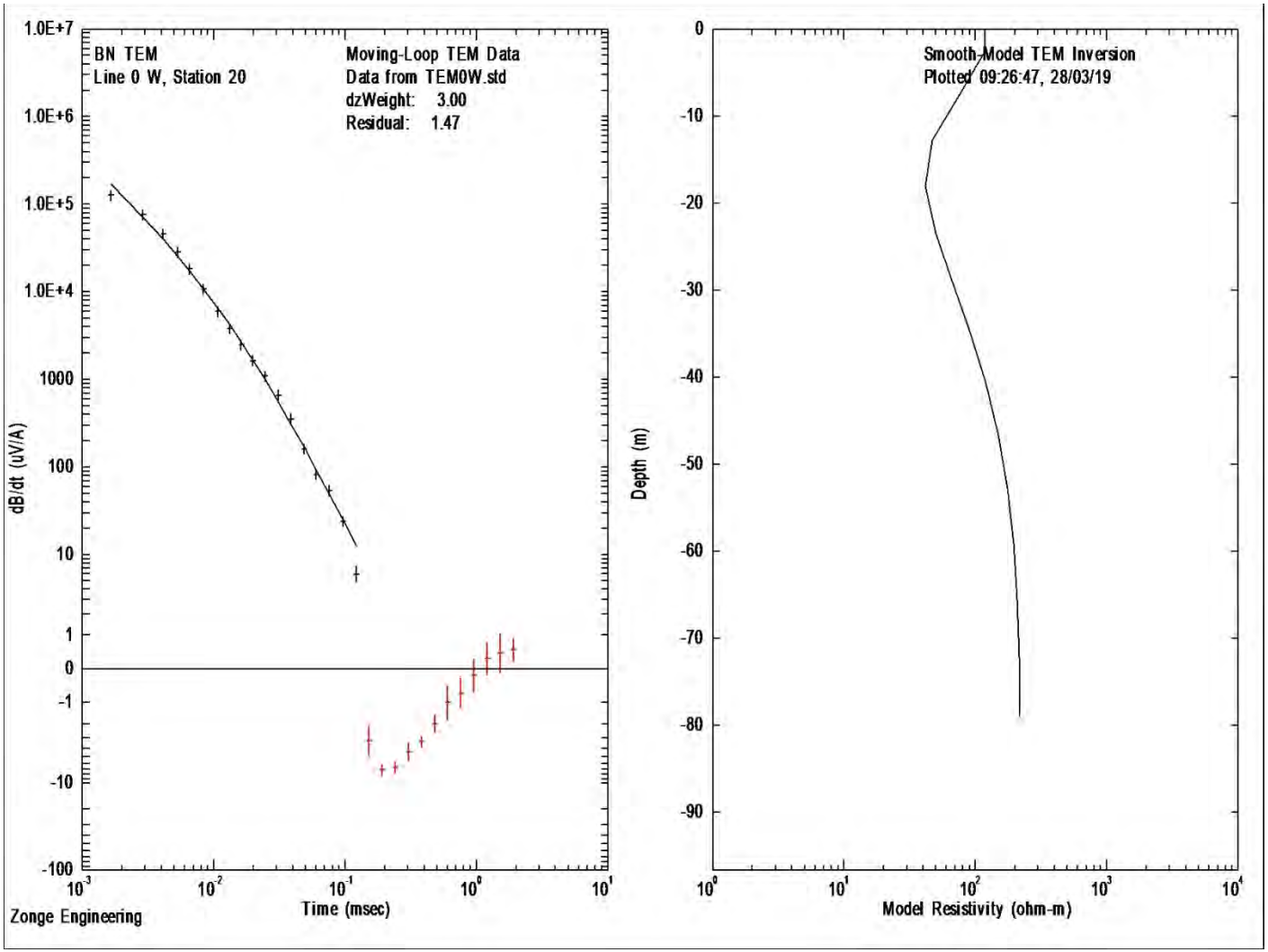

Figure 3.6b. Modeled and transient curve for Line 1, Loop 1.

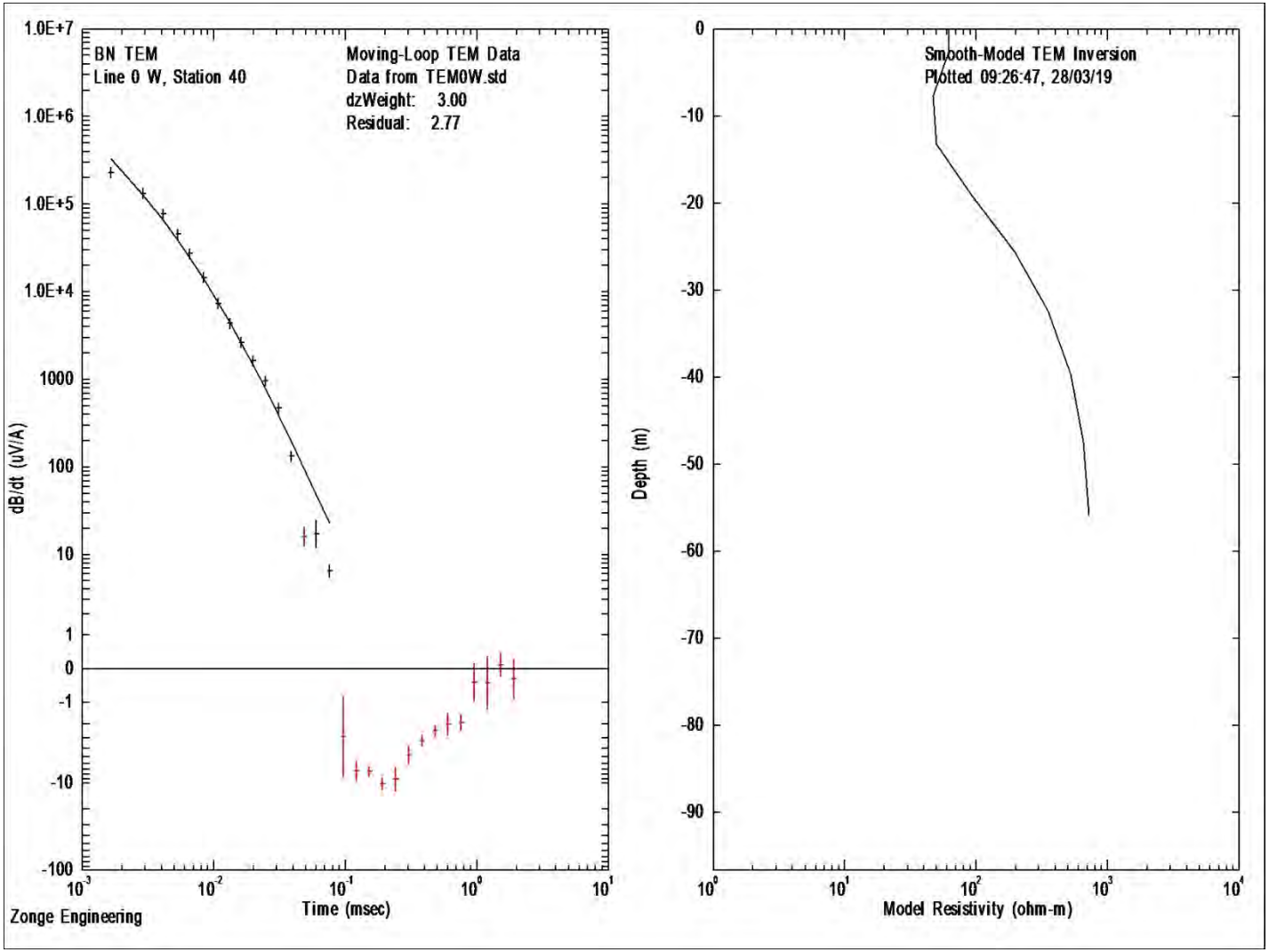

Figure 3.6c. Modeled and transient curve for Line 1, Loop 2.

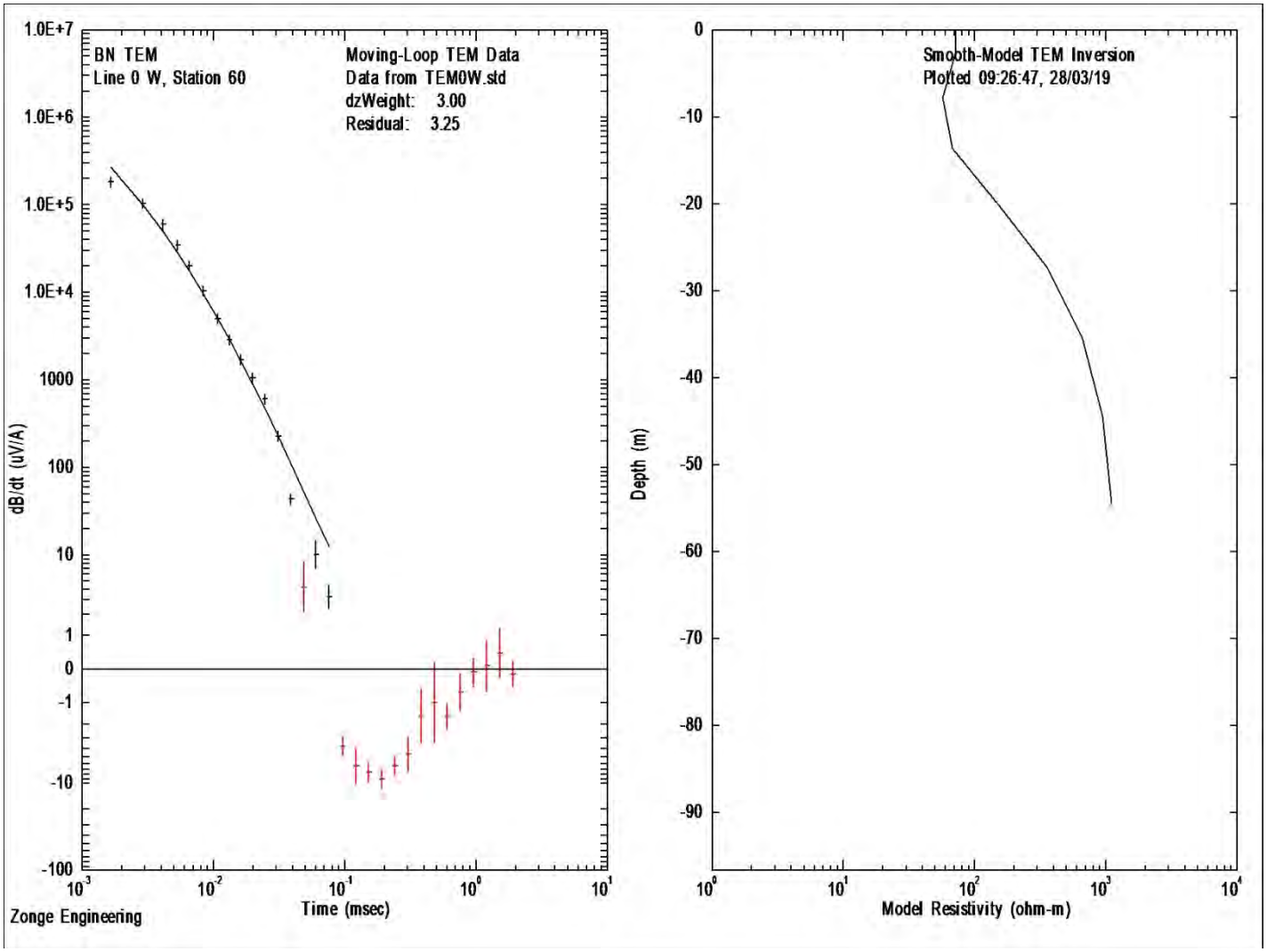

Figure 3.6d. Modeled and transient curve for Line 1, Loop 3.

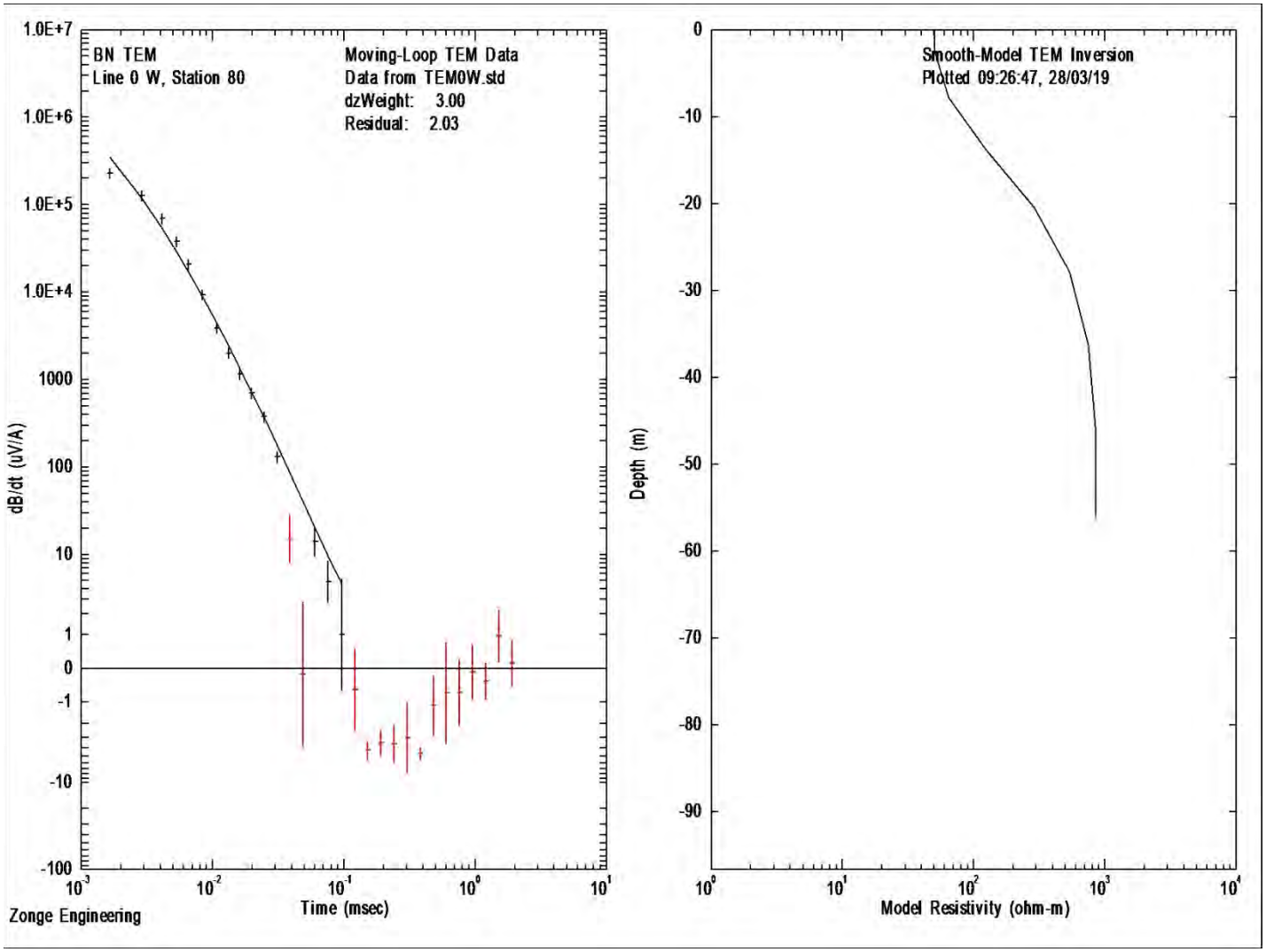

Figure 3.6e. Modeled and transient curve for Line 1, Loop 4.

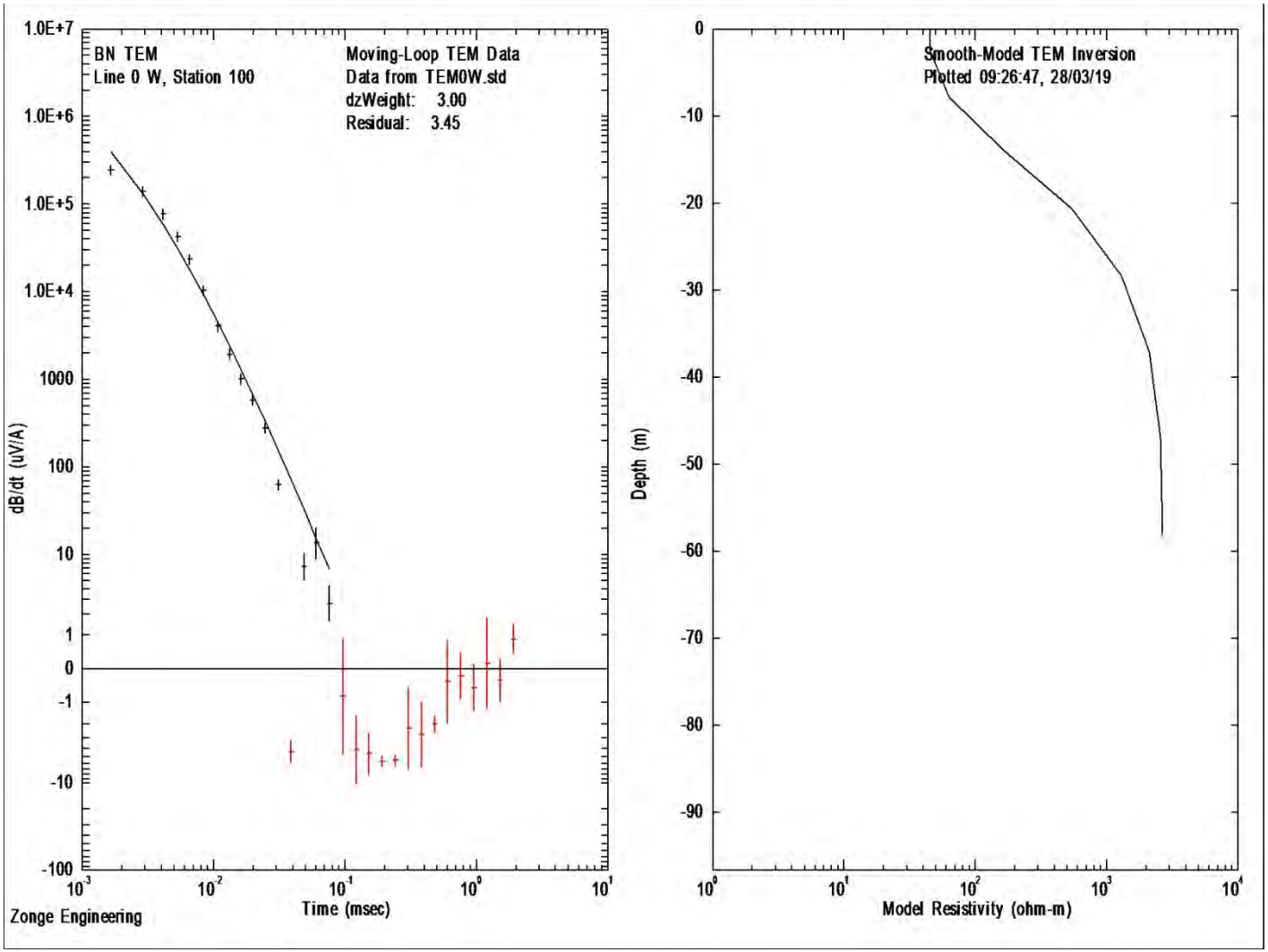

Figure 3.6f. Modeled and transient curve for Line 1, Loop 5.

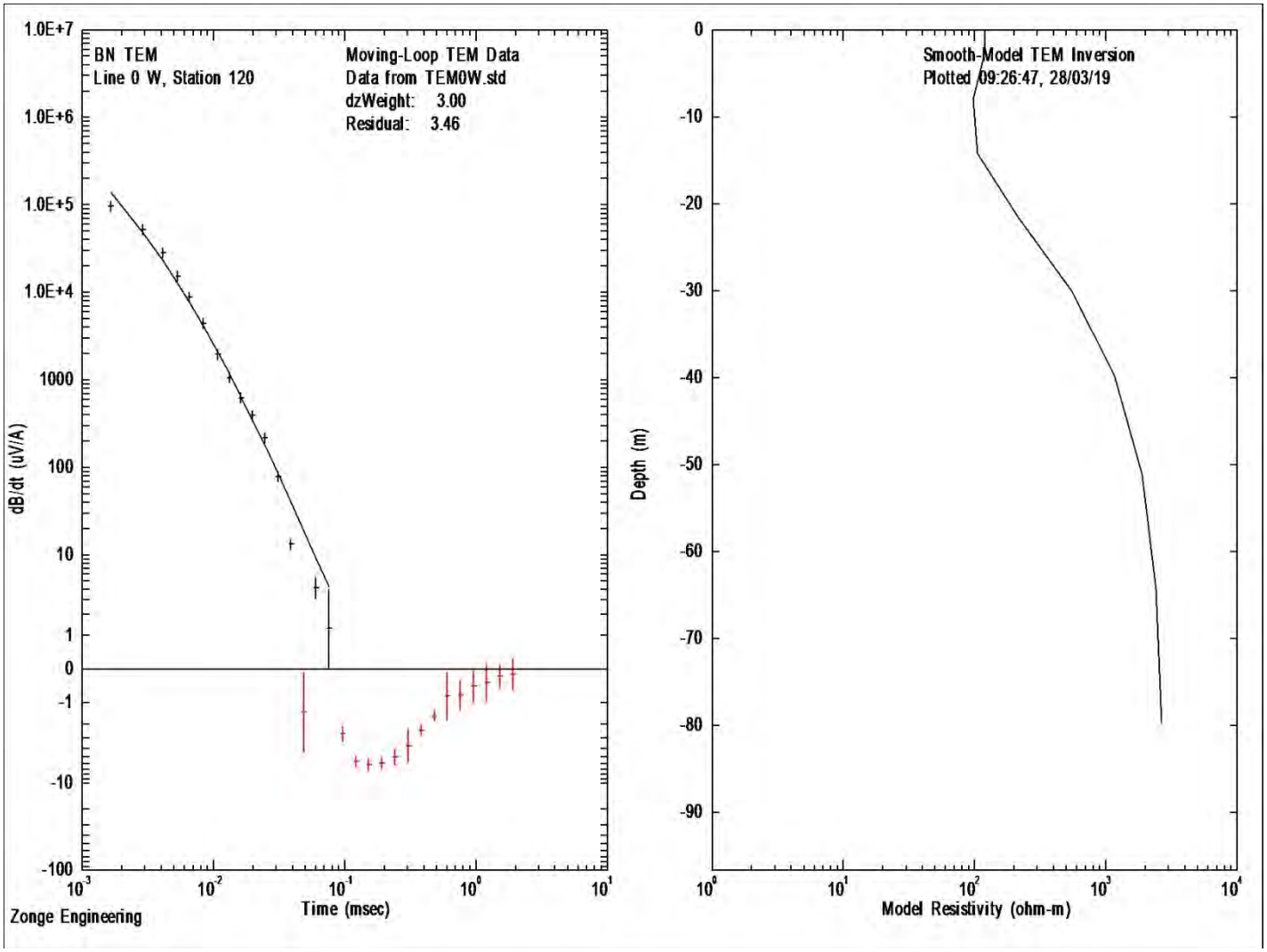

Figure 3.6g. Modeled and transient curve for Line 1, Loop 6.

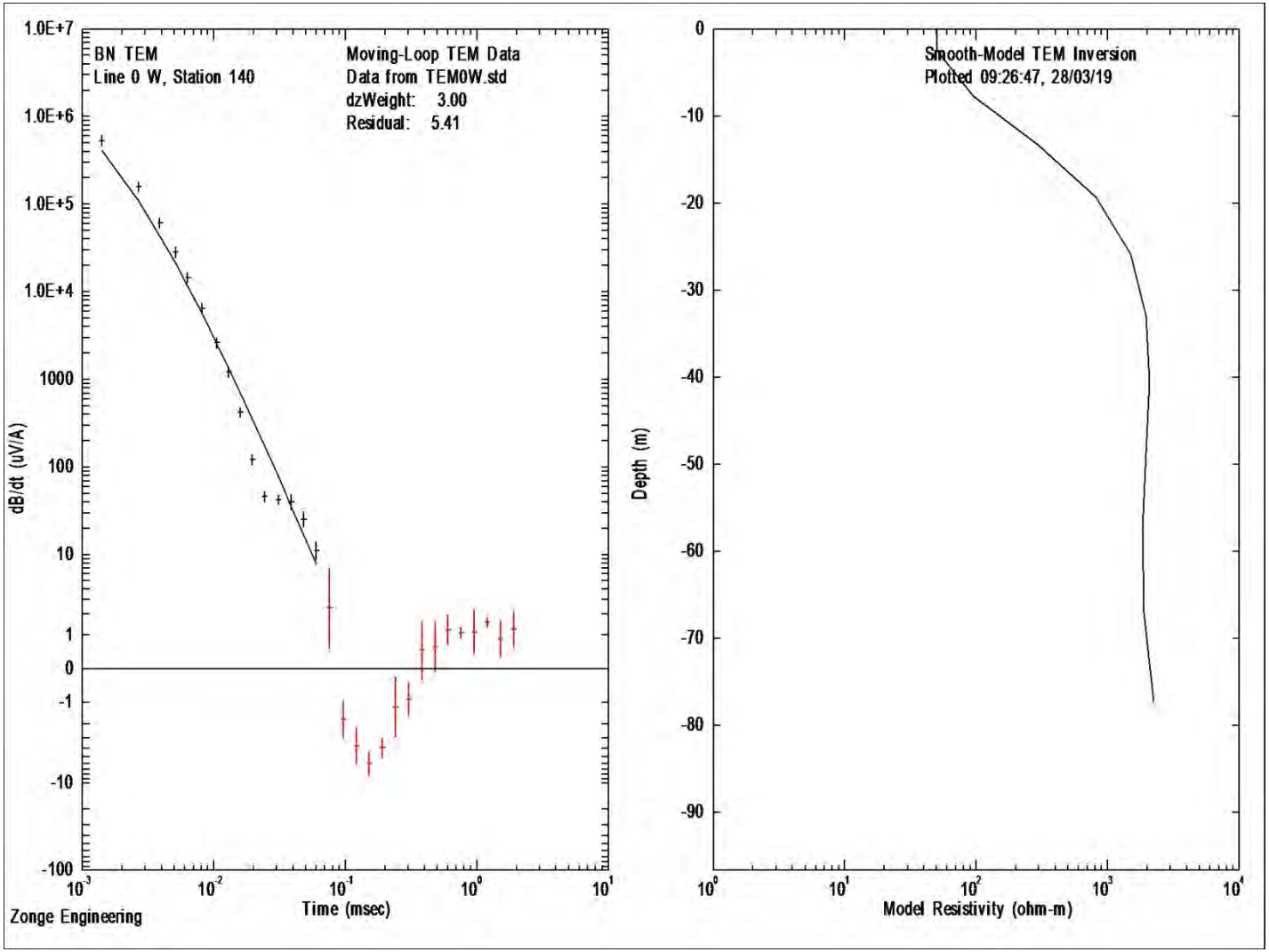

Figure 3.6h. Modeled and transient curve for Line 1, Loop 7.

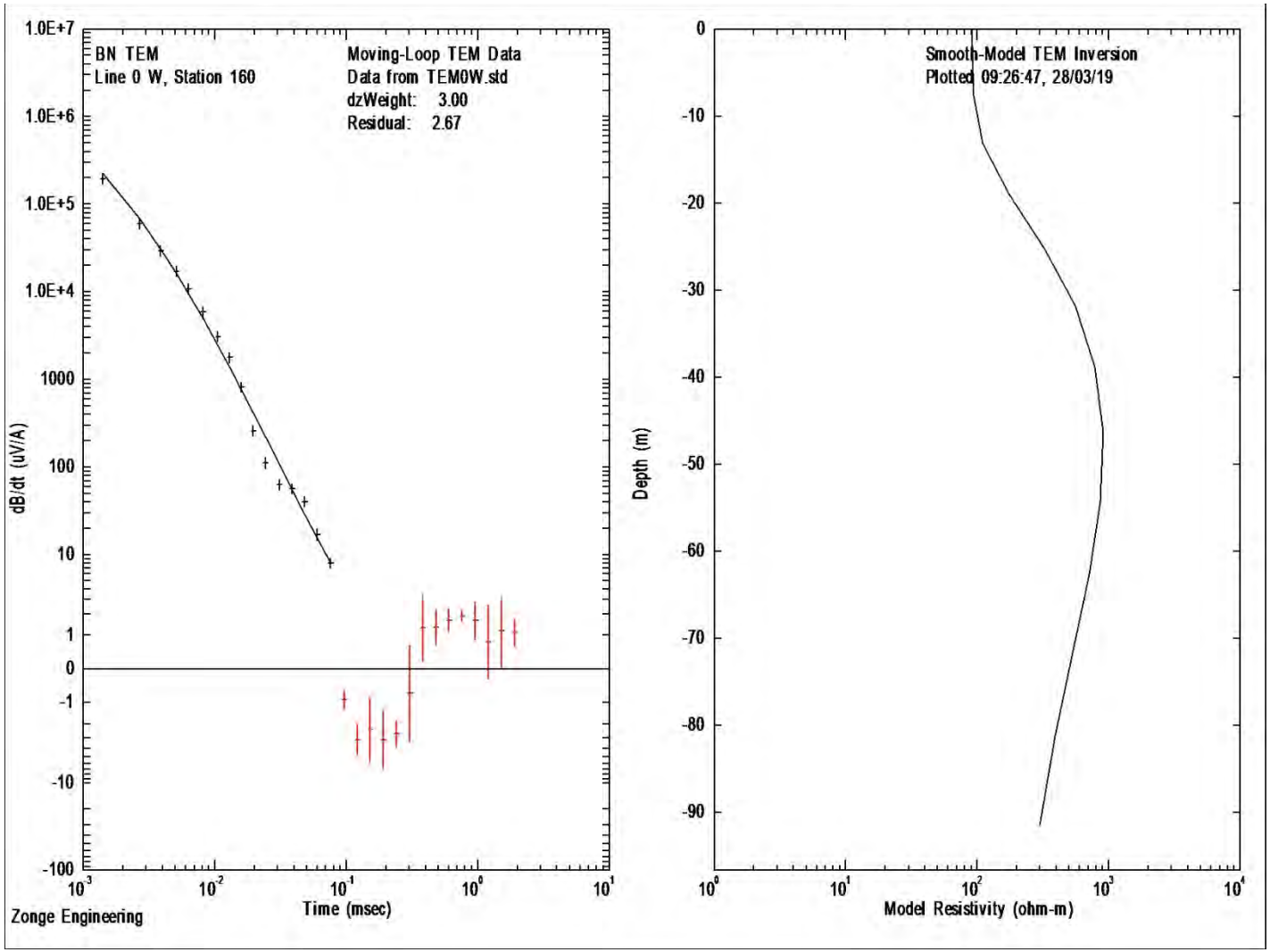

Figure 3.6i. Modeled and transient curve for Line 1, Loop 8.

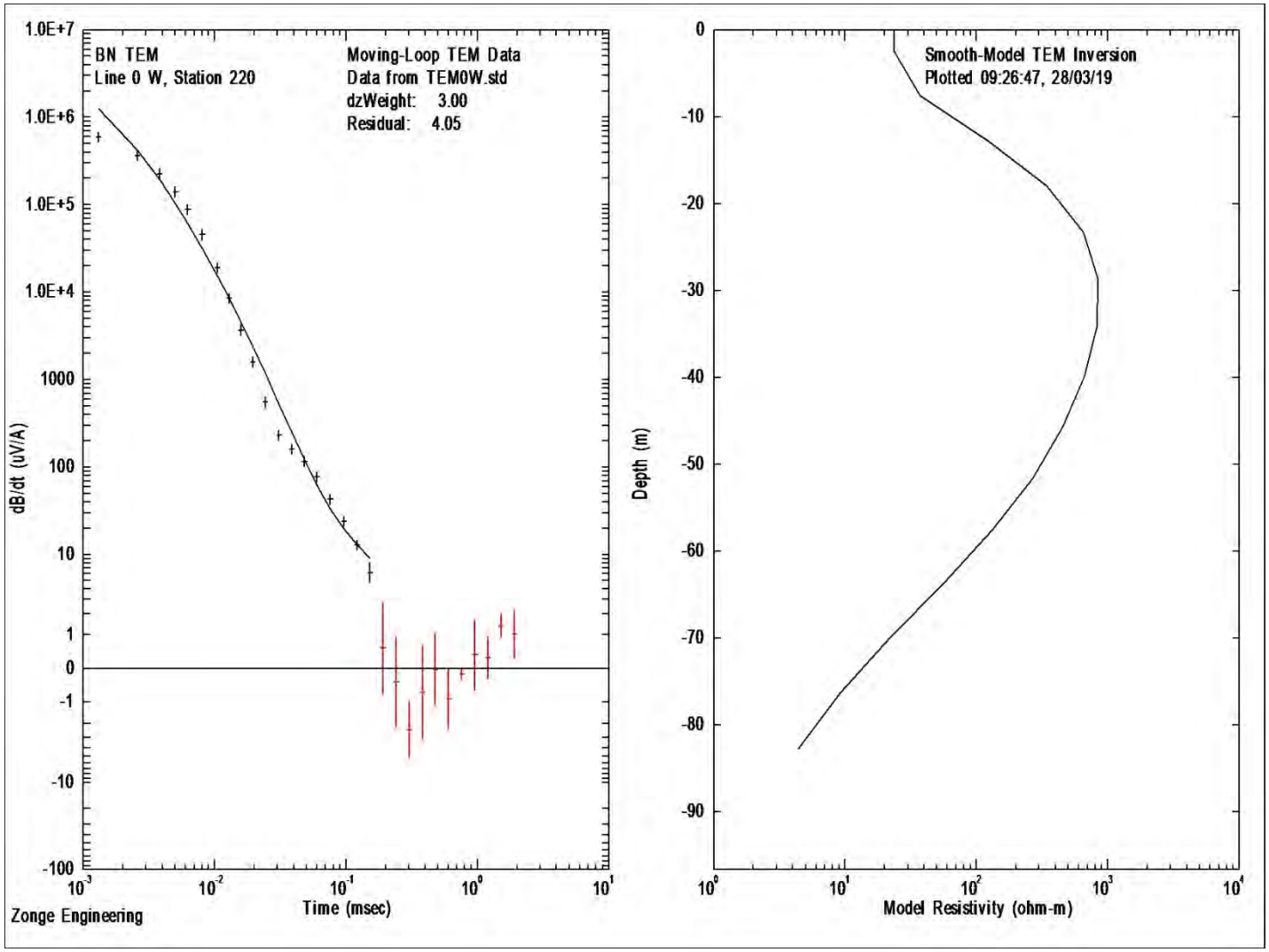

Figure 3.6j. Modeled and transient curve for Line 1, Loop 11.

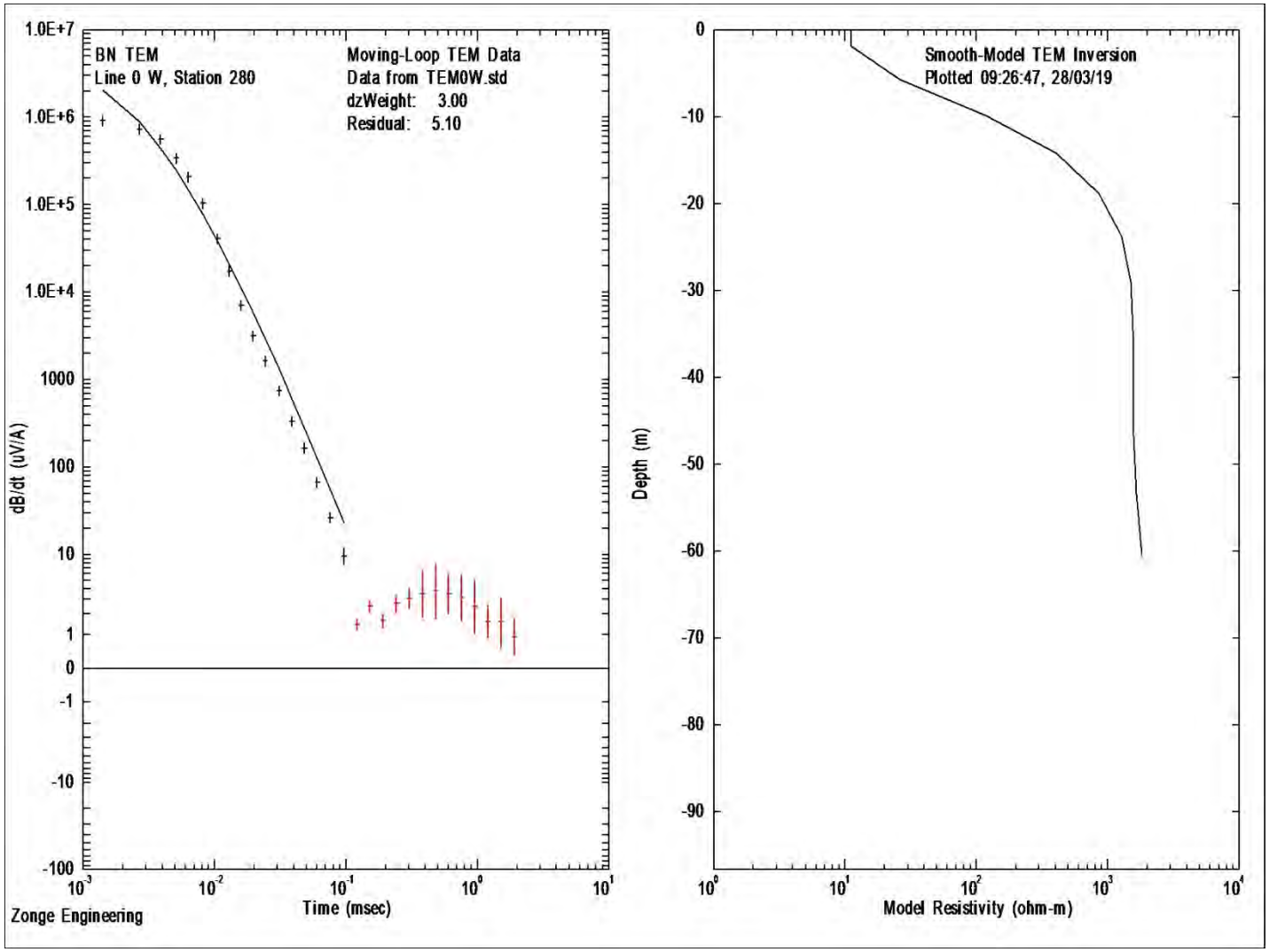

Figure 3.6k. Modeled and transient curve for Line 1, Loop 14.

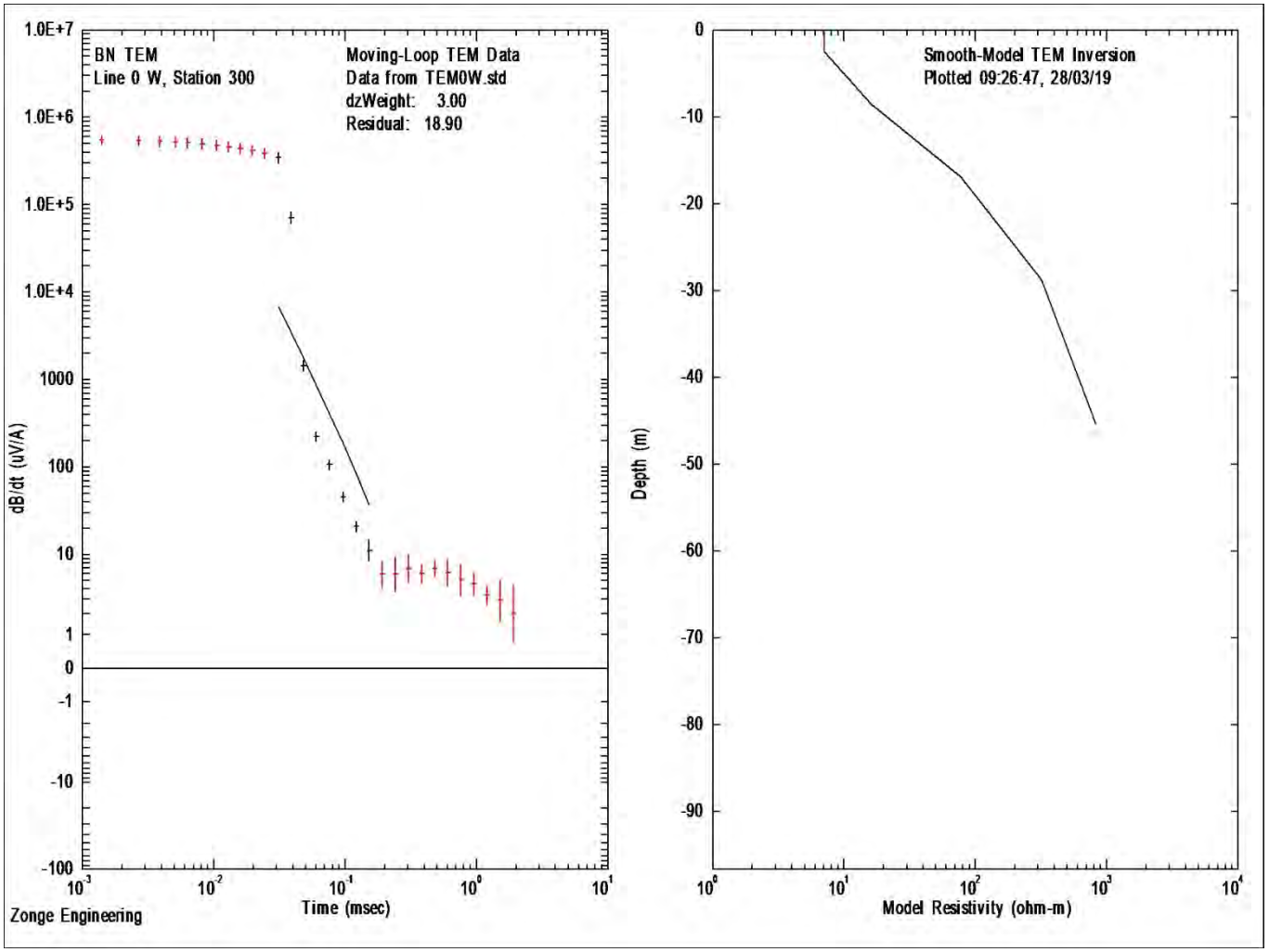

Figure 3.6l. Modeled and transient curve for Line 1, Loop 15. Not included in inversion (Figure 3.4) because of abnormal decay curve.

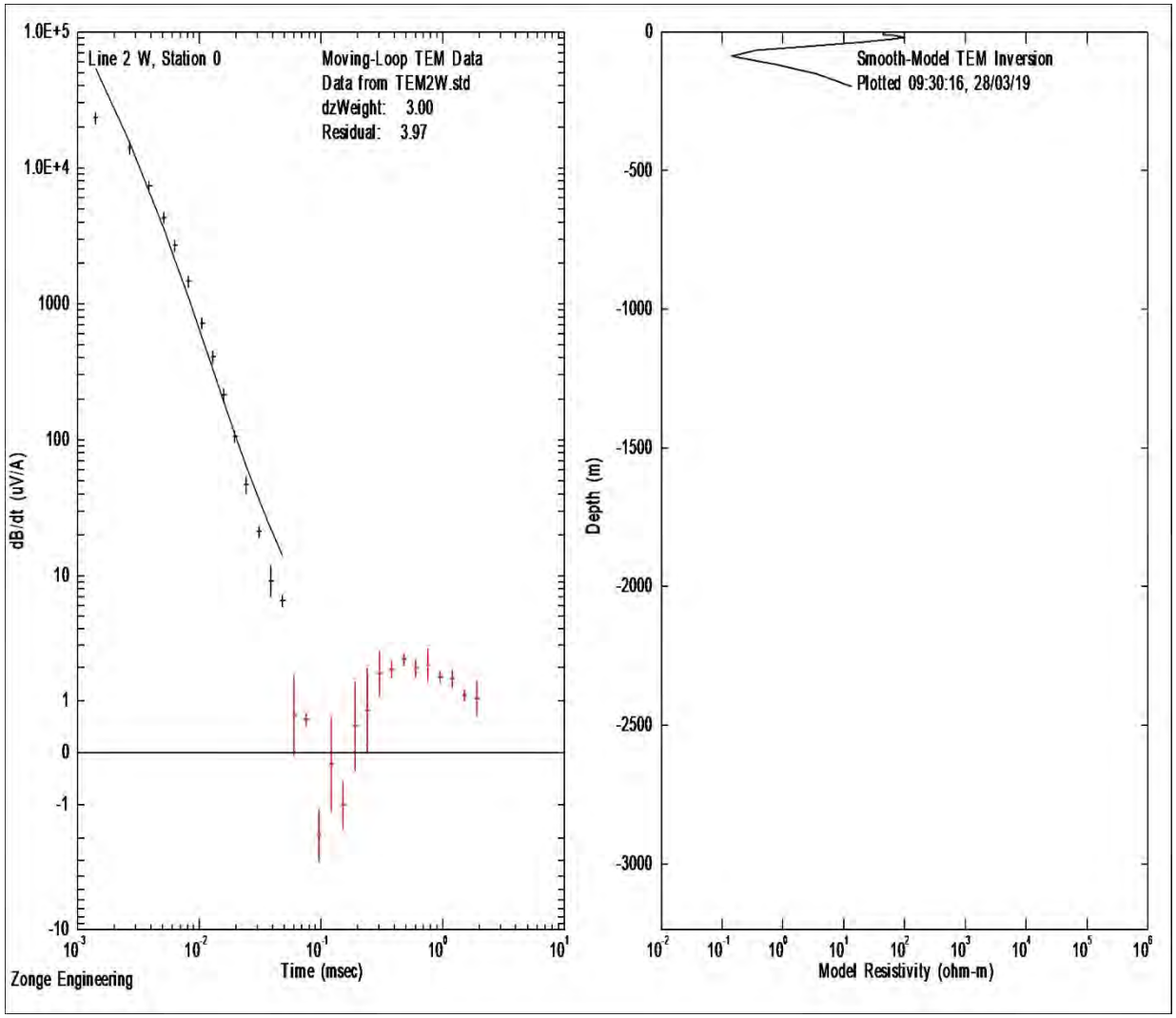

Figure 3.7a. Modeled and transient curve for Line 2, Loop 1.

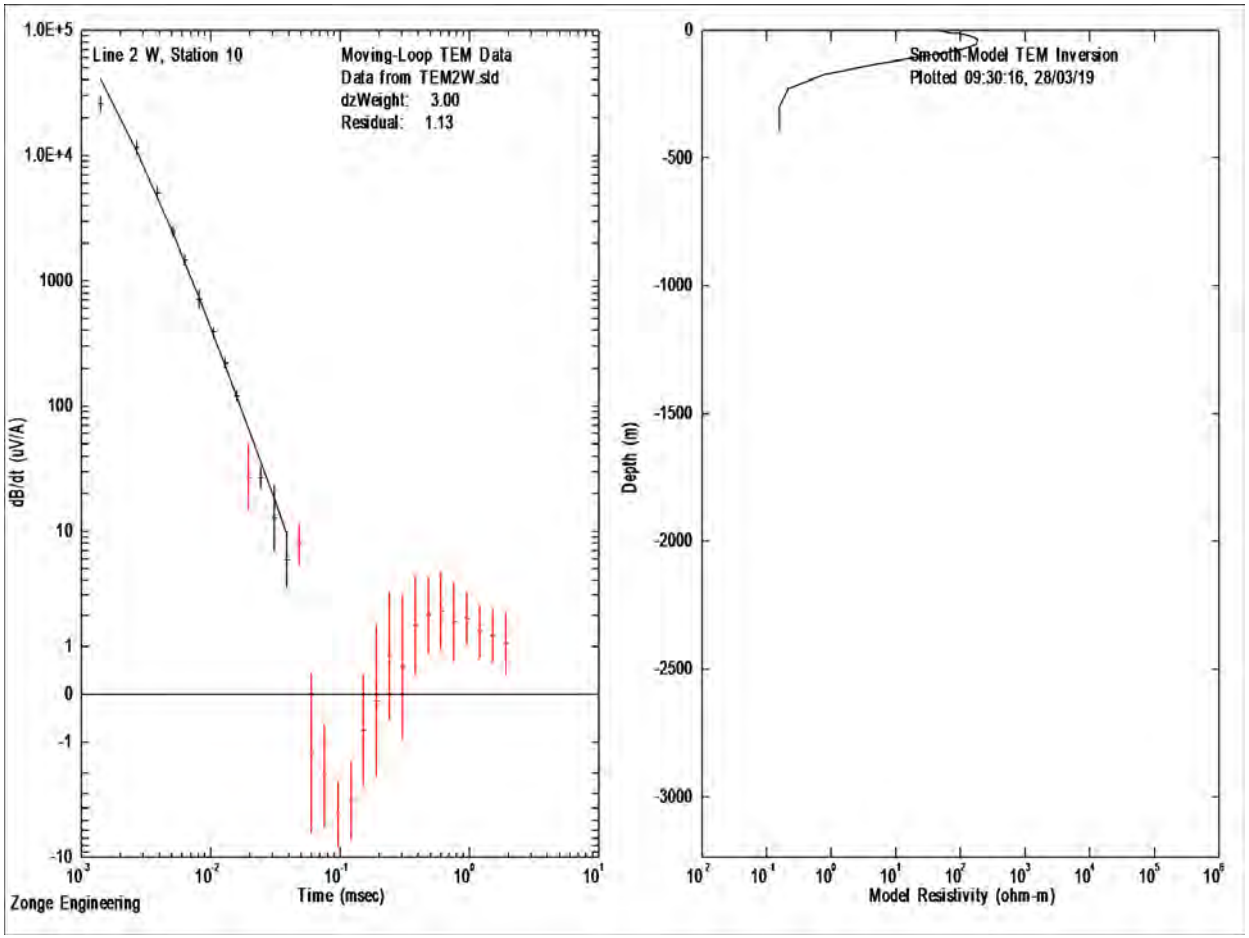

Figure 3.7b. Modeled and transient curve Line 2, Loop 2.

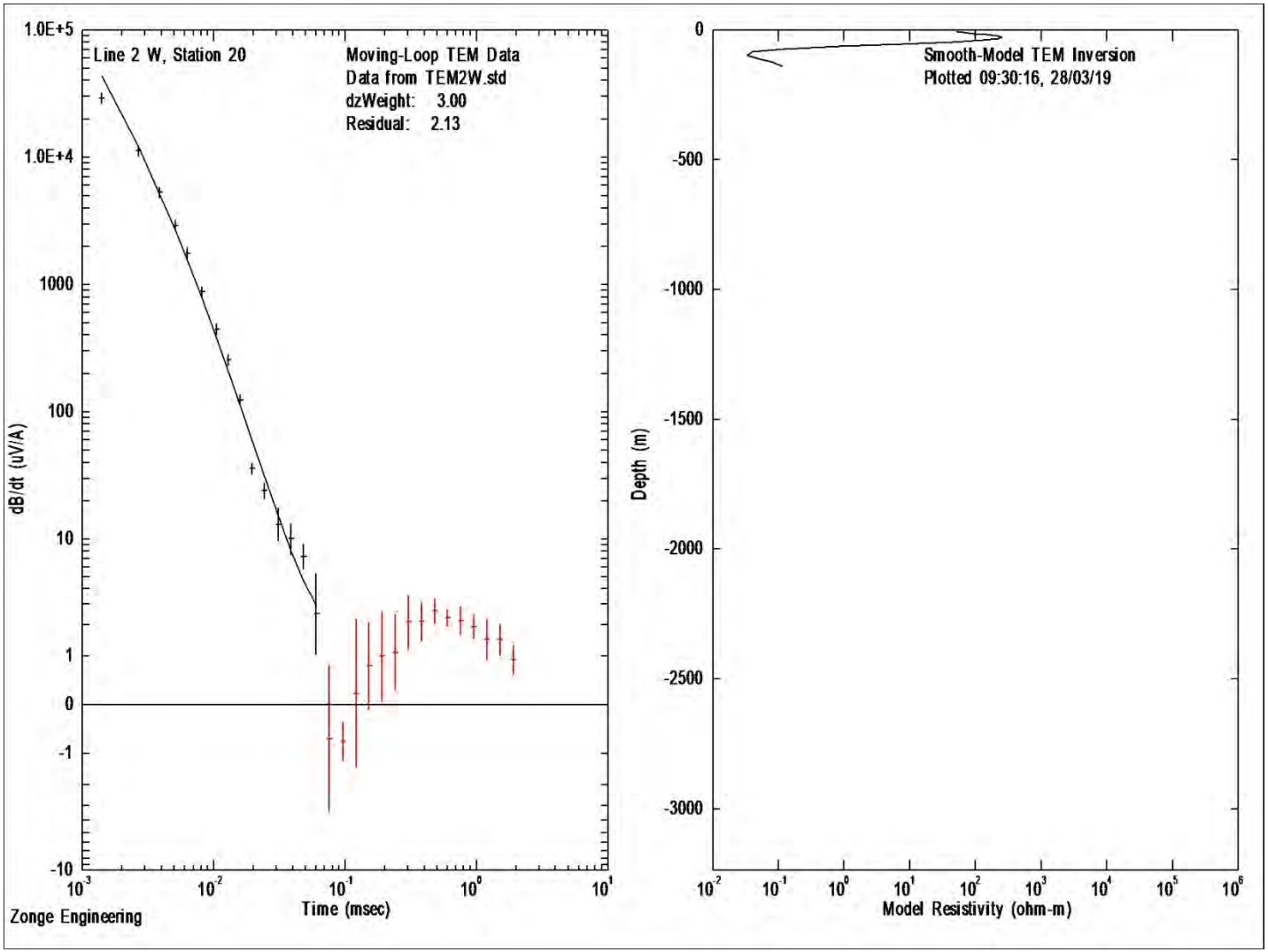

Figure 3.7c. Modeled and transient curve Line 2, Loop 3.

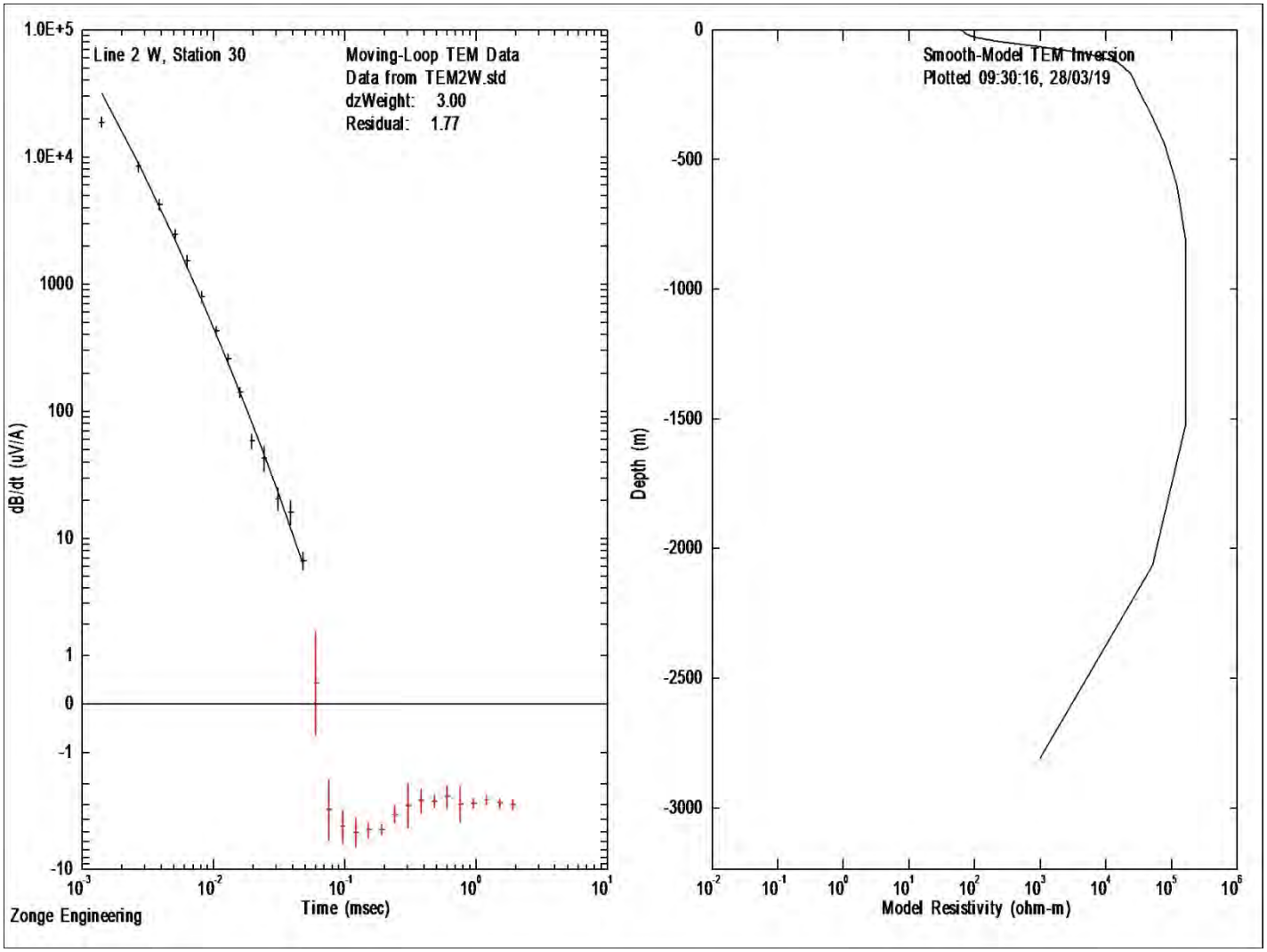

Figure 3.7d. Modeled and transient curve Line 2, Loop 4.

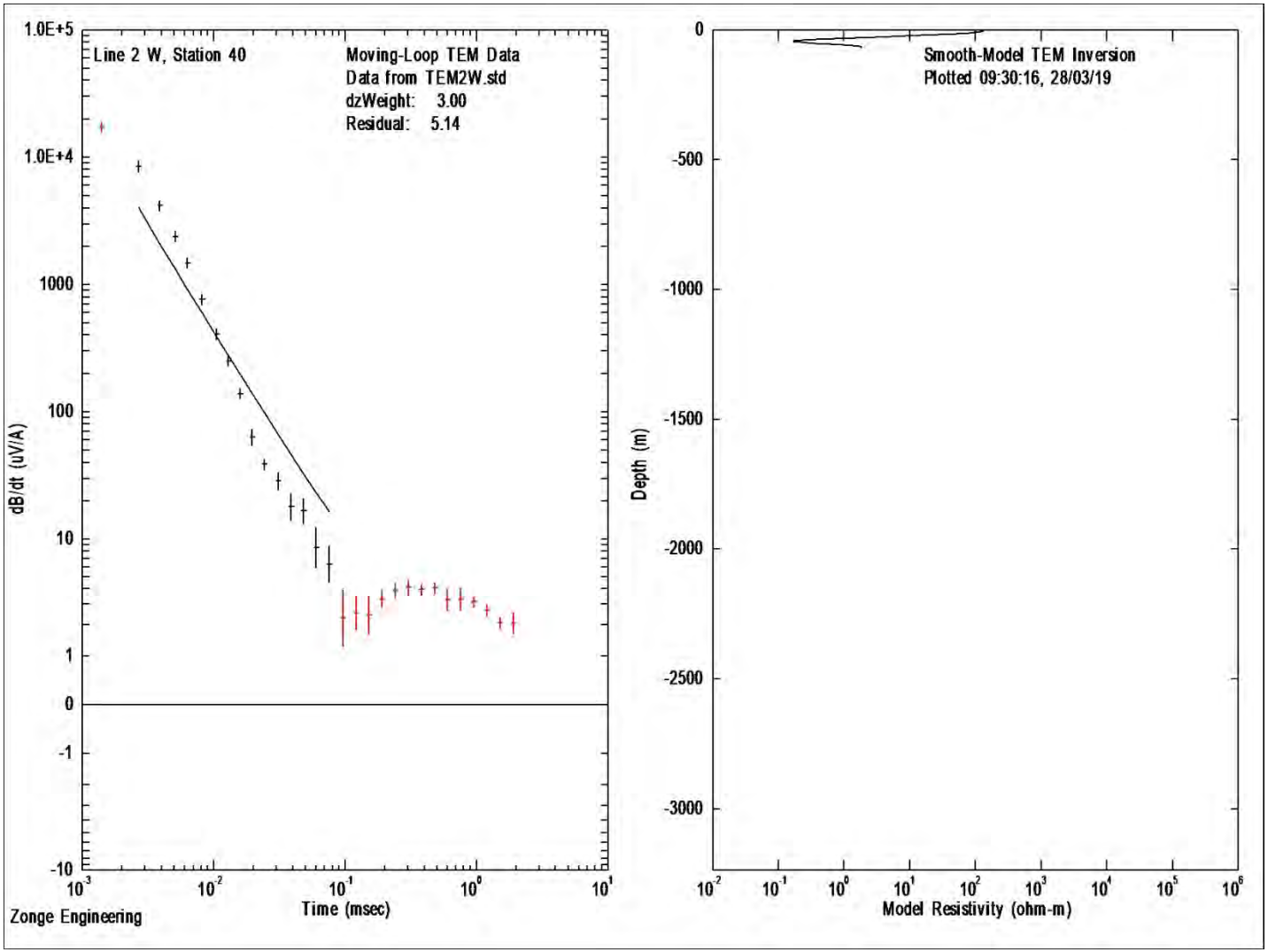

Figure 3.7e. Modeled and transient curve Line 2, Loop 5. Not included in inversion (Figure 3.5).

3.5 References

BGR, 2019, Transient electromagnetics (TEM), https://www.deutsche-rohstoffagentur.de/EN/Themen/GG_Geophysik/Bodengeophysik/Transienten_EM/tem_inhalt_en.html, accessed April 11, 2019.

Garmin, 2019, GPS Accuracy, https://support.garmin.com/en-US/?faq=aZc8RezeAb9LjCDpJplTY7, accessed April 15, 2019.

Zonge International, 2019, Transient Electromagnetic of Time-Domain EM (TEM), http://zonge.com/geophysical-methods/electrical-em/tem/, accessed April 4, 2019.

4. DC Resistivity Survey

4.1 Introduction

DC resistivity is a geophysical method that helps us understand and map variations in resistivity in the subsurface. It uses sets of two electrodes to input an electrical current into the ground and measure the resulting voltage. These measured voltages are then converted into apparent resistivity using Ohm's law, where resistance is proportional to voltage divided by current (Zonge International, 2019). Apparent resistivity, or resistance per unit volume, is the measured electrical resistivity between two points in the Earth, assuming that the Earth is homogenous and isotropic.

Some earth materials, such as metals and certain minerals like graphite, have low resistivity values and conduct electricity well. Other rocks and minerals are natural insulators. Groundwater contains dissolved compounds, which enhances its ability to conduct electricity. The more pore spaces there are in a rock, the more groundwater it could contain, and thus much of the variation in resistivity is mostly a function of fluid content and porosity (Burnley, 2016). This relationship between resistivity, water saturation, and porosity is defined by an empirical formula known as Archie's Law, which is given as

$$\rho = \frac{\alpha \rho_w}{\varphi^m S_W^n}, \tag{4.1}$$

where α, m, and n are empirical constants with typical values α=1, m=2, n=2; ρ_w is the resistivity of water; ρ is the observed resistivity; φ is the fractional porosity; and S_W is the fractional water saturation.

The calculation of apparent resistivity depends on the geometry of the electrode configuration used. The method used in this survey is a dipole-dipole DC array. This type of array consists of an electrode pair—A and B—that injects current into the ground, which is then read by the voltage (potential) pair—M and N. The apparent resistivity measured from these four electrodes is plotted at a point that is half way in between the two electrode pairs and at a depth that is half of the distance between the electrode pairs (Figure 4.1).

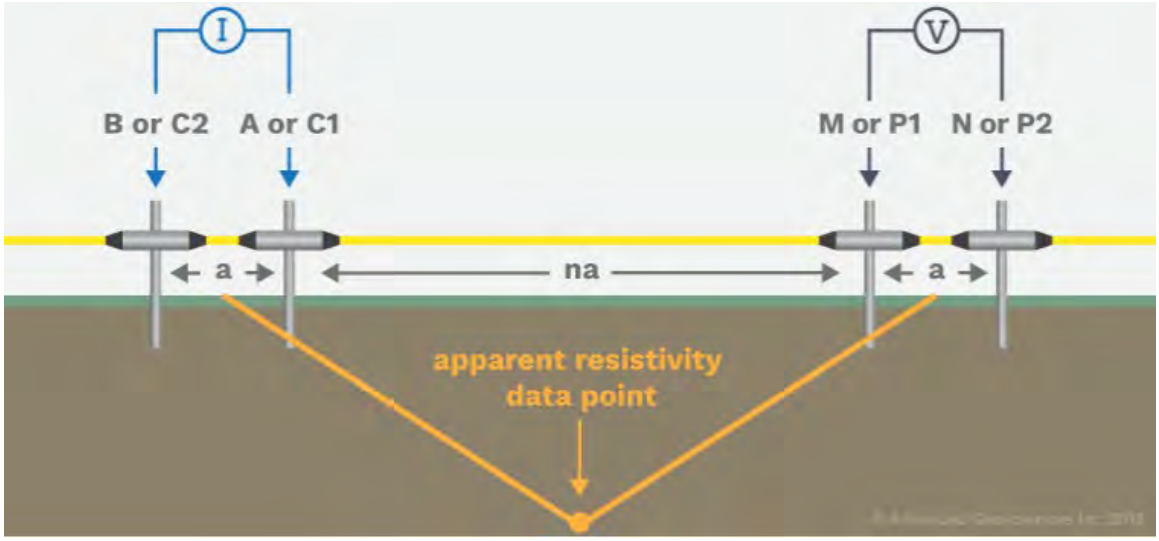

Figure 4.1. Diagram of an electrode pair used to calculate apparent resistivity at a specified point. The 'I' represents the current source and the 'V' represents the measured voltage (potential). Reproduced from Advanced Geosciences Inc. (2017).

The apparent resistivity values are plotted as a pseudosection, which is a distorted and rough version of the actual picture (Advanced Geosciences Inc., 2017). To construct the pseudosection, the apparent resistivity data points are plotted as a measurement of depth of penetration from the surface. The measured resistivity values are plotted along lines angled at 45°. A representation of this plotting geometry is shown in Figure 4.2. The apparent resistivity at each point is defined by the following equation,

$$\rho_\alpha = \frac{V}{I}\pi an(n+1)(n+2), \tag{4.2}$$

where ρ_a is the apparent resistivity; *V/I* is the impedance in Ohms; *a* is the distance between electrodes; and *n* is the number of spacings (multiples of *a*). To get a more accurate model of the subsurface from the measured apparent resistivity, the data collected are inverted into a modeled resistivity depth section. This provides a clearer analysis that takes into account the inhomogeneous nature of the earth, anisotropy ratios, and elevation differences between electrodes (Zonge International, 2019).

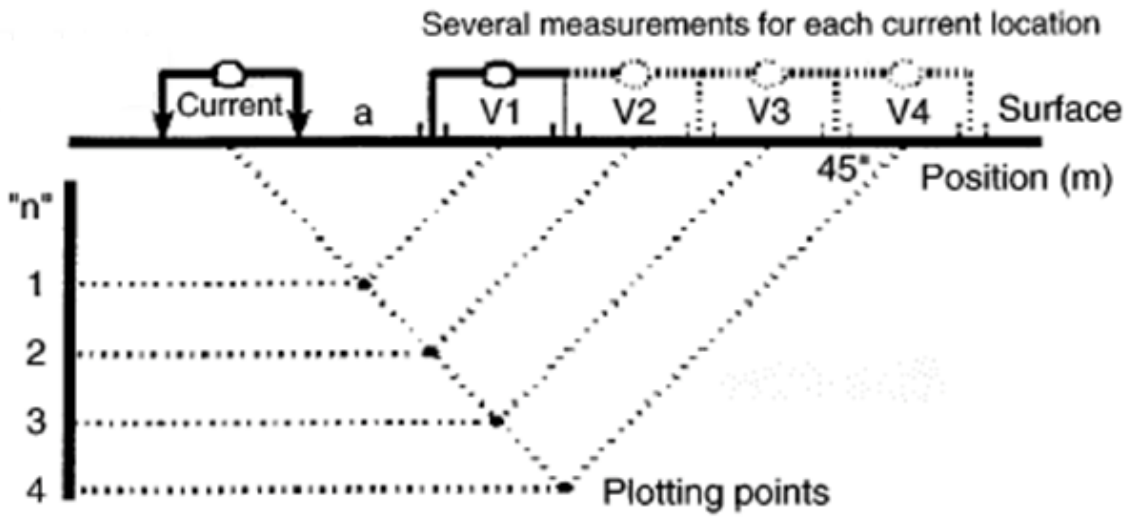

Figure 4.2. Diagram showing the construction of data point placement used in the creation of a pseudosection. The "n" is the spacing between current and potential electrode pairs. Reproduced from Landviser, LLC (2016).

4.2 Instrumentation and Field Procedures

Two DC dipole-dipole array lines were used for this study site. The two survey lines were laid on different days: the first was laid on February 16, 2019, and the second line on February 17, 2019. Each line consisted of 28 stainless steel electrodes, placed every ten meters, for a survey length of 280 m. The electrodes were attached to steel stakes inserted into the ground to a depth of at least 10 cm. A saline solution was then poured onto the ground at each stake location to increase the conductivity between the stake and the ground.

The first line trended at an azimuth of 260°/80°, starting near Harshaw Creek Road and ending past some of the old mine adits. The first DC line ran roughly in the center of the 20 m loop TEM line. The second line was placed parallel to the first line at a distance of 100 m to the south to get information on the tailings area (Figure 4.3).

The data were collected using an Advanced Geosciences Inc. (AGI) Sting R1 resistivity meter, along with an AGI Swift Resistivity switch box that allowed automatic switching between channels. Automatic switching isolates the individual electrodes for multiple electrode sender and receiver configurations and

consequently provides a more detailed subsurface map of the area. During the study, the system used was powered by a 12 V battery. The maximum voltage and current used were 400 V and 200 mA, respectively.

4.3 Data Processing

The collected apparent resistivity data were processed using AGI's EarthImager 2D software and inversion methods. Figures 4.4 and 4.5 show the measured, calculated, and inverted sections for both lines. These figures were processed and produced by Jamie Macy of the USGS.

4.4 Interpretation and Conclusions

The model shown in Figure 4.4 contains a large resistive body from approximately 65 to 140 m bounded by conductive bodies that extend to the bottom of the section and are likely deeper. In Figure 4.5, the model section contains a similar relationship of a large resistive body bounded by conductive bodies on either side, which could be the same feature seen in Line 1, as the second line runs parallel to the first line.

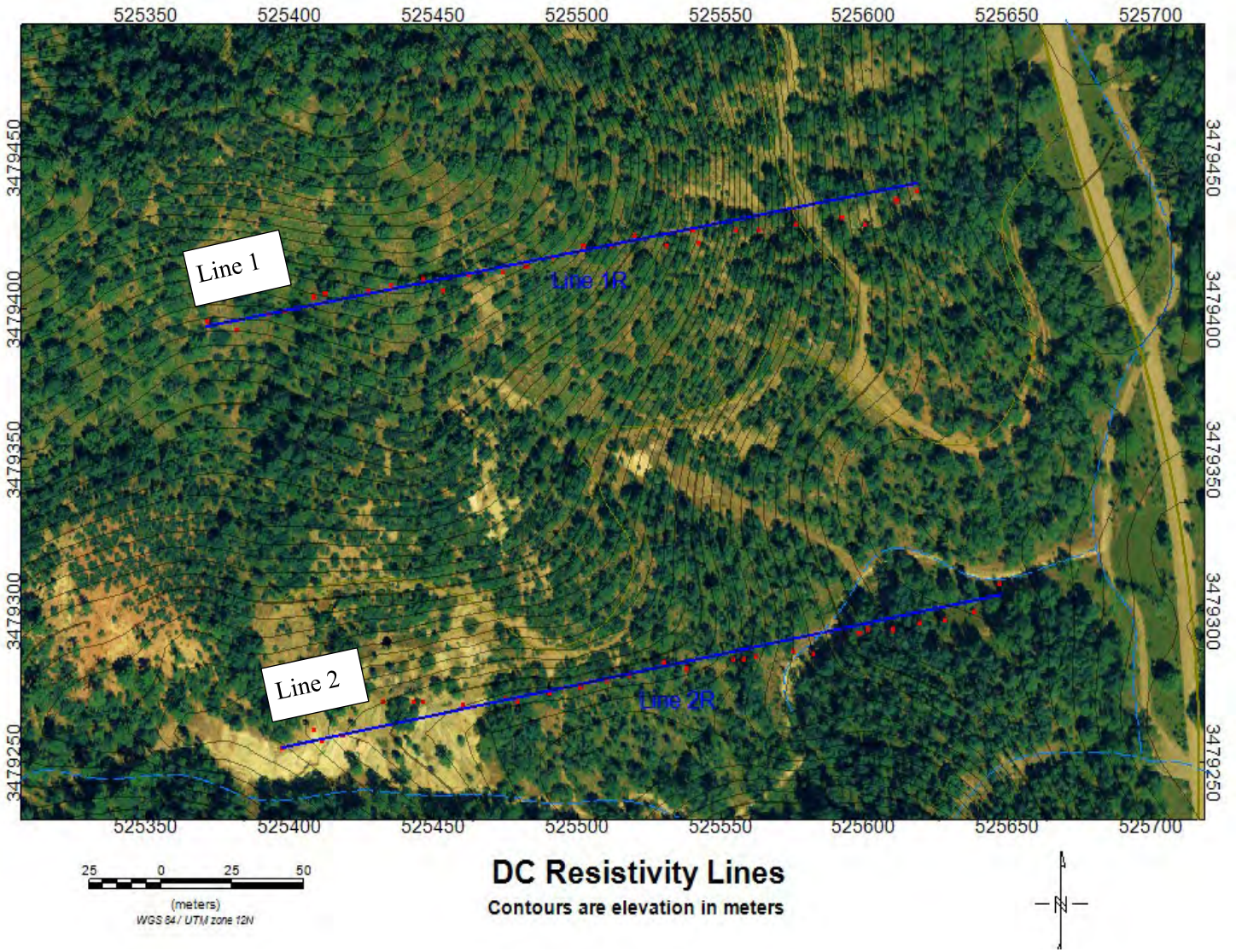

Figure 4.3. Location map showing the DC resistivity lines in blue. The red data points are GPS locations collected at each electrode.

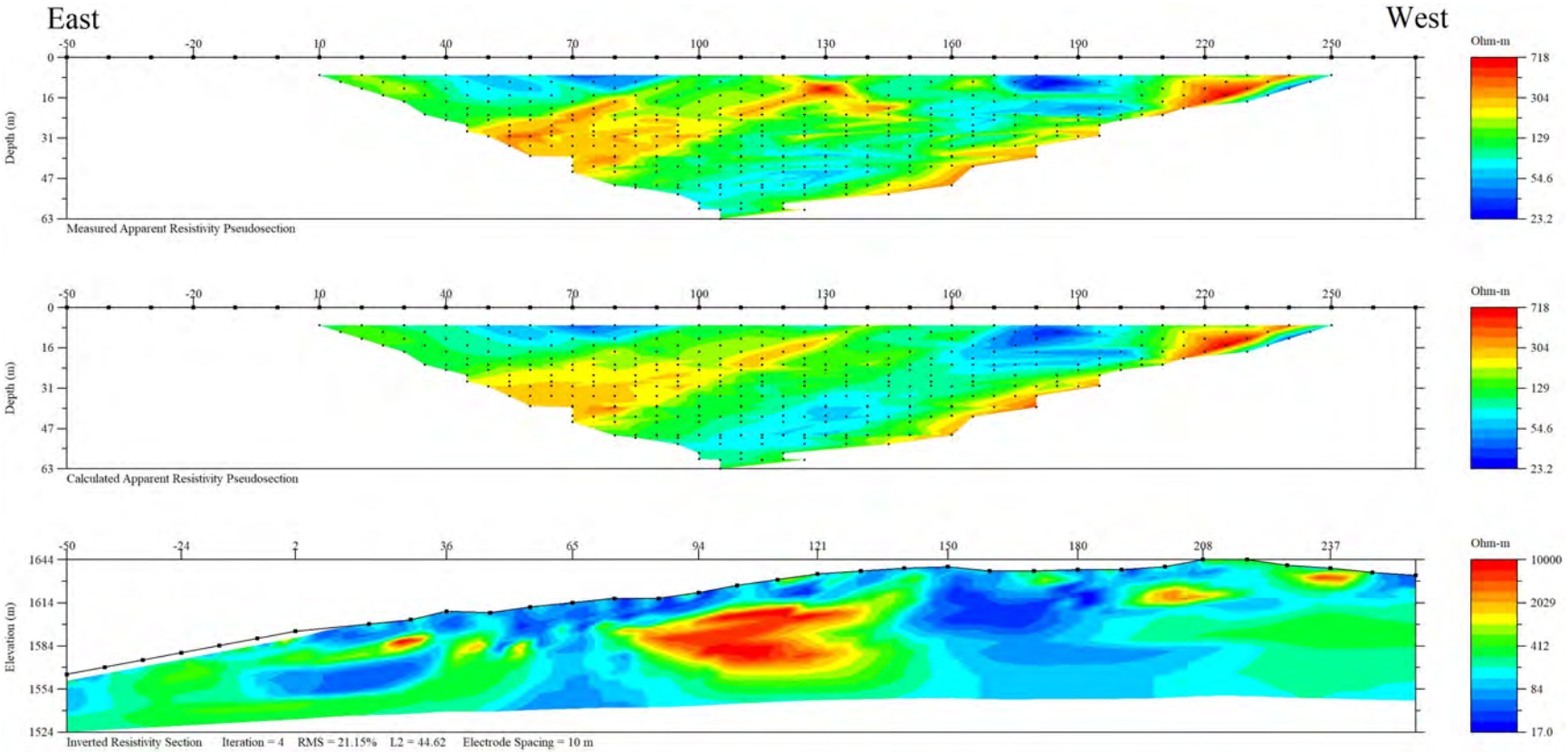

Figure 4.4. DC resistivity Line 1. The top and middle plots are the measured and calculated apparent resistivity, respectively. The bottom plot is the inverted resistivity model with topography. Plots prepared by Jamie Macy (USGS).

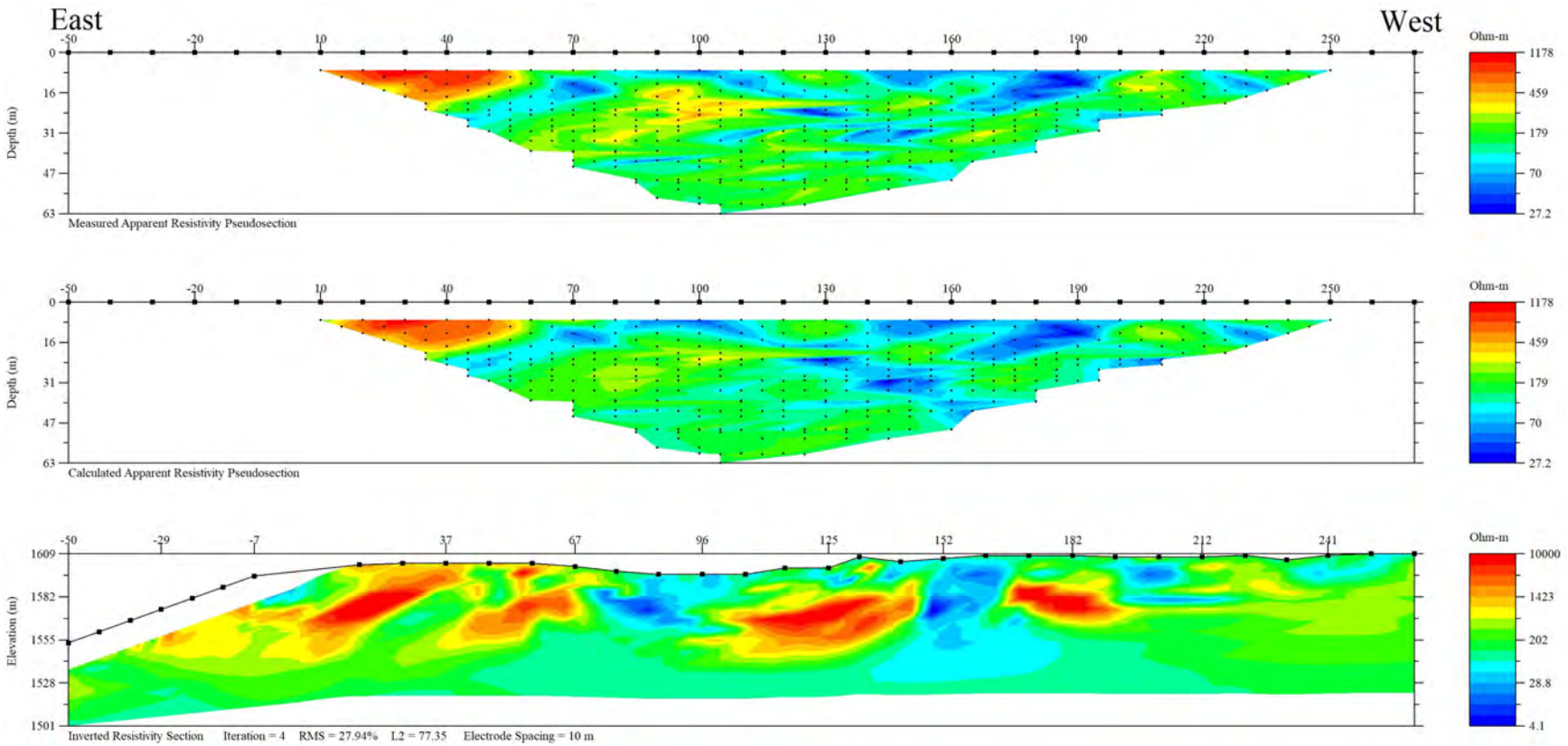

Figure 4.5. DC resistivity Line 2. The top and middle plots are the measured and calculated apparent resistivity, respectively. The bottom plot is the inverted resistivity model with topography. Plots prepared by Jamie Macy (USGS).

4.5 References

Advanced Geosciences Inc., 2017, Dipole-Dipole Array: Electrical Resistivity Methods, Part 3, https://www.agiusa.com/dipole-dipole%E2%80%8B-%E2%80%8Barray%E2%80%8B, accessed April 14, 2019.

Burnley, P., 2016, Resistivity of Earth Materials, https://pburnley.faculty.unlv.edu/GEOL442_642/RES/NOTES/ResistivityNotes06Rockres.html, accessed April 15, 2019.

Landviser, LLC, 2016, 2D Dipole-Dipole Electrical Tomography with LandMapper, http://www.landviser.net/content/2d-dipole-dipole-electrical-tomography-landmapper, accessed April 15, 2019.

Zonge International, 2018, DC Resistivity & Electrical Resistivity Tomography (ERT), http://zonge.com/geophysical- methods/electrical-em/dc-resistivity/, accessed April 10, 2019.

5. Electromagnetic Induction (EM-31 and EM-38) Survey

5.1 Introduction and Methods

An electromagnetic survey using Geonics EM-31 and EM-38 instruments was conducted on February 16, 2019 at the tailings area of the Blue Nose Mine study site, which is located just south and downhill of the existing mill foundation and north of the drainage. The Geonics EM-31 and EM-38 are widely-used geophysical instruments that measure apparent conductivity of the shallow subsurface. The purpose of the survey is to understand how the processed ore dumped beside the mill changed the conductivity of the subsurface, delineate the area covered by the tailings, and try to resolve information on the depth of the tailings material.

The two instruments used for the survey are the Geonics EM-31 and EM-38 Low Induction Number (LIN) tools, which are used to measure conductivity in the subsurface. The two instruments measure conductivity of the terrain by operating on the same principle. Each instrument consists of two coils separated by a set distance. At one end of the instrument, the transmitter coil induces a primary electromagnetic field into the ground at a fixed frequency. As the EM field travels through the subsurface, conductors in the ground generate eddy currents, which produce a secondary EM field. A receiver coil at the other end of the instrument then detects the strength of the secondary field, which is a measure of ground conductivity (McNeill, 1980).

The measured response is the apparent (bulk) conductivity of the ground and is given by the following formula (McNeill, 1980):

$$\sigma_a = \frac{4}{\omega \mu_0 s^2} \left(\frac{H_s}{H_p} \right), \tag{5.1}$$

where σ_a is the apparent conductivity (S/m); H_s is the secondary magnetic field at the receiver coil (T); H_p is the primary magnetic field at the receiver coil (T); ω is the frequency of the EM wave (rad); μ_0 is the magnetic permeability of free space; and s is the distance between transmitter and receiver coils (m).

5.2 Data Processing

Each instrument can be operated in vertical or horizontal dipole mode. The maximum depth of investigation for each instrument depends on the intercoil spacing and whether it is in vertical or horizontal mode. The intercoil spacing for the EM-31 is 3.66 m, and the intercoil spacing for the EM-38 is 1 m (Geonics Ltd., 2013). For vertical mode, the maximum depth of investigation is the intercoil spacing (s) multiplied by 1.5. For horizontal mode, the maximum depth of investigation is the intercoil spacing (s) multiplied by 0.75 (GeonicsTraining, 2014). The average investigation depth for each instrument can also be used to resolve thicknesses of conductive layers. The average investigation depth is where the material above and below each contributes half of the recorded signal. For the vertical dipole mode, it is 0.866 multiplied by the intercoil spacing, and for the horizontal modes it is 0.375 multiplied by the intercoil spacing (Sherriff et al., 2009).

	Intercoil spacing (s) [m]	**Maximum vertical depth (1.5*s) [m]**	**Maximum horizontal depth (0.75*s) [m]**	**Average vertical depth (0.866*s) [m]**	**Average horizontal depth (0.375*s) [m]**
EM-38	1	1.5	0.75	0.866	0.375
EM-31	3.66	6	3	3.17	1.3725
EM-31 operated at waist height	3.66	5	2	2.17	0.3725

Figure 5.1. Maximum and average depths of investigation for EM-31 and EM-38 based on operating mode (Sherriff et. al, 2009). The EM-31 average investigation depths change when the instrument is operated at waist height (approximately 1 m above the ground surface), so 1m is subtracted from those values.

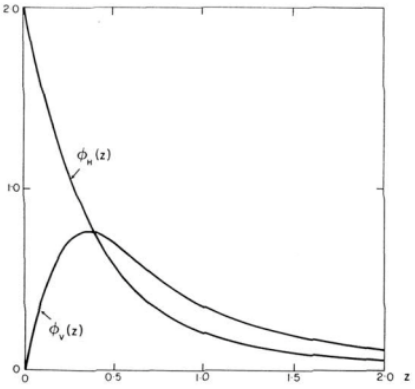

Figure 5.2. Instrument response as a function of depth (z) for vertical (Φ_V) and horizontal (Φ_H) dipole configurations. Reproduced from McNeill (1980).

5.3 Instrumentation and Field Procedures

The survey was conducted in part with the Geonics Limited EM-31 electromagnetic surveying instrument. A diagram for the operating modes is shown in Figure 5.3, and the operating panel for this instrument can be seen in Figure 5.4. The instrument is about 4 m in length when fully assembled. The magnitude of apparent conductivity is measured in milliSiemens per meter (mS/m), with an effective range of 0 to 1000 mS/m. The EM-31 has an intercoil spacing of 3.66 m, and it operates at 9.8 kHz, using 8 disposable alkaline "C" cell batteries. The measurement accuracy is +/- 5% at 20 mS/m (Geonics Ltd., 2013). The instrument has measurement ranges over which the scales can be adjusted so the reading can be more accurate. The available scales are 1000, 300, 100, 30, 10, and 3. The recordings taken for this survey used the scales of 100, 30, and 10, which proved to be the most accurate for this location. When used in vertical mode, the instrument has an effective sensing range of 2 to 5 m. When used in horizontal mode, the EM-31 has an effective sensing range of 0 to 3 m (Reynolds, 2011). We operated the EM-31 instrument at waist height approximately 1 m above the surface, which changed the average investigation depths and are noted in Figure 5.1.

The other instrument used for the survey was the Geonics EM-38-MK2-1 electromagnetic surveying instrument. It measures apparent conductivity in mS/m and also has an effective range from 0 to 1000 mS/m. The EM-38 has an intercoil spacing of 1 m and operates at a fixed frequency of 14.5 kHz, using a disposable 9 V battery. It has a measurement accuracy of +/- 5% at 30 mS/m (Geonics Ltd., 2013). The data are read on a digital display. The EM-38 was operated by placing the instrument on the ground to take the reading, which did not change the average investigation depth from the values given in Figure 5.1.

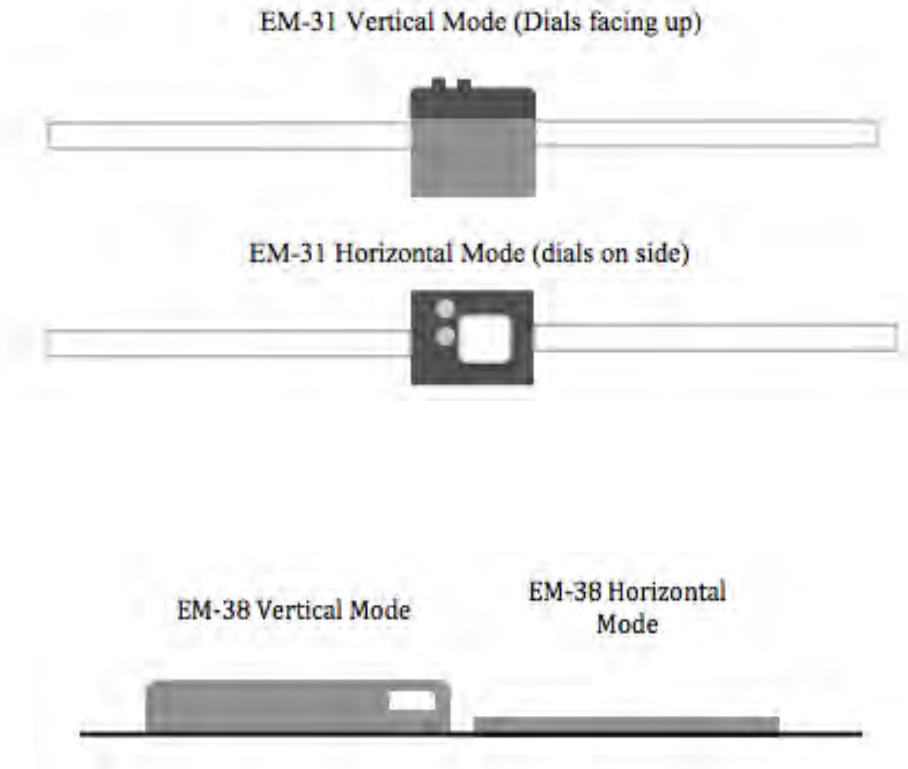

Figure 5.3. Diagrams of EM31 and EM-38 vertical and horizontal operating orientations.

Figure 5.4. Picture of the EM-31 operating panel.

5.4 Interpretation and Conclusions

Two profiles were taken with instrument readings in horizontal and vertical modes every 5 m using a 100 m tape-measuring reel. The first profile (Line 1) runs East to West and is 100 m in length. It starts about 15 m east of where we the visible tailings began, runs across the tailings, and ends about 20 m west of the visible tailings. The second line runs South to North and starts in the drainage that bounds the southern edge of the tailings, runs across the approximate middle of the tailings pile, and up the hill toward the still-existing concrete mill foundation. Line 2 is 35 m in length. GPS data were collected using a Garmin eTrex 10 handheld GPS unit along the line every 10 m for Line 1; and at positions -3, 0, 10, 20, 30, and 35 m for Line 2.

Based on the data collected over both profile lines, it is apparent that the tailings area, characterized by the bright orange and white clay-like material, is more conductive than the surrounding topsoil and native hillside. The surrounding native material tends to have average conductivity values below 8 mS/m in both vertical and horizontal readings of both the EM-31 and the EM-38. The colorful tailings material ranges in higher conductivity values of 8 to 60 mS/m (Figures 5.6 and 5.7). These higher conductivity values are most likely caused by residual ore metals leftover from mill processing and possibly from a higher water saturation than the surrounding material due to its clay-rich nature. Another source of conductivity that might have affected the survey is buried metal in the area, which is likely, as there was junk metal on the surface of the tailings that were moved away from the EM survey area.

Looking at Figures 5.9, 5.10, 5.11, and 5.12, the area covered by the tailings clearly stands out from the surrounding material, with high conductivity values represented by cool colors, and low conductivity values represented by warm colors. Data collected on both lines are similar, as they show the same trend of increased conductivity near the tailings dump and significantly lower values on the surrounding soil.

The pseudosections provided in Figure 5.13 indicate that the conductivity of the tailings material decreases with depth. The vertical thickness of the conductive material cannot be determined, though, as some of the high conductivity values continue to the bottom of the section. Future surveys could operate the EM-31 on the ground surface rather than at waist height to maximize the depth of investigation provided by the instrument or utilize an EM instrument with a larger intercoil spacing, possibly a Geonics EM34 instrument.

The electromagnetic survey conducted on the tailings area of the Blue Nose Mine study site shows that the EM-31 and the EM-38 were useful tools in distinguishing the conductivity of the processed tailings material from the surrounding native hillside and for mapping the conductivity variations along the profiles. When projected on the color conductivity maps, it is easy to delineate the conductive tailings from the more resistive surrounding soil. While the EM-31 and 38 instruments do not provide high-resolution depth images of the subsurface, they do provide limited resolution of the extent of conductivity with depth of the subsurface.

Figure 5.5. Picture of the tailings area looking west along Line 1. The bright orange and white colors are indicative of the conductive tailings material.

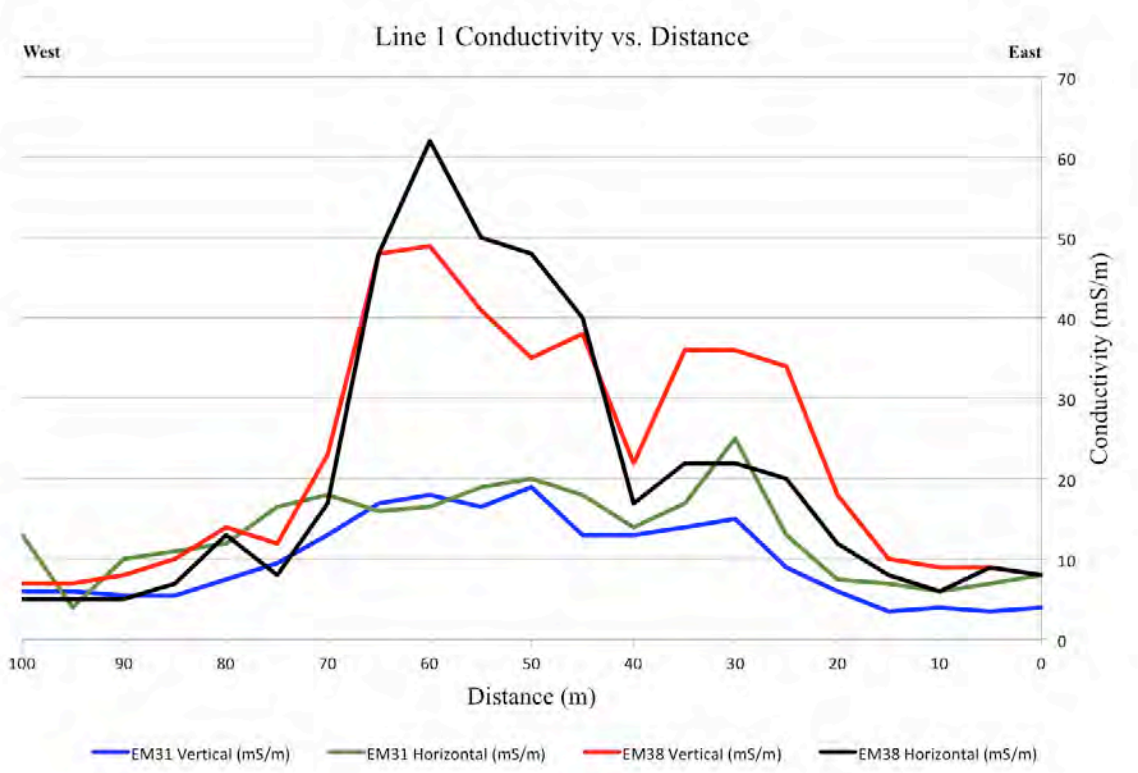

Figure 5.6. EM conductivity profile data for Line 1 going from West to East.

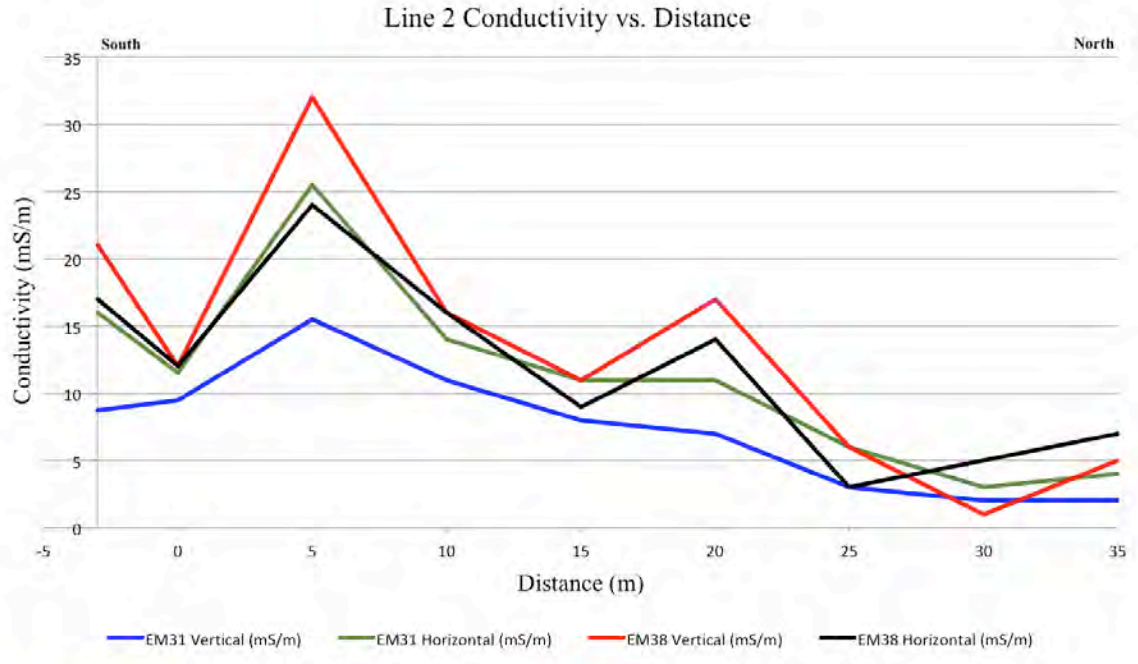

Figure 5.7. EM conductivity profile data for Line 2 going from South to North.

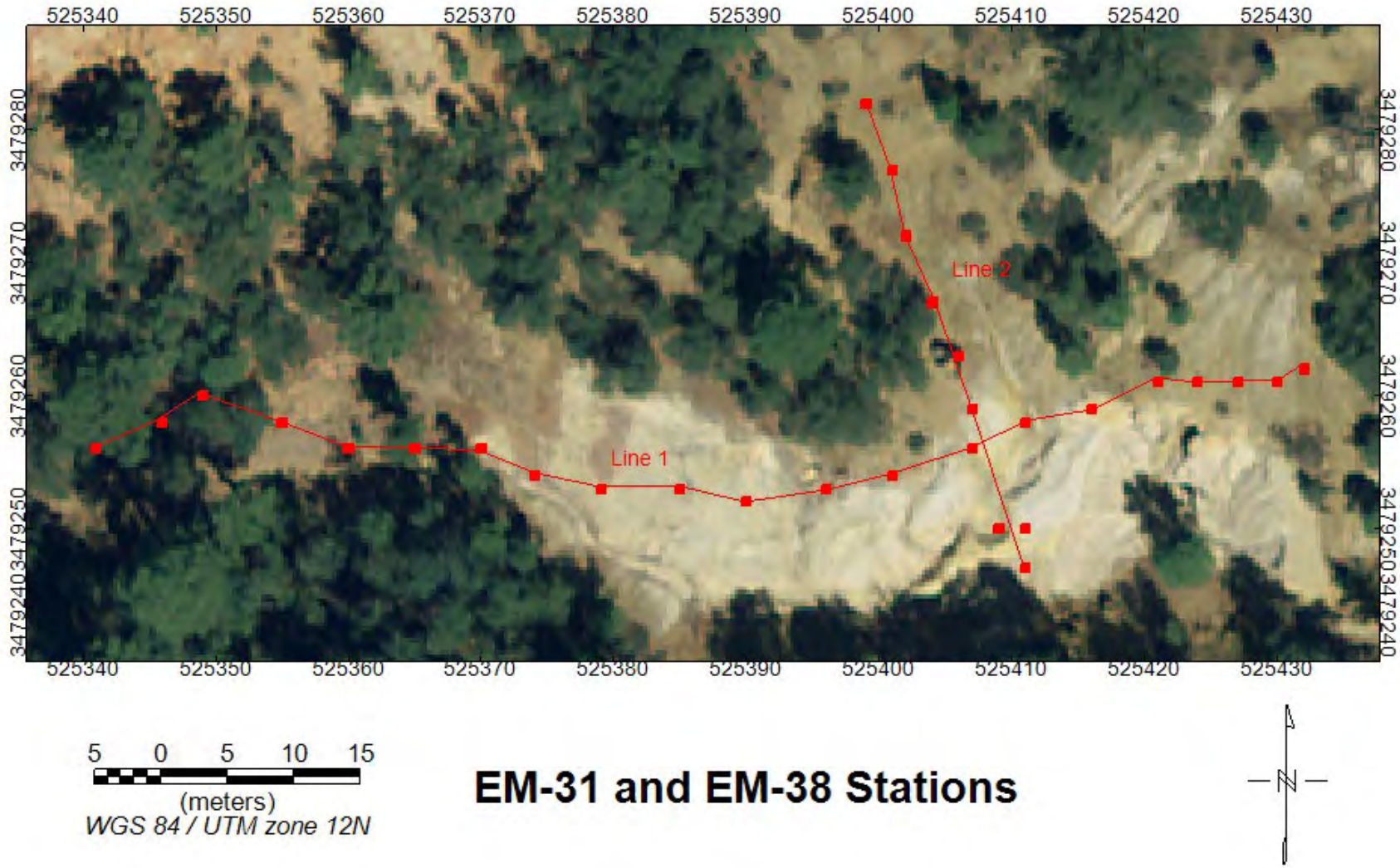

Figure 5.8. Map of the tailings area showing the data collection points. Location data collected using a Garmin eTrex 10 GPS unit. The light tan color and lack of vegetation of the tailings stands out from the surrounding area.

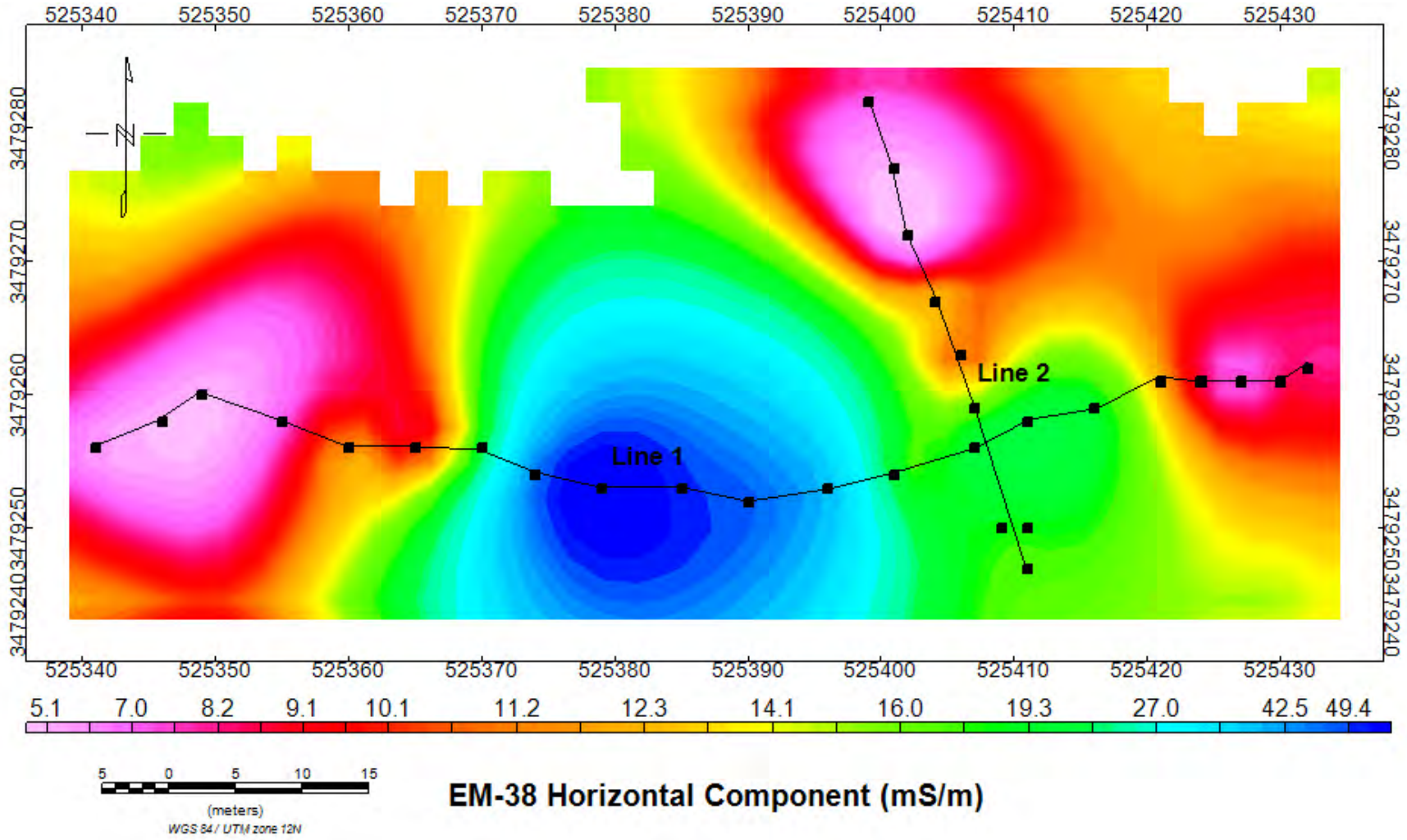

Figure 5.9. Surface color contour map of horizontal EM-38 readings at data collection points. Higher conductivity values shown in cooler colors.

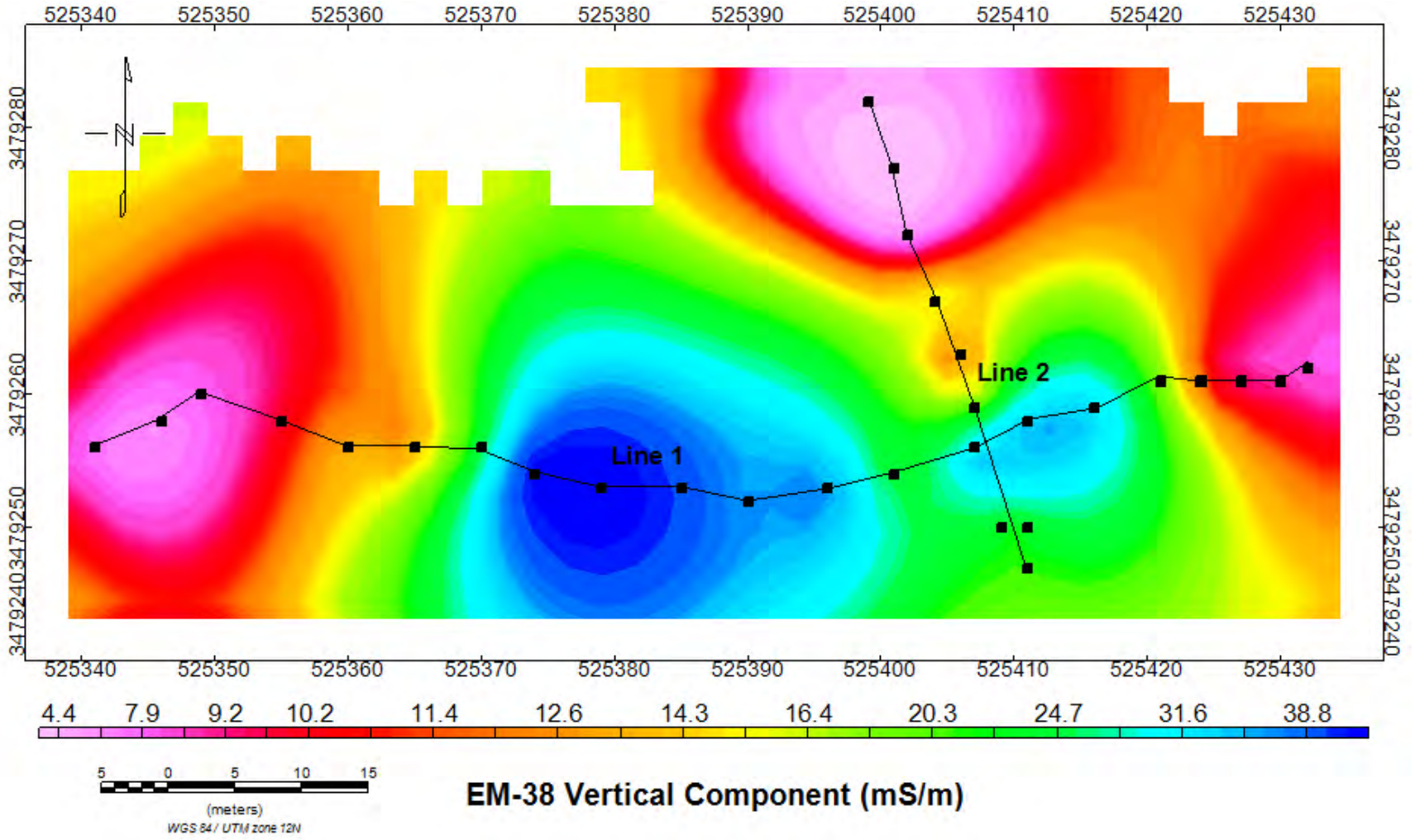

Figure 5.10. Surface color contour map of vertical EM-38 readings at data collection points. Higher conductivity values shown in cooler colors.

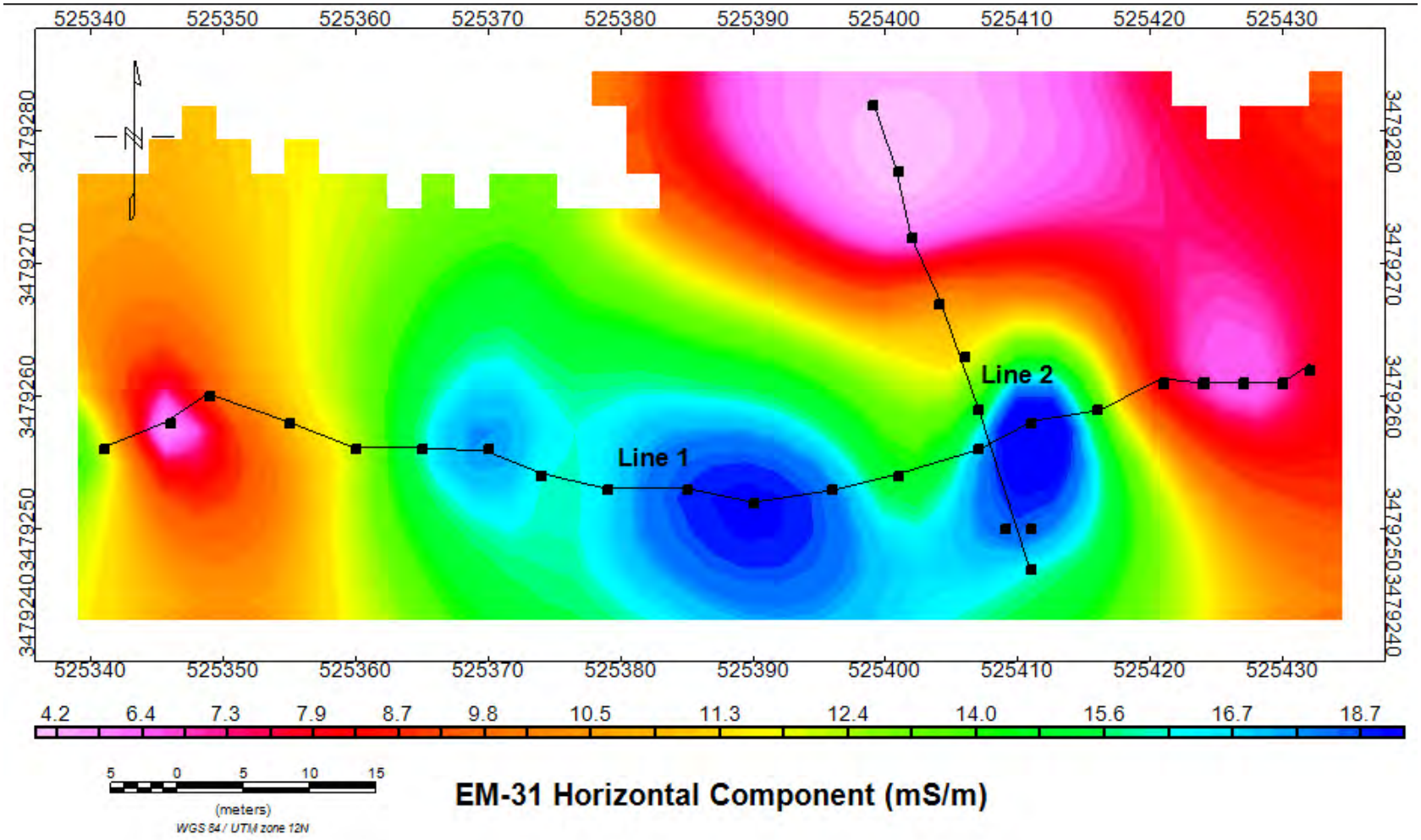

Figure 5.11. Surface color contour map of horizontal EM-31 readings at data collection points. Higher conductivity values shown in cooler colors.

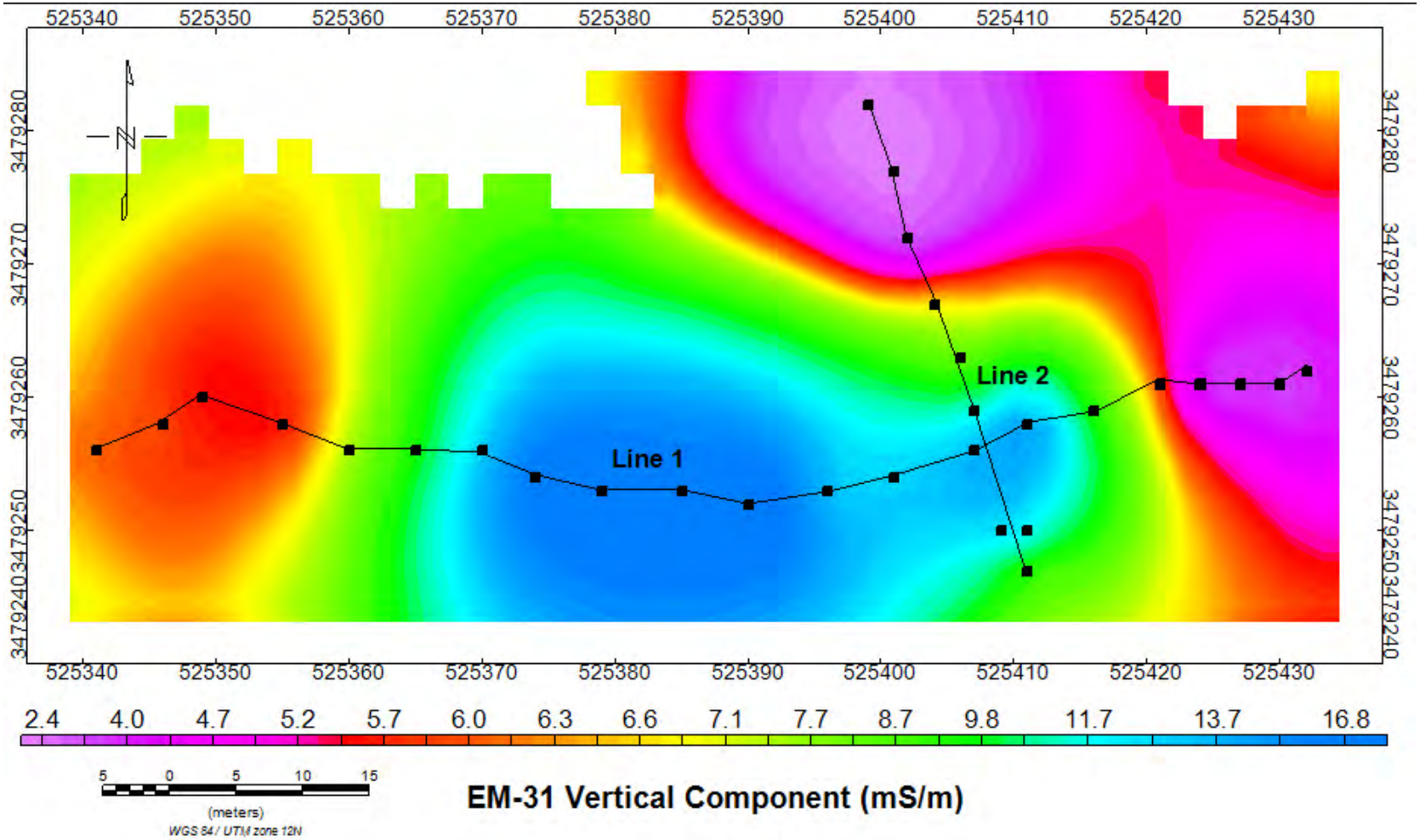

Figure 5.12. Surface color contour map of vertical EM-31 readings at data collection points. Higher conductivity values shown in cooler colors.

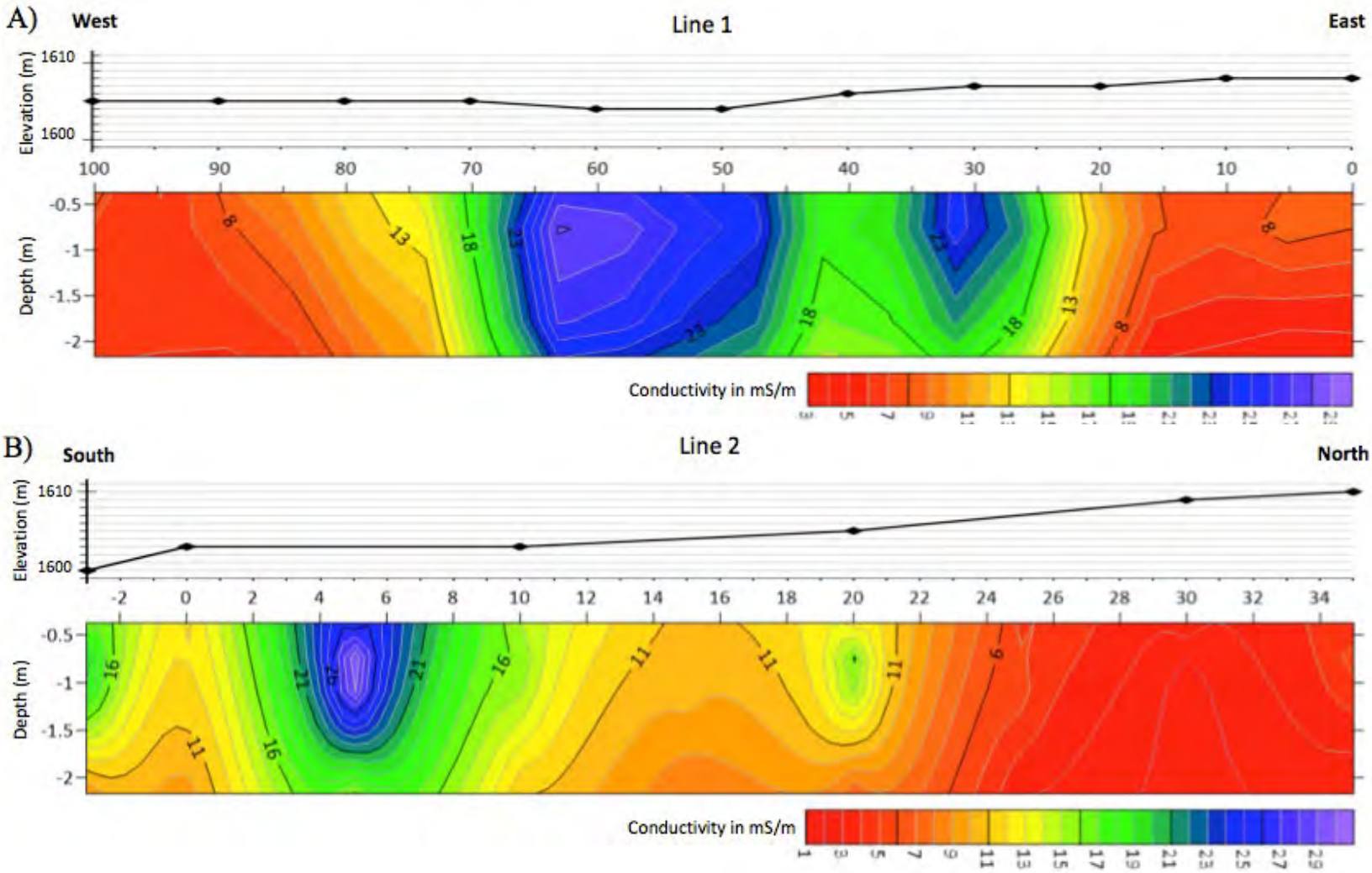

Figure 5.13. Pseudosections of the EM-31 and EM-38 apparent conductivity data with depth collected along **A)** Line 1 and **B)** Line 2 with accompanying elevation profiles plotted at the top. Apparent conductivity data are gridded using a kriging algorithm for the corresponding average depths for each instrument reading as listed in Table 5.1. Note that these figures are not a rigorous inversion of the data to determine true conductivity with depth. Elevation data collected using Garmin eTrex 10 GPS unit at marked intervals.

Line 1 Data					
Position	**EM-38 H**	**EM-38 V**	**EM-31 H**	**EM-31 V**	**Comments**
0	8	8	8	4	Waste rock slope
5	9	9	7	3.5	Waste rock slope
10	6	9	6	4	Waste rock slope
15	8	10	7	3.5	Waste rock slope
20	12	18	7.5	6	Waste rock slope
25	20	34	13	9	Orange / white tailings
30	22	36	25	15	Orange / white tailings
35	22	36	17	14	Orange / white tailings
40	17	22	14	13	Orange / white tailings
45	40	38	18	13	Orange / white tailings
50	48	35	20	19	Orange / white tailings
55	50	41	19	16.5	Orange / white tailings
60	62	49	16.5	18	Orange / white tailings
65	48	48	16	17	Orange / white tailings
70	17	23	18	13	Orange / white tailings
75	8	12	16.5	9.5	Orange / white tailings
80	13	14	12	7.5	
85	7	10	11	5.5	
90	5	8	10	5.5	Slight vegetation
95	5	7	4	6	
100	5	7	3	6	More vegetation
Line 2 Data					
-3	17	21	16	8.75	In the drainage
0	12	12	11.5	9.5	Edge of tailings
5	24	32	25.5	15.5	Orange / white tailings
10	16	16	14	11	Orange / white tailings
15	9	11	11	8	Orange / white tailings
20	14	17	11	7	On tailings, metal nearby
25	3	6	6	3	Off tailings upslope
30	5	1	3	2	
35	7	5	4	2	Concrete foundation nearby

Table 5.1. Data table showing EM-38 and EM-31 horizontal and vertical orientation readings in mS/m and notes on the surrounding area that could have an effect on the instrument response. Position for Line 1 starts at 0 m on the East end of the line and ends at 100 m at the West end of the line. Position for Line 2 starts at -3 m on the South end of the line and ends at 35 m on the North end.

Position Locations for Line 1				
	UTM Coordinates			
Position (m)	**Zone**	**Easting**	**Northing**	**Elevation**
0	12R	0525432	3479262	1608
10	12R	0525427	3479261	1608
20	12R	0525421	3479261	1607
30	12R	0525411	3479258	1607
40	12R	0525401	3479254	1606
50	12R	0525390	3479252	1604
60	12R	0525379	3479253	1604
70	12R	0525370	3479256	1605
80	12R	0525360	3479256	1605
90	12R	0525349	3479260	1605
100	12R	0525341	3479256	1605
Position Locations for Line 2				
-3	12R	0525411	3479247	1600
0	12R	0525411	3479250	1603
10	12R	0525407	3479259	1603
20	12R	0525404	3479267	1605
30	12R	0525401	3479277	1608
35	12R	0525399	3479282	1610

Table 5.2. GPS based locations and elevations for Line 1 and Line 2 collected using a Garmin eTrex 10 handheld unit.

5.5 References

Geonics Ltd., 2013, EM31-MK2 EM31-SH, http://www.geonics.com/html/em31-mk2.html, accessed March 24, 2019.

GeonicsTraining, 2014, Geonics Training EM-61 EM-31 EM-34 EM-38, http://geonicstraining.com/compare-geonics-em31-and-em38/, accessed April 5, 2019.

McNeill, J.D., 1980, Electromagnetic terrain conductivity measurement at low induction numbers, Geonics Ltd., Technical Note TN-6.

Reynolds, J.M, 2011, An Introduction to Applied and Environmental Geophysics, John Wiley & Sons Ltd, Chichester, 712 pp.

Sherriff, B. L., et al., 2009, A geophysical and geotechnical study to determine the hydrological regime of the Central Manitoba gold mine tailings deposit, Canadian Geotechnical Journal, **46**, no. 1, 69-80.

6. Ground Magnetic Survey

6.1 Introduction and Methods

A two-dimensional total-field magnetic dataset was collected at the Blue Nose Mine property as part of a larger environmental study of the area. The magnetic data provide a spatial representation of mineralization and structures which help in determining areas of high sulfide content or intrusive bodies which may direct the subterranean flow of water. Our goal is to use spatial variations in magnetic anomalies to determine underlying mineralization (or mineral deposits) and any distinguishable features which produced hydrothermal mineralization in void spaces. Magnetic surveys distinguish different underlying materials based on differing magnetic properties. When conducting a survey, the instrument registers magnetic fields based upon spatial and temporal variations.

Total magnetic field is produced by three main sources: Earth's outer core, solar wind passing through Earth's ionosphere, and any anomalies beneath the Earth's surface (Likkason, 2014). Temporal variations in magnetic strength are mostly dependent on solar flares from outer space. Although these variations are small in amplitude (on the order of nT), measurements of the magnetic field can be heavily affected by them due to their high frequencies. Temporal variations can be accounted for by using a base station. The data recorded at the base station is subtracted from measurements collected in the field.

Assuming the Earth's magnetic field is spatially uniform within the field site, and using a base station for temporal variation corrections, the resulting spatial variation that emerges is interpreted to be due to geologic lithology and mineralization. These minerals, especially iron-bearing ones, change the ambient field from one lithology to the next (Chon et al., 2016). The localized subsurface bodies will constructively and destructively interfere with the background magnetic field (Earth's field and any solar radiation). Interference will produce varying total magnetic field at different spatial points within the field site.

Various minerals can be magnetized in different orientations by inducing fields or measuring remnant fields, and are procured in primary or secondary events. Established magnetism can also be altered due to heating and realignment of existing magnetism, chemical alteration, and other processes (Lyatsky, 2010). Not only do subsurface materials have differing alignments, the bodies maintain different magnetic magnitude. The magnitude variations emerge based on magnetic susceptibility of the material, its orientation and distribution, and in the case of iron-bearing materials, the time of its freezing below the Curie temperature during formation (Chon et al., 2016). Overall, the instrumentation measures the total magnetic field at a specific location. Thus, during data processing, correction factors and data interpolation produce spatial maps displaying the varying magnetic field over the Blue Nose Mine field site.

6.2 Instrumentation and Field Procedures

Total-field magnetic measurements were taken at the surface by personnel utilizing an Overhauser GSM-19 portable magnetometer. Field readings were measured in nanoteslas (nT) along a total of 10 East/West trending lines that were 300-315 m in length with a 15 m spacing between each station. Each line was also spaced 15 m to the North/South in order to facilitate the collection of a complete and consistent grid. Station locations and relative elevations were established utilizing a Garmin Foretrex 601 MIL-STD and a Nikon Forestry Pro Laser Range Finder with location coordinates in the UTM format and all distances recorded in meters. Certain station locations were adjusted and/or survey lines were shortened in the event of impassable terrain. In addition to the primary survey area, two higher resolution surveys were conducted over the primary mine tailings with a station spacing of 5 m and a total survey line length of 100 m East/West and 40 m North/South.

A second magnetometer was set up in a stationary location (base station) in order to capture geomagnetic variations and monitor for excessive magnetic noise which would obscure data collection. These stationary readings were taken at five-minute intervals at all times when the portable magnetometer crew was taking measurements. The base-station location was near the origin point of our survey grid.

6.3 Data Processing

The total-field data were imported into Geosoft software and rendered into color imagery (Figure 6.2). The total-field data were then corrected for external field strength effects (not geometric effects) by subtracting out the linearly-interpolated base station data (Equation 6.1). The resulting value is known as the residual field and should be free of time-domain fluctuations in the magnitude of the geomagnetic field. The result of this correction is seen in Figure 6.3. The plot resulting from this residual field is useful, however interference from negative field values make it less accurate than the final product. Two types of mathematical correction were applied in order to increase the spatial accuracy of the plot.

$$B_{residual} = B_{total} - B_{base} \tag{6.1}$$

The first is correction is known as analytic signal filtering. This is achieved by utilizing an analytic signal or total gradient filter, which is a product of the combination of the horizontal and vertical gradients of a magnetic anomaly. This calculation does not depend on the direction of magnetization and will produce the maximum value directly over a given anomaly source. This filter is computed using the Hilbert transform, which is a complex function where the real

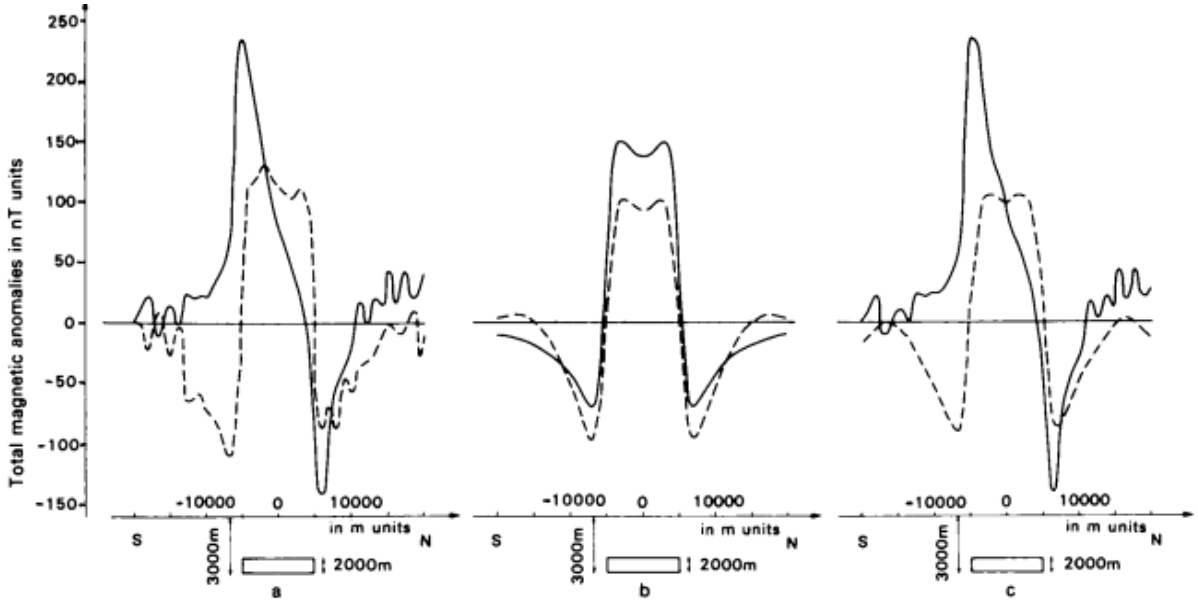

Figure 6.1. Example of pole reduction, where the solid line is uncorrected magnetic data, and the dashed line is corrected magnetic data. Reproduced from Kis (1990).

component represents the horizontal gradient of magnetic field intensity, and the imaginary represents the vertical gradient (Ansari and Alamdar, 2009). This function is fast Fourier transformed into the frequency domain and signals are then differentially weighted based on the sign of their wavenumber. This reweighted function is then transformed back into the spatial domain for display and interpretation. The result of this correction is seen in Figure 6.5.

The second correction used in this study is called pole reduction. This correction is similar to the analytic signal in that it eliminates negative field effects, however the pole reduction filter also corrects for the difference between apparent anomaly locations and their actual location. This slight shift in location is due to the dipole orientation of large-scale fields with far away sources, which is mainly the Earth's magnetic field, although effects from any field that can be represented as a point source can be corrected in this way. The effect of pole reduction on a magnetic anomaly can be seen by a sample 2D prism in Figure 6.1. Note how the anomaly flattens out a bit and shifts after the correction. The result of a pole reduction correction in our field area is seen in Figure 6.4. Pole reduction may be carried out in several ways, the most common of which uses a double (two dimensional) fast Fourier transform to find solutions to a finite series of trigonometric functions that involve the magnetic inclination and declination of the external field (Kis, 1990; Ervin, 1976).

6.4 Interpretation and Conclusions

Several linear features are apparent in both the pole reduced and analytic signal data, and are highlighted in Figure 6.6. Solid lines represent clear lineations, and dotted lines indicate less clear or inferred lineations. The Harshaw Creek fault is readily visible in the valley on the eastern side of the imagery and is labeled HCF. This structure is a large normal fault system which dips to the west and places altered Cretaceous shallow marine sediments alongside Paleozoic carbonates and other deep marine lithologies.

The final plot also shows a very high magnitude trend just to the west of the Harshaw Creek fault. It has a residual amplitude of up to 280 nT and is the largest anomaly in the field site. Given the very high amplitude of this anomaly, we can conclude that it is probably caused by

high-susceptibility ferrimagnetic minerals, such as pyrrhotite or magnetite. Pyrrhotite and magnetite are often found in association with chalcopyrite and other sulfide minerals. The Blue Nose Mine produced secondary copper from a chalcopyrite ore containing pyrite and other sulfides. Clearly, the observed anomaly could be produced by mineralization known to exist in the area. It is worth noting that this high amplitude anomaly is not the site of the old mine workings; however, its relationship to the metasomatic mineralization at the Blue Nose Mine is not clear. It is possible that this anomaly is an intrusive body which supplied the metasomatic fluids that buffered when contacting the calcareous Cretaceous sediments, but further analysis is needed in order to confirm this theory. Using the slope method described in Telford et al. (1990), we can make a rough estimate of the depth to the intrusive body, following

$$h = k_1 S; \quad 1.67 \leq k_1 \leq 2.0, \tag{6.2}$$

where *S* is the horizontal extent of the region of maximum slope at the flank of the anomaly; *h* is the depth to the anomaly; and k_1 is an empirical constant. Using S=9.4 m, we can expect a depth to the intrusive body between 15.7 m and 18.8 m.

The magnetic survey was successful at identifying several geologic features which may have an impact on the overall restoration project at the Blue Nose Mine. Data quality was good, and the survey was free of any significant noise from cultural or geomagnetic sources.

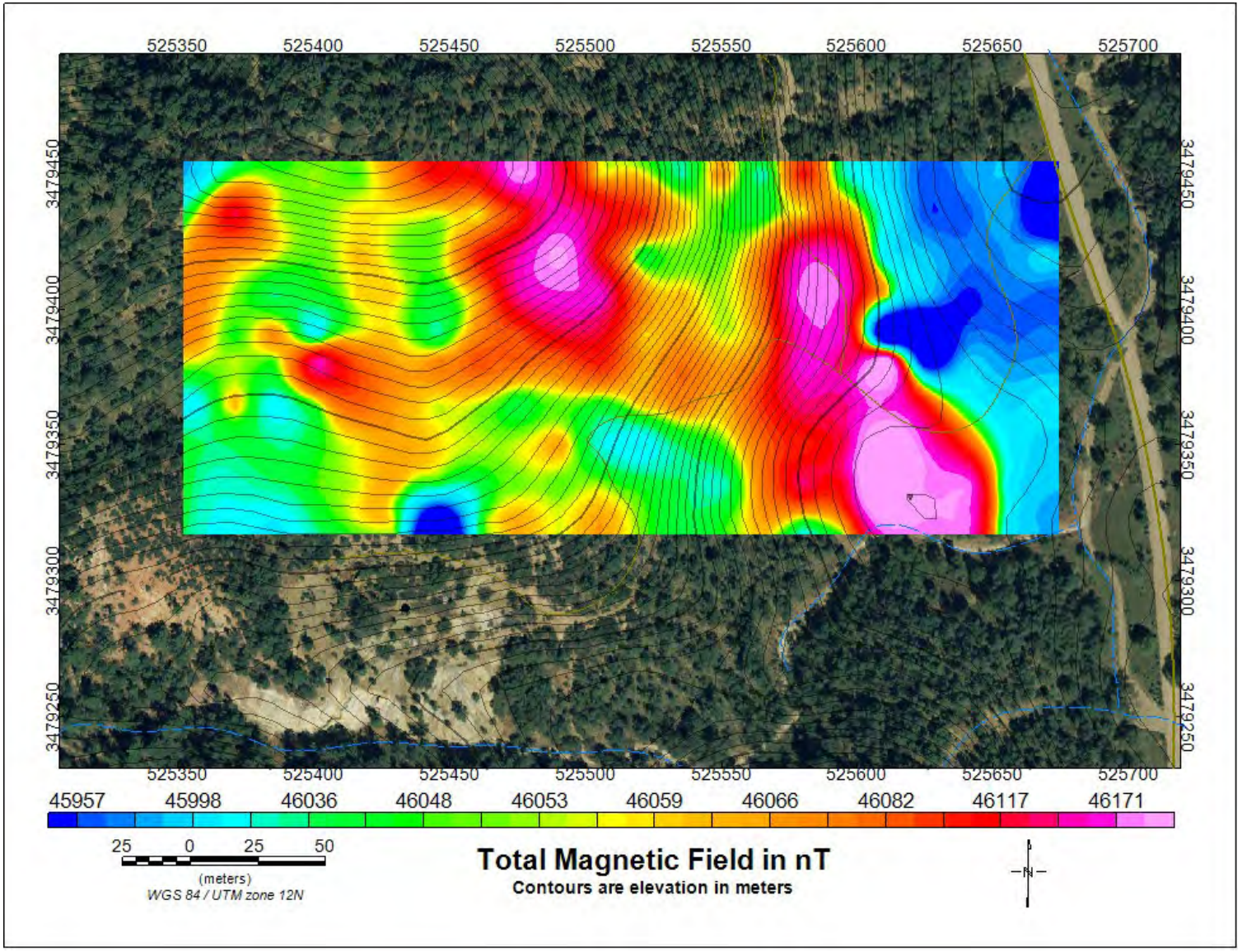

Figure 6.2. Total magnetic field (nT) interpolated from raw data collected across entire Blue Nose Mine field site.

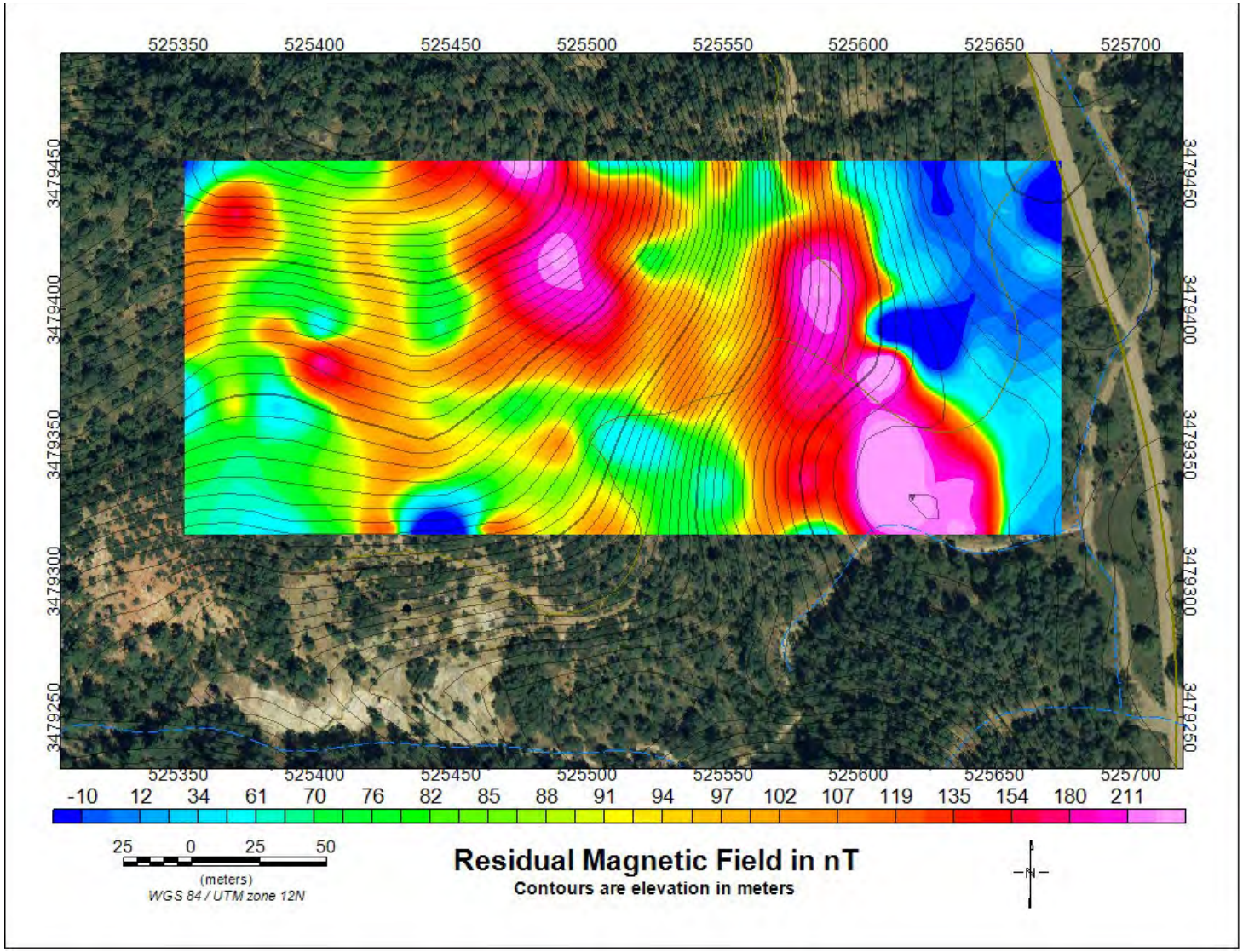

Figure 6.3. Residual magnetic field (nT) interpolated across entire Blue Nose Mine field site. Residual is calculated as the interpolated base station data subtracted from the observed total field.

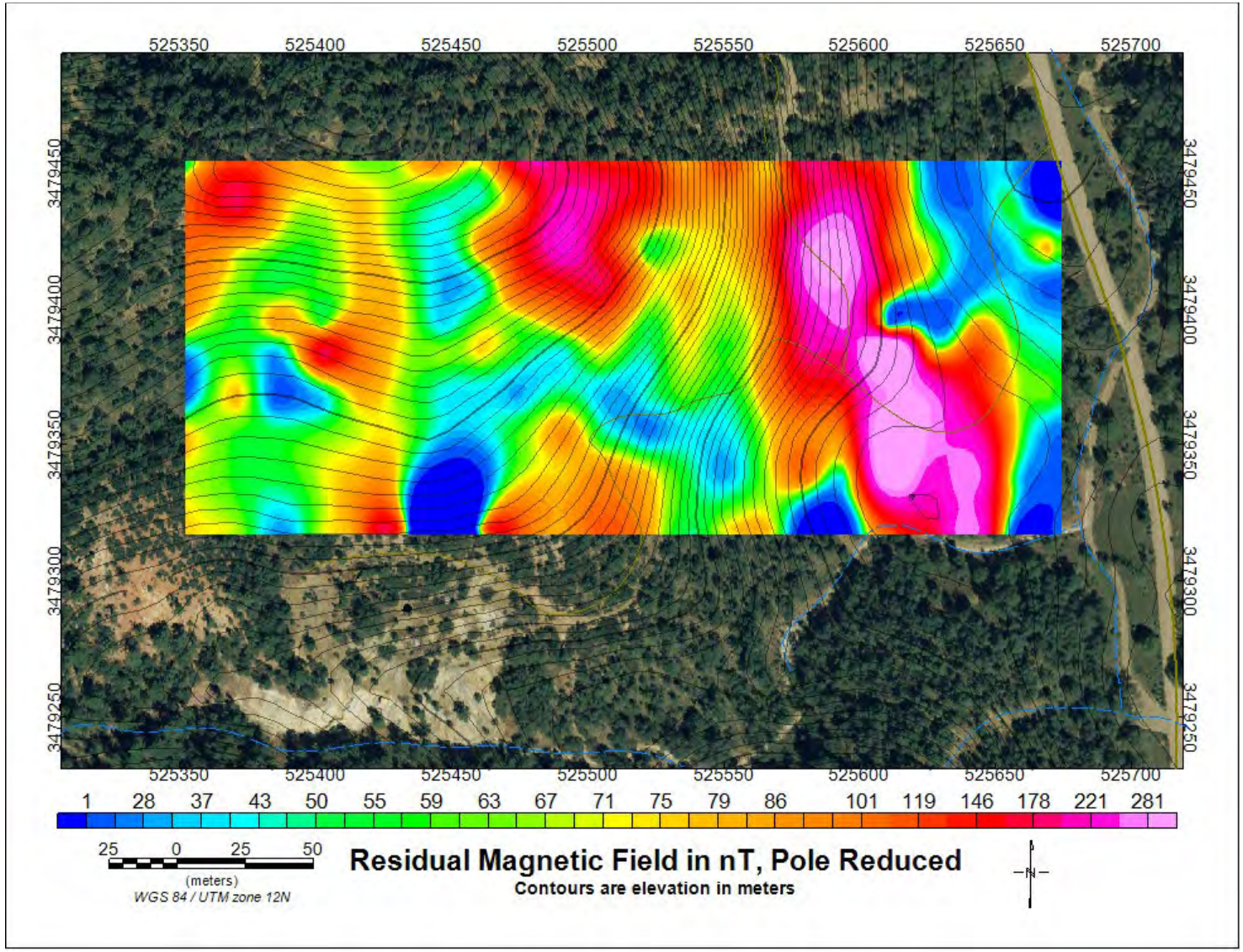

Figure 6.4. Same data as Figure 6.3 with a pole reduction correction. The magnetic inclination and declination used for this correction are 58º and +9.5º, respectively.

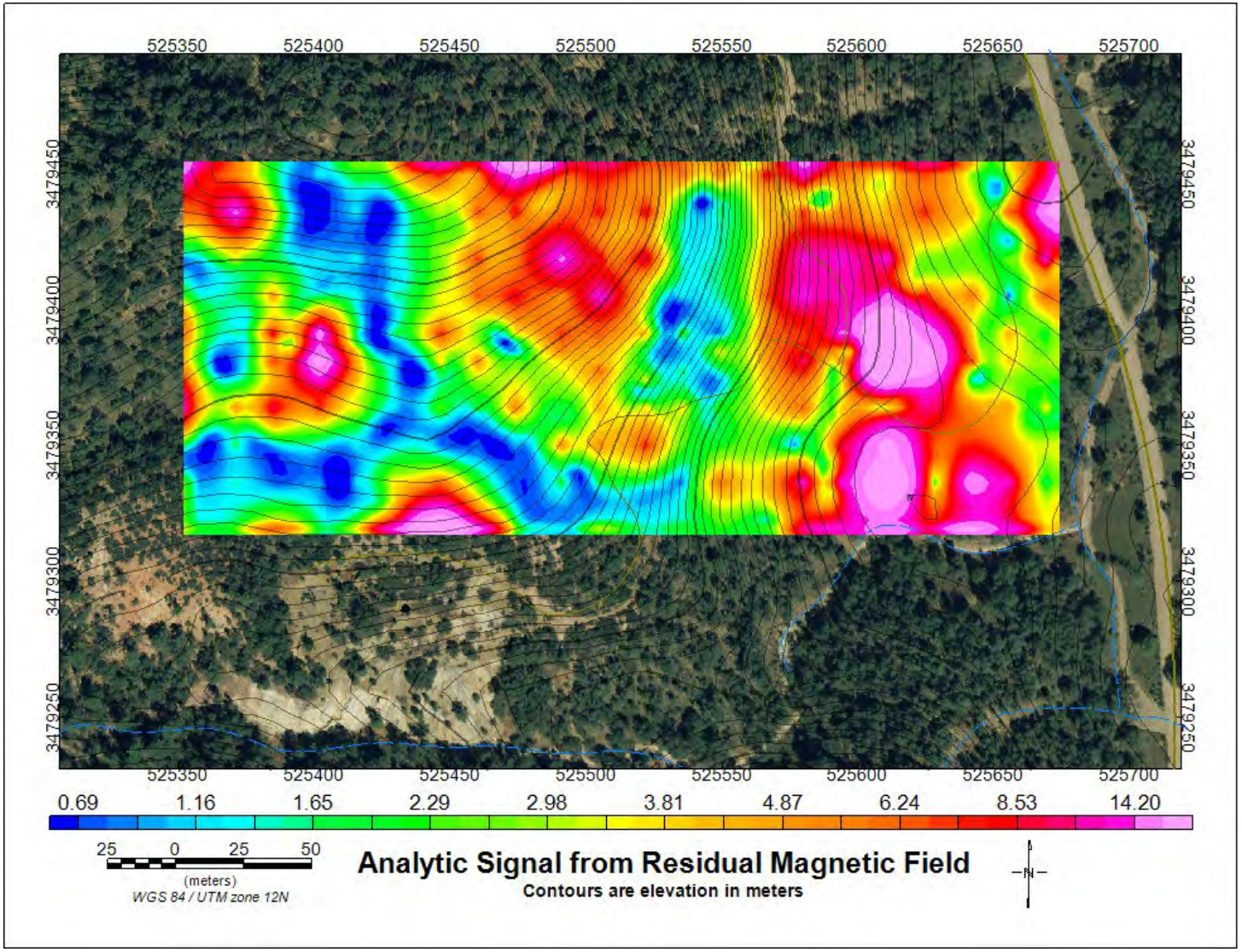

Figure 6.5. Analytic signal correction applied to data plotted in Figure 6.3. The lack of singularities in this corrected data implies that there were no large metal objects in the field site that could have obscured the analysis.

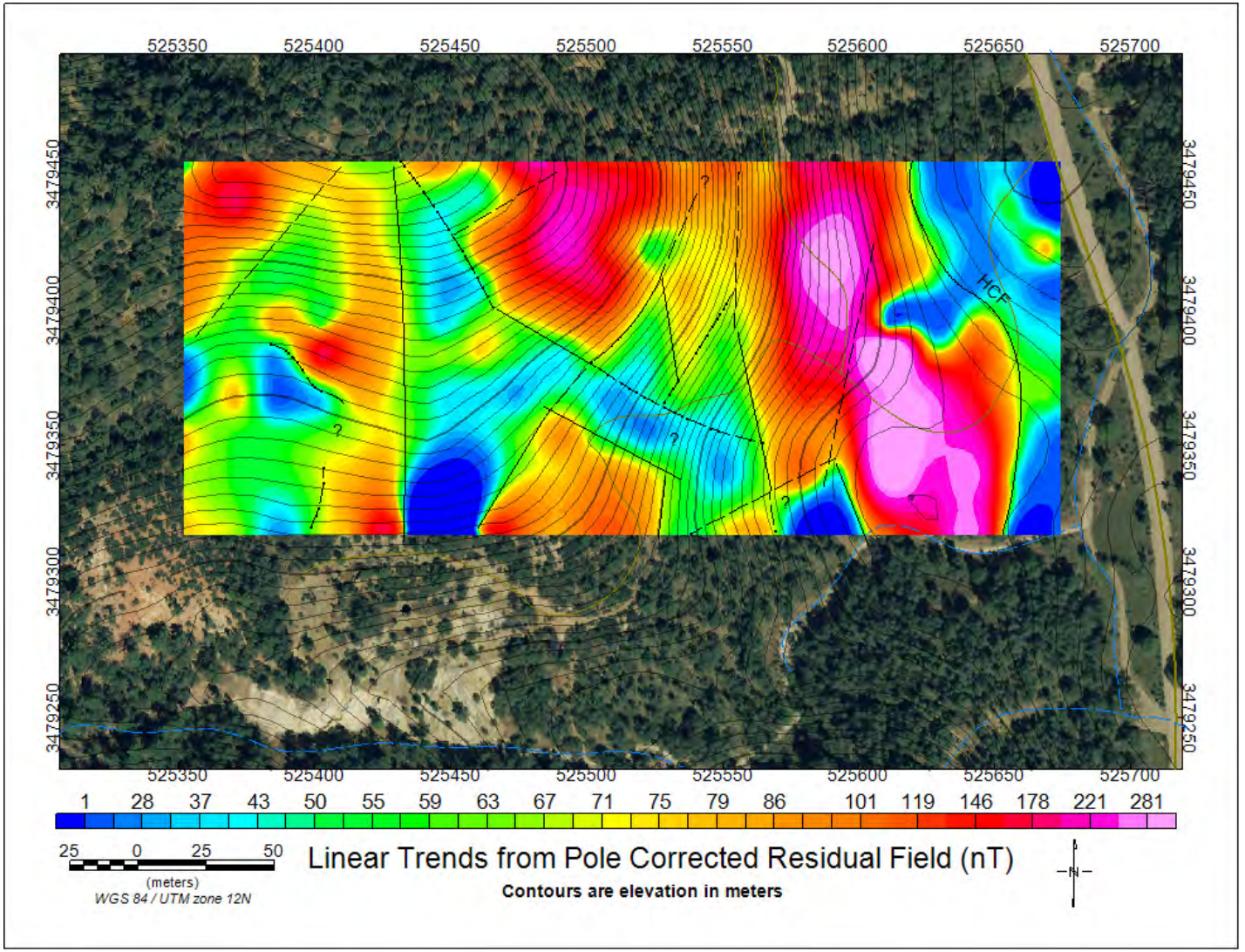

Figure 6.6. Same data as plotted in Figure 6.4 with interpreted linear features overlain. The line labeled 'HCF' in the east side of the field area is the interpreted position of the Harshaw Creek Fault. Other linear features are likely sympathetic faults or ancient faults.

Station	Total Field (nT)	Time (UTC-7)	Easting	Northing
1S-1	45,966	10:09	525670	3479380
1S-2	46,002	10:10	525655	3479380
1S-3	45,969	10:11	525640	3479380
1S-4	45,991	10:13	525625	3479380
1S-5	46,045	10:15	525610	3479380
1S-6	46,232	10:16	525595	3479380
1S-7	46,172	10:18	525580	3479380
1S-8	46,083	10:21	525565	3479380
1S-9	46,061	10:22	525550	3479385
1S-10	46,080	10:24	525535	3479378
1S-11	46,061	10:25	525520	3479375
1S-12	46,100	10:27	525506	3479378
1S-13	46,087	10:29	525490	3479383
1S-14	46,086	10:30	525475	3479381
1S-15	46,092	10:33	525460	3479380
1S-16	46,076	10:35	525445	3479380
1S-17	46,066	10:36	525430	3479380
1S-18	46,075	10:38	525416	3479384
1S-19	46,168	10:40	525401	3479380
1S-20	46,044	10:42	525385	3479380
1S-21	46,055	10:44	525370	3479381
1S-22	46,057	10:46	525355	3479381

Table 6.1. Station location and total field data for Line 1S. Data collected on February 16, 2019.

Station	Total Field (nT)	Time (UTC-7)	Easting	Northing
2S-1	46017	11:39	525670	3479365
2S-2	45992	11:37	525655	3479365
2S-3	46028	11:35	525640	3479365
2S-4	46107	11:34	525625	3479365
2S-5	46160	11:32	525610	3479365
2S-6	46136	11:30	525595	3479365
2S-7	46141	11:27	525580	3479365
2S-8	46099	11:25	525565	3479365
2S-9	46061	11:21	525550	3479365
2S-10	46075	11:20	525535	3479365
2S-11	46064	11:15	525520	3479365
2S-12	46041	11:13	525505	3479365
2S-13	46049	11:11	525490	3479365
2S-14	46036	11:09	525475	3479365
2S-15	46053	11:07	525460	3479365
2S-16	46053	11:03	525445	3479365
2S-17	46066	11:01	525430	3479365
2S-18	46086	11:00	525415	3479365
2S-19	46044	10:57	525400	3479365
2S-20	46012	10:54	525385	3479365
2S-21	46068	10:52	525370	3479365
2S-22	46014	10:50	525355	3479365

Table 6.2. Station location and total field data for Line 2S. Data collected on February 16, 2019.

Station	Total Field (nT)	Time (UTC-7)	Easting	Northing
3S-1	45990	12:08	525670	3479350
3S-2	46014	12:10	525655	3479350
3S-3	46093	12:11	525640	3479350
3S-4	46159	12:13	525625	3479350
3S-5	46277	12:14	525610	3479350
3S-6	46123	12:16	525595	3479350
3S-7	46100	12:17	525580	3479350
3S-8	46080	12:20	525565	3479350
3S-9	46049	12:21	525550	3479350
3S-10	46037	12:25	525535	3479350
3S-11	46010	12:27	525520	3479350
3S-12	46024	12:30	525505	3479350
3S-13	46069	12:32	525490	3479350
3S-14	46056	12:34	525475	3479350
3S-15	46055	12:37	525461	3479350
3S-16	46059	12:40	525445	3479350
3S-17	46066	12:41	525430	3479350
3S-18	46056	12:43	525415	3479350
3S-19	46044	12:45	525400	3479350
3S-20	46036	12:47	525385	3479350
3S-21	46037	12:49	525370	3479350
3S-22	46040	12:51	525355	3479350

Table 6.3. Station location and total field data for Line 3S. Data collected on February 16, 2019.

Station	Total Field (nT)	Time (UTC-7)	Easting	Northing
4S-1	45990	13:46	525670	3479335
4S-2	46010	13:44	525655	3479335
4S-3	46196	13:42	525640	3479335
4S-4	46175	13:41	525625	3479335
4S-5	46355	13:39	525610	3479335
4S-6	46112	13:38	525595	3479335
4S-7	46141	13:36	525580	3479335
4S-8	46076	13:34	525565	3479335
4S-9	46026	13:32	525550	3479335
4S-10	46038	13:31	525535	3479335
4S-11	46046	13:29	525520	3479335
4S-12	46055	13:27	525505	3479335
4S-13	46048	13:26	525490	3479335
4S-14	46050	13:23	525475	3479335
4S-15	46038	13:20	525461	3479335
4S-16	46046	13:14	525445	3479335
4S-17	46065	13:11	525430	3479335
4S-18	46053	13:08	525415	3479335
4S-19	46049	13:07	525400	3479335
4S-20	46036	13:03	525385	3479335
4S-21	46029	13:01	525370	3479335
4S-22	46036	12:57	525355	3479335

Table 6.4. Station location and total field data for Line 4S. Data collected on February 16, 2019.

Station	Total Field (nT)	Time (UTC-7)	Easting	Northing
5S-1	45981	13:47	525670	3479320
5S-2	46007	13:48	525655	3479320
5S-3	46188	13:49	525640	3479320
5S-4	46182	13:51	525625	3479320
5S-5	46194	13:52	525610	3479320
5S-6	46060	13:53	525595	3479320
5S-7	46033	13:55	525580	3479320
5S-8	46067	13:56	525565	3479320
5S-9	46048	13:57	525550	3479320
5S-10	46036	13:59	525535	3479320
5S-11	46051	14:01	525520	3479320
5S-12	46069	14:03	525505	3479320
5S-13	46055	14:05	525490	3479320
5S-14	46067	14:07	525475	3479320
5S-15	46053	14:11	525461	3479320
5S-16	45831	14:16	525445	3479320
5S-17	46058	14:20	525430	3479320
5S-18	46053	14:23	525415	3479320
5S-19	46036	14:26	525400	3479320
5S-20	46008	14:29	525385	3479320
5S-21	46022	14:31	525370	3479320

Table 6.5. Station location and total field data for Line 5S. Data collected on February 16, 2019.

Station	Total Field (nT)	Time (UTC-7)	Easting	Northing
1N-1	45937	9:50	525670	3479450
1N-2	45988	9:51	525655	3479450
1N-3	45978	9:52	525640	3479450
1N-4	45956	9:55	525625	3479450
1N-5	46002	9:56	525610	3479450
1N-6	46027	9:58	525595	3479450
1N-7	46113	9:59	525580	3479450
1N-8	46026	10:01	525565	3479450
1N-9	46073	10:02	525550	3479450
1N-10	46028	10:04	525535	3479450
1N-11	46057	10:06	525520	3479450
1N-12	46052	10:07	525505	3479450
1N-13	46128	10:09	525490	3479450
1N-14	46207	10:11	525475	3479450
1N-15	46118	10:13	525461	3479450
1N-16	46117	10:15	525445	3479450
1N-17	46071	10:16	525430	3479450
1N-18	46047	10:18	525415	3479450
1N-19	46054	10:19	525400	3479450
1N-20	46048	10:21	525385	3479450
1N-21	46044	10:22	525370	3479450
1N-22	45985	10:24	525355	3479450

Table 6.6. Station location and total field data for Line 1N. Data collected on February 17, 2019.

Station	Total Field (nT)	Time (UTC-7)	Easting	Northing
0-1	45861	11:11	525670	3479435
0-2	45988	11:10	525655	3479435
0-3	45960	11:07	525640	3479435
0-4	45956	11:06	525625	3479435
0-5	46022	11:03	525610	3479435
0-6	46078	11:00	525595	3479435
0-7	46054	10:59	525580	3479435
0-8	46039	10:57	525565	3479435
0-9	46048	10:54	525550	3479435
0-10	46063	10:52	525535	3479435
0-11	46108	10:51	525520	3479435
0-12	46132	10:49	525505	3479435
0-13	46152	10:48	525490	3479435
0-14	46089	10:46	525475	3479435
0-15	46052	10:45	525461	3479435
0-16	46053	10:44	525445	3479435
0-17	46057	10:42	525430	3479435
0-18	46059	10:40	525415	3479435
0-19	46051	10:38	525400	3479435
0-20	46054	10:36	525385	3479435
0-21	46129	10:34	525370	3479435
0-22	46049	10:32	525355	3479435

Table 6.7. Station location and total field data for Line 0. Data collected on February 17, 2019.

Station	Total Field (nT)	Time (UTC-7)	Easting	Northing
E420-1	46010	11:27	525670	3479420
E420-2	45976	11:29	525655	3479420
E420-3	45967	11:32	525640	3479420
E420-4	45990	11:34	525625	3479420
E420-5	46001	11:36	525610	3479420
E420-6	46148	11:37	525595	3479420
E420-7	46162	11:38	525580	3479420
E420-8	46075	11:40	525565	3479420
E420-9	46050	11:41	525550	3479420
E420-10	46051	11:43	525535	3479420
E420-11	46037	11:44	525520	3479420
E420-12	46098	11:45	525505	3479420
E420-13	46211	11:47	525490	3479420
E420-14	46144	11:48	525475	3479420
E420-15	46111	11:50	525461	3479420
E420-16	46050	11:52	525445	3479422
E420-17	46052	11:52	525430	3479420
E420-18	46062	11:55	525415	3479420
E420-19	46049	11:57	525400	3479420
E420-20	46057	11:58	525385	3479420
E420-21	46067	12:02	525370	3479420
E420-22	46071	12:03	525355	3479420

Table 6.8. Station location and total field data for Line 420E. Data collected on February 17, 2019.

Station	Total Field (nT)	Time (UTC-7)	Easting	Northing
E405-1	45955	12:45	525670	3479405
E405-2	45968	12:44	525655	3479405
E405-3	45950	12:42	525640	3479405
E405-4	45996	12:41	525625	3479405
E405-5	46069	12:40	525610	3479405
E405-6	46164	12:32	525595	3479405
E405-7	46191	12:30	525580	3479405
E405-8	46076	12:30	525565	3479405
E405-9	46054	12:26	525550	3479405
E405-10	46062	12:25	525535	3479405
E405-11	46072	12:23	525520	3479405
E405-12	46168	12:22	525505	3479405
E405-13	46166	12:20	525490	3479405
E405-14	46147	12:19	525475	3479405
E405-15	46066	12:17	525461	3479405
E405-16	46040	12:15	525445	3479405
E405-17	46060	12:14	525430	3479405
E405-18	46059	12:13	525415	3479405
E405-19	46045	12:11	525400	3479405
E405-20	46033	12:09	525385	3479405
E405-21	46052	12:06	525370	3479405
E405-22	46074	12:04	525355	3479405

Table 6.9. Station location and total field data for Line 405E. Data collected on February 17, 2019.

Station	Total Field (nT)	Time (UTC-7)	Easting	Northing
E390-1	45972	12:50	525670	3479390
E390-2	45962	12:51	525655	3479390
E390-3	45969	12:53	525640	3479390
E390-4	45886	12:54	525625	3479390
E390-5	45833	12:56	525610	3479390
E390-6	46156	12:59	525595	3479390
E390-7	46158	13:00	525580	3479390
E390-8	46069	13:05	525565	3479390
E390-9	46054	13:06	525550	3479390
E390-10	46067	13:07	525535	3479390
E390-11	46058	13:09	525520	3479390
E390-12	46118	13:10	525505	3479390
E390-13	46120	13:12	525490	3479390
E390-14	46083	13:13	525475	3479390
E390-15	N/A	N/A	525461	3479390
E390-16	46030	13:16	525445	3479390
E390-17	46059	13:18	525430	3479390
E390-18	46056	13:20	525415	3479390
E390-19	46010	13:21	525400	3479390
E390-20	46076	13:24	525385	3479390
E390-21	46044	13:26	525370	3479390
E390-22	46073	13:28	525355	3479390

Table 6.10. Station location and total field data for Line 390E. Data collected on February 17, 2019. Total field data was not collected at station 390E-15 due to the presence of a nearby truck that biased results.

Time (UTC-7)	Field (nT)	Time (UTC-7)	Field (nT)
1010	45972	1315	45964
1015	45972	1320	45963
1020	45970	1325	45963
1025	45972	1330	45965
1030	45969	1335	45965
1035	45970	1340	45964
1040	45971	1345	45963
1045	45972	1350	45964
1050	45972	1400	45958
1055	45972	1405	45955
1100	45970	1410	45949
1105	45967	1415	45965
1110	45965	1420	45960
1115	45968	1425	45961
1120	45967	1430	45960
1125	45966	1435	45960
1130	45965	1445	45960
1135	45965	1450	45963
1205	45964	1455	45967
1210	45963	1500	45960
1215	45962	1505	45962
1220	45963	1510	45959
1225	45964	1515	45957
1230	45963	1520	45955
1235	45962	1525	45959
1240	45963	1530	45952
1245	45965	1535	45954
1250	45966	1540	45957

1255	45965	1545	45961
1300	45963	1550	45963
1305	45964	1555	45961
1310	45964	1600	45960

Table 6.11. Base station total field data collected on February 16, 2019.

Time (UTC-7)	Field (nT)	Time (UTC-7)	Field (nT)
945	45967	1225	45963
950	45964	1230	45964
955	45968	1235	45963
1000	45967	1240	45963
1005	45969	1245	45962
1010	45973	1250	45961
1015	45968	1255	45962
1020	45971	1300	45961
1025	45971	1305	45958
1030	45966	1310	45958
1035	45963	1315	45964
1040	45964	1320	45959
1045	45958	1325	45960
1050	45966	1330	45960
1055	45967	1335	45954
1100	45962	1340	45951
1105	45966	1345	45953

1110	45963	1350	45955
1115	45963	1355	45959
1120	45961	1400	45954
1125	45962	1405	45957
1130	45965	1410	45957
1135	45966	1415	48956
1140	45965	1420	45948
1145	45966	1425	45949
1150	45966	1430	45949
1155	45965	1445	45957
1200	45968	1450	45957
1205	45965	1455	45963
1210	45964	1500	45959
1215	45966	1505	45965
1220	45965		

Table 6.12. Base station total field data collected on February 17, 2019.

6.5 References

Ansari, A.H. and K. Alamdar, 2009, Reduction to the pole of magnetic anomalies using analytic signal, World Applied Sciences Journal, **7**, 405-409.

Bultman, M.W., 2015, Detailed interpretation of aeromagnetic data from the Patagonia Mountains area, southeastern Arizona: U.S. Geological Survey Scientific Investigations Report 2015-5029.

Chon, E., et al., 2016, Geophysical surveys near old Yuma Mine, Tucson Mountains, Arizona: geophysics field camp 2016, Laboratory for Advanced Subsurface Imaging, LASI-16-1.

Ervin, C.P, 1976, Reduction to the magnetic pole using a fast Fourier series algorithm, Computers and Geosciences, **2**, no. 2, 211-217.

Kis, K.I., 1990, Transfer properties of the reduction of magnetic anomalies to the pole and to the equator, Geophysics, **55**, no. 9, 1141-1147.

Likkason, O.K., 2014, Exploring the use of magnetic methods, Advanced Geosciences Remote Sensing, InTech.

Lyatsky, H., 2010, Magnetic and gravity methods in mineral exploration: the value of well-rounded geophysical skills, Lyatsky Geoscienes Research & Consulting Ltd., **35**, no. 08, 30-35.

Telford, W., L. Geldart, and R. Sheriff, 1990, Magnetic methods, Applied Geophysics, Cambridge: Cambridge University Press, 62-135.

7. Petrophysical Laboratory Analysis

7.1 Introduction and Methods

Core samples representing several lithologies were collected at the Blue Nose Mine site in order to facilitate comparison with other surveys. In many cases, small-scale resistivity measurements conducted in a laboratory setting may often be much higher than large-scale measurements taken in the field. This is due to a variety of circumstances, ranging from weathering of the rocks to bedding/soil saturation. Typically, special preparation and strict handling procedures are required for laboratory analysis to reflect field survey data accurately. However, when samples are harvested without these particular considerations, the results may still be used to improve survey data interpretation as well as to correlate geologic information in a particular region (Zonge International, 2019).

As stated previously, small-volume rock samples measured in a laboratory tend to inadequately represent large volume subsurface structures that are often faulted, jointed, or contain mineralized solutions. This is particularly true when measuring the resistivity and conductivity of a medium. However, fresh cores that haven't been exposed to air or elevated temperatures may yield resistivity values representative of the host rock (Zonge International, 2019). Conversely, induced polarization (IP) responses measured in the laboratory usually correlate well with field observations and thus provide a greater degree of accuracy for interpretation and/or targeting (Zonge et al., 2005).

7.2 Instrumentation and Field Procedures

All resistivity and induced polarization measurements were conducted utilizing a GDP32 III, LDT-10B lab downhole transmitter, and a four-electrode porous sample holder filled with aqueous copper sulfate. During the TDIP (Time Domain IP) and CR (Complex Resistivity) testing, the sample is situated inside a plastic container in order to minimize sample exposure and moisture loss. Sample mass was determined utilizing an electronic balance, and sample dimensions were measured with electronic calipers. Magnetic susceptibility measurements were obtained utilizing a Bartington MS2 at the 1.0 CGS setting, unless readings were less than 1.0 μCGS, where the 0.1 CGS setting would then be used.

Shale samples were collected on February 9, 2016, in the vicinity of UTM 12R 0525467E 3479339N from an exposed outcrop of massively bedded shale that was dipping at 56^{o} NW (Figure 7.2). This rock unit was subjected to previous mining operations throughout the immediate area, and the bedding was

highly jointed throughout. The igneous sample was found down slope of the outcrop and was not collected in the same immediate vicinity. All four samples were returned to the rock laboratory at Zonge, International, where they were cut and cored to fit the testing specifications. They were saturated in Tucson, Arizona tap water for subsequent testing three days later. No exposed portion of the samples was used during any testing procedures.

7.3 Data Processing

Induced polarization response and resistivity were measured in the time domain mode on the GDP receiver using an 8 second period (2 seconds on positive, 2 seconds off, 2 seconds on negative, 2 seconds off). The IP response is integrated over a window from 0.45 to 1.1 seconds during the off time (Zonge International, 2019). This was performed at a constant current via the LDT-10B transmitter that is set to 100 nA. IP measurements are made in the time domain for a complete cycle of 8 seconds (two transmitter pulses), averaged over 16 cycles and 4 stacks (Zonge International, 2019).

The CR results are the stacked and averaged values for 0.125, 1.0, and 8.0 Hz, including the 3rd, 5th, 7th, and 9th harmonics for each fundamental frequency (Zonge International, 2019). During these complex resistivity measurements, three stacks per frequency range were used rather than four stacks. Complex plane plots and magnitude/phase plots are presented along with tabulations of the spectral results and apparent resistivity and phase at 0.125 Hz. The spectral-type parameters are based on the slopes of the CR curves for the 0.125 to 1 Hz, 1 to 8 Hz, and 8 to 72 Hz data (Zonge International, 2019).

7.4 Interpretation and Conclusions

In this study, laboratory analysis of hand samples collected at the Blue Nose Mine facilitated potential refinement of our interpretation of the subsurface survey. It's plausible that a bedding plane of the same or similar composition to the high resistivity shale unit measured in the lab is located within the eastern resistive target (Figure 3.4) identified in our TEM survey. Additionally, the granitic sample had a measured resistivity of approximately 95 Ohm-m, which may also correlate with the less resistive feature beneath the first TEM station (Figure 3.4) or the target between/beneath the resistive targets. Although these small-scale sample resistivities seem to provide potential aid in identifying, differentiating, and

correlating particular subsurface features; without samples from these areas we are unable to rely on this interpretation with any degree of certainty.

The primary limitation of petrophysical laboratory analysis for this EM survey was the lack of an adequate and diverse sample size. In order to be more effective at aiding our interpretation, several subsurface samples would be required along the survey line from a depth that exceeded our own depth of investigation. Although it may be possible to sample an exposure nearby that geologically correlates to subsurface rock within the survey area, it would be unlikely that it would represent the region's specific geophysical properties.

	Time Domain IP		Complex Resistivity						
Sample ID	Apparent Resistivity (Ohm-m)	Chargeability (msec)	Apparent Resistivity (Ohm-m)	3-point IP (mrad)	Apparent Solid Specific Gravity	Dry Density (g/cm^3)	Saturated Density (g/cm^3)	Porosity	Magnetic Susceptibility (μCGS)
001 Granite/ Granodiorite	101	17.91	91	18.91	2.77	2.11	2.35	0.24	11.35
002 Shale (Upper Unit)	913	3.02	866	3.24	2.57	2.35	2.43	0.08	No Data
003 Shale (Lower Unit)	1095	4.12	1214	4.92	2.62	2.59	2.60	0.01	0.87
004 Highly Mineralized Shale (S, $CaCO_3$, SiO_2)	811	12.07	808	14.67	2.56	2.32	2.41	0.10	No Data

Table 7.1. Sample properties and results from the time domain IP, complex resistivity, density, porosity, and magnetic susceptibility laboratory test.

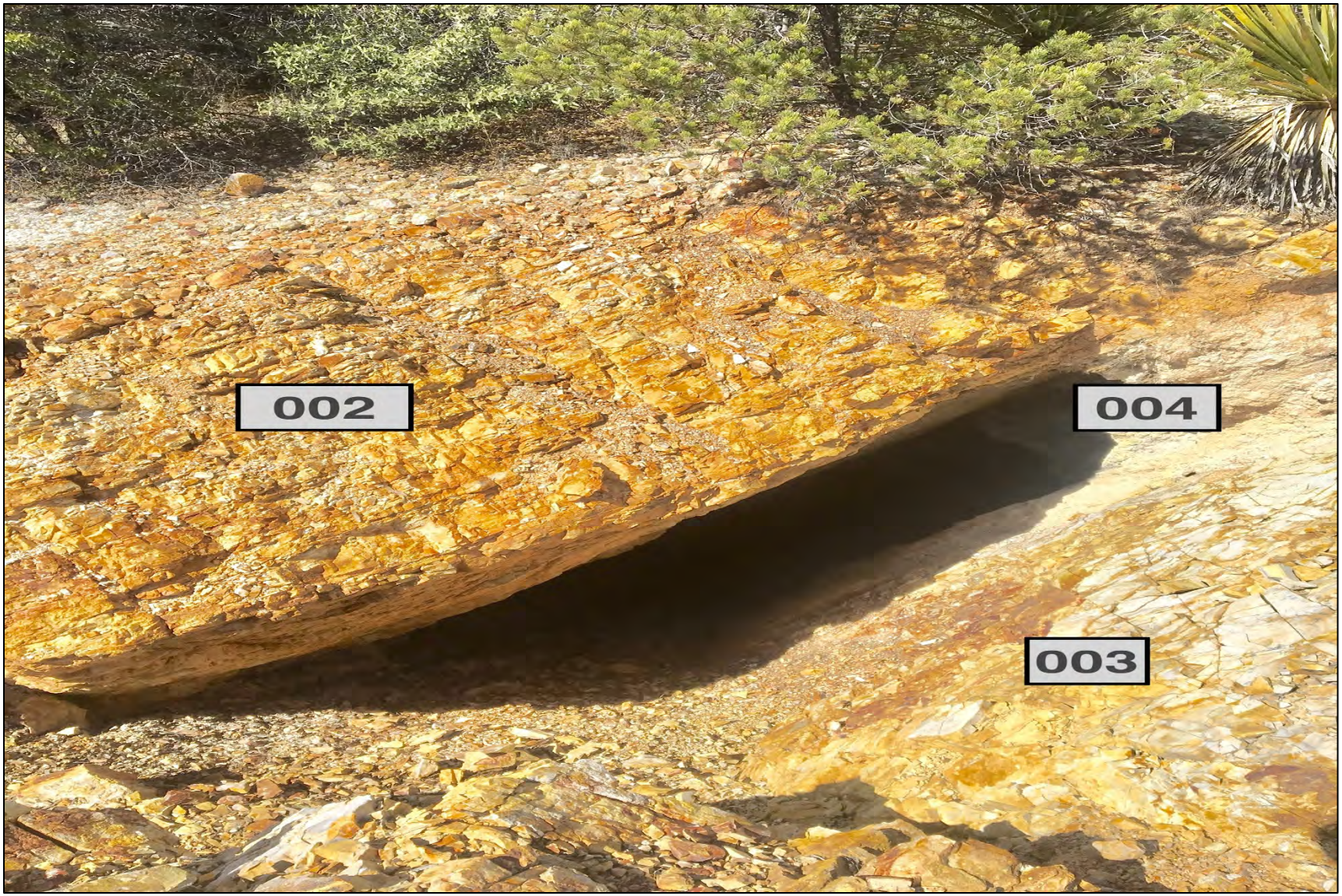

Figure 7.1. The hand sample extraction locations from the shale outcrop with sample identification numbers overlying their respective unit.

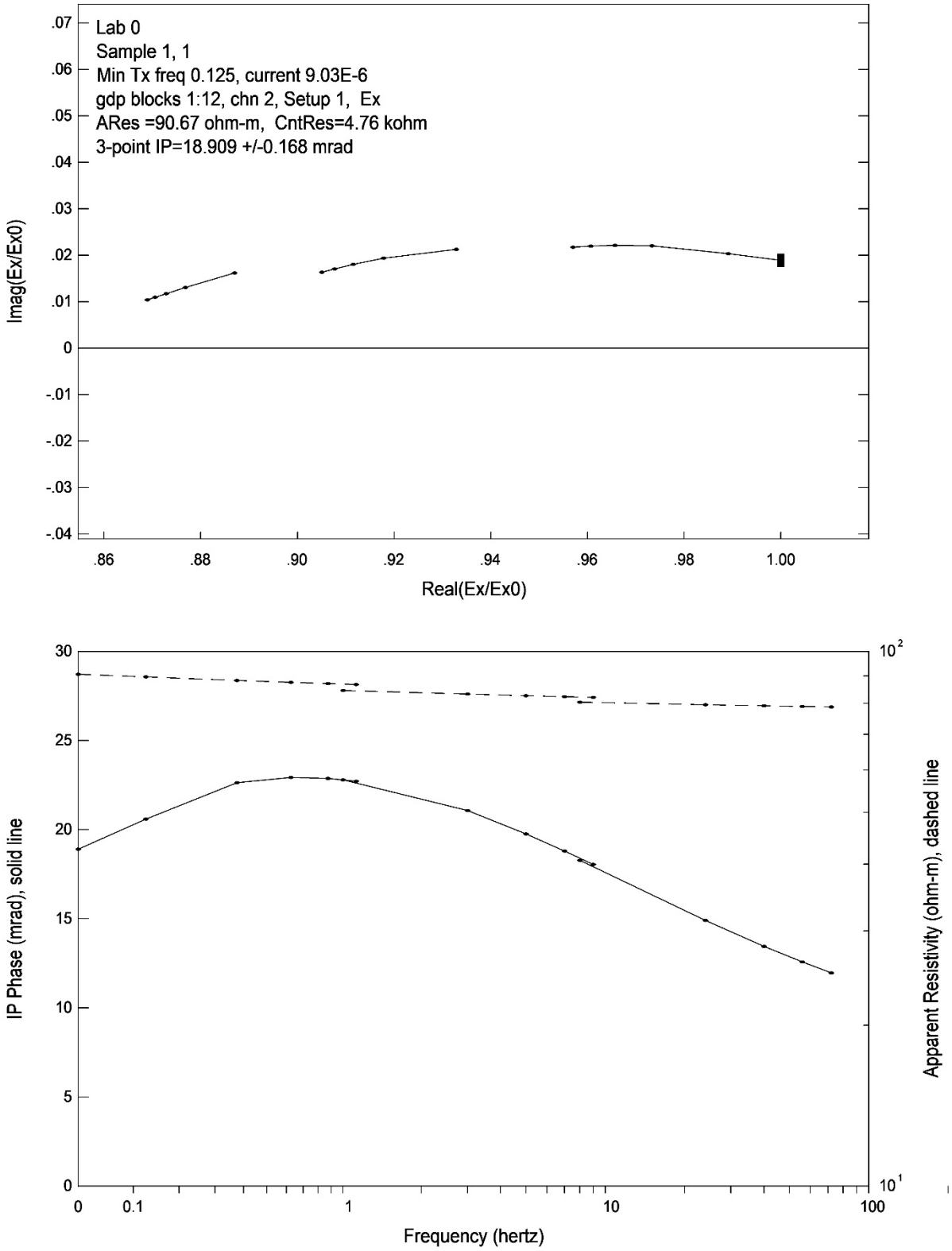

Figure 7.2. Complex resistivity plotted results for sample 001. (Top) Real vs. Imaginary. (Bottom) IP and apparent resistivity vs. frequency.

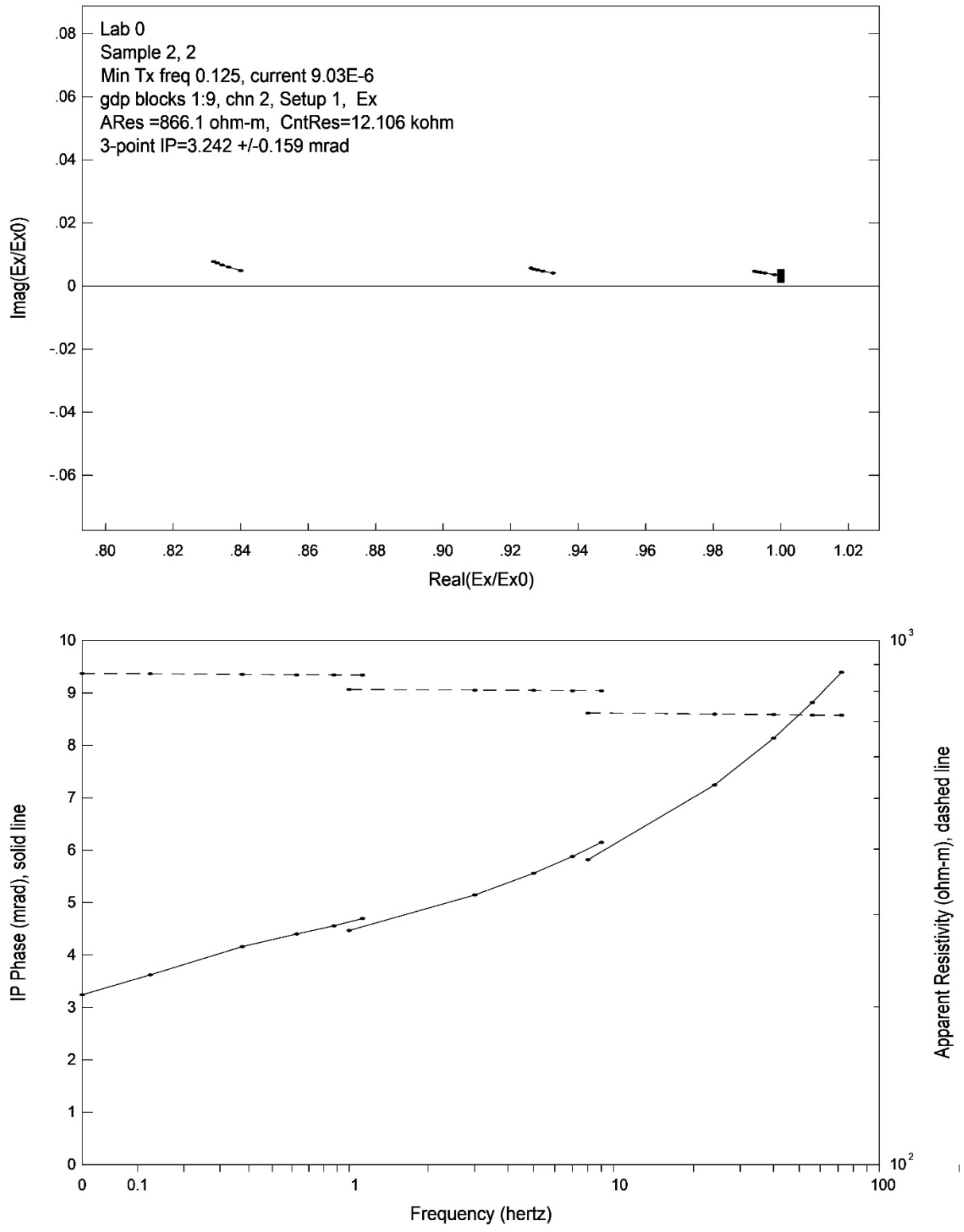

Figure 7.3. Complex resistivity plotted results for sample 002. (Top) Real vs. Imaginary (Bottom) IP and apparent resistivity vs. frequency.

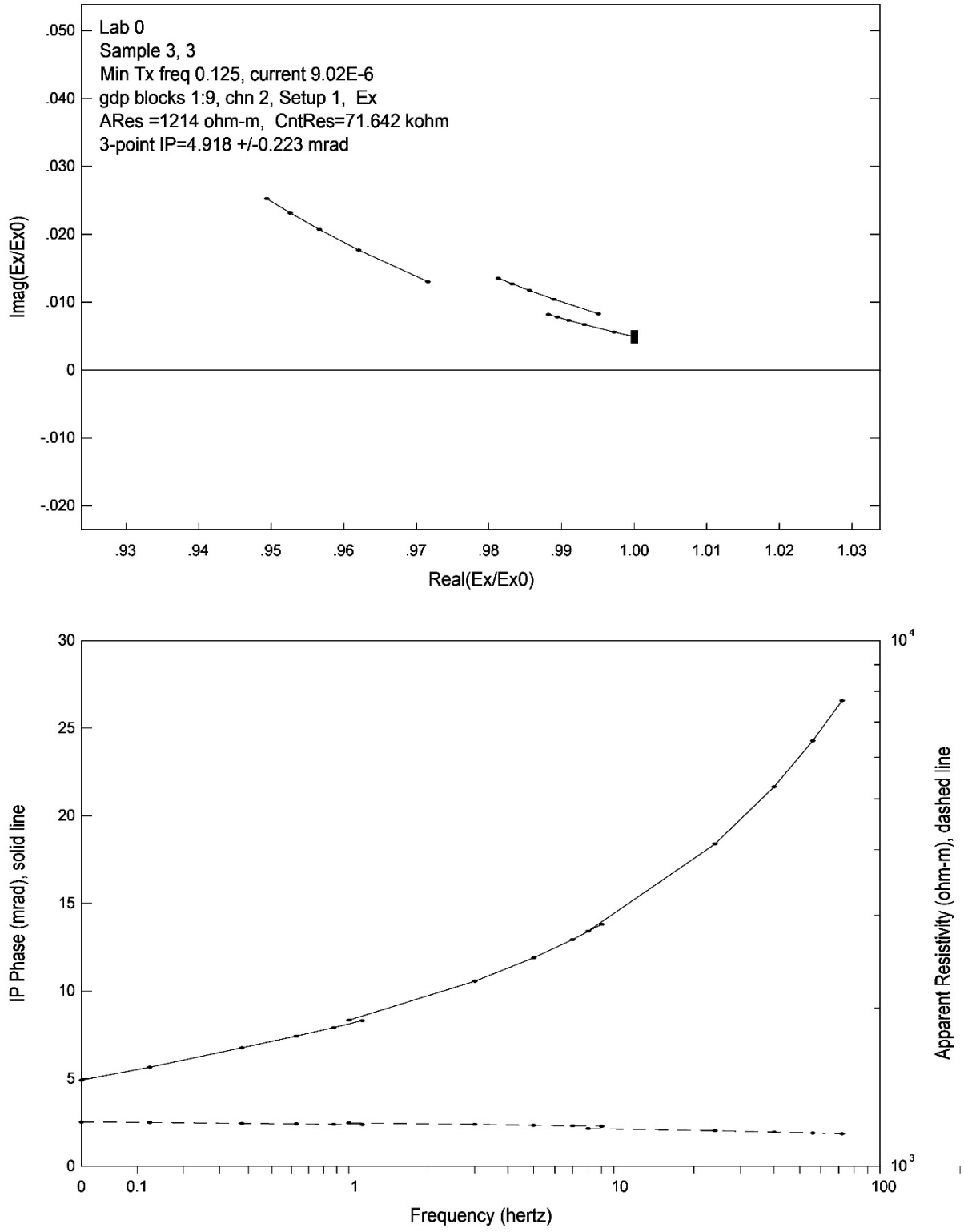

Figure 7.4. Complex resistivity plotted results for sample 003. (Top) Real vs. Imaginary (Bottom) IP and apparent resistivity vs. frequency.

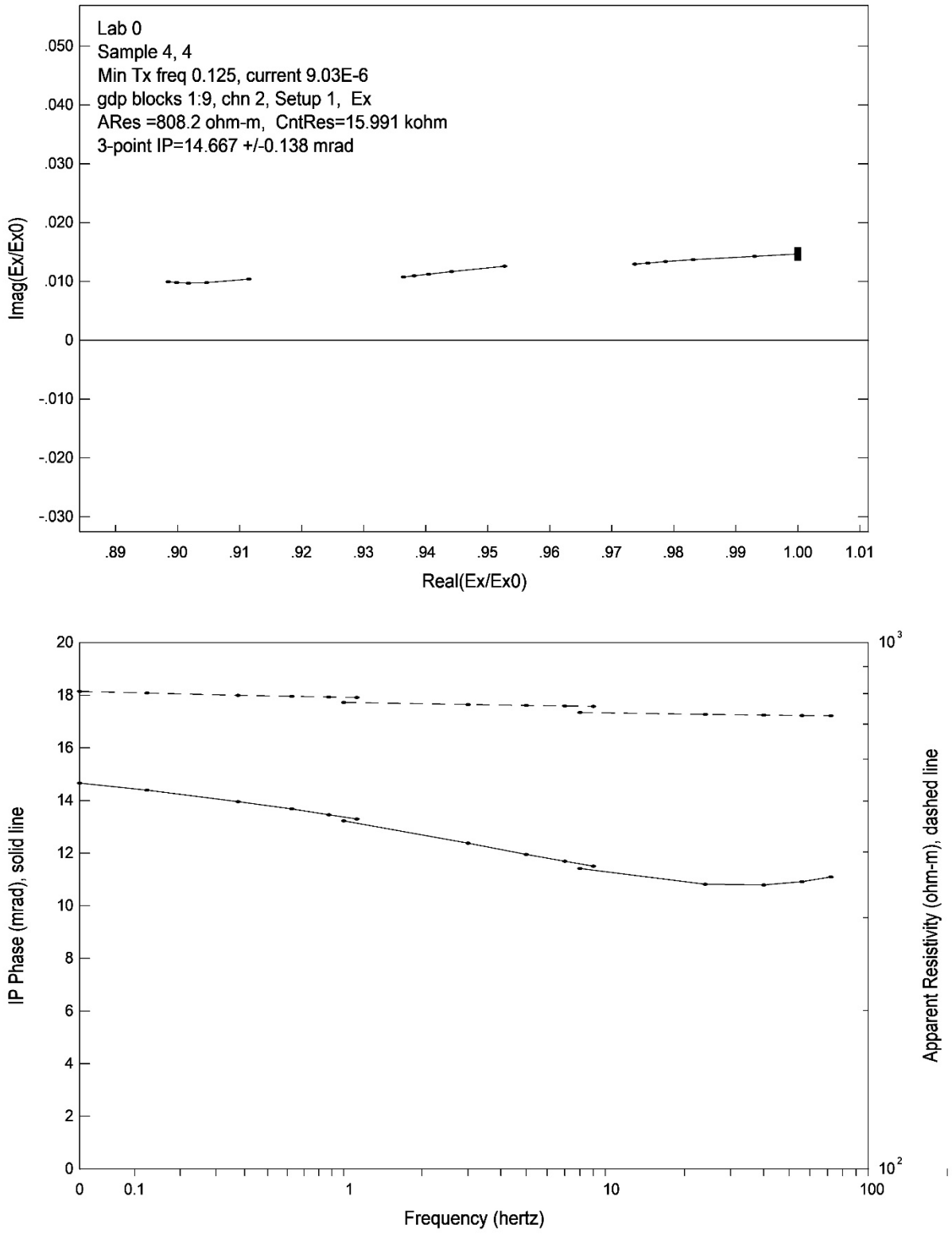

Figure 7.5. Complex resistivity plotted results for sample 004. (Top) Real vs. Imaginary (Bottom) IP and apparent resistivity vs. frequency.

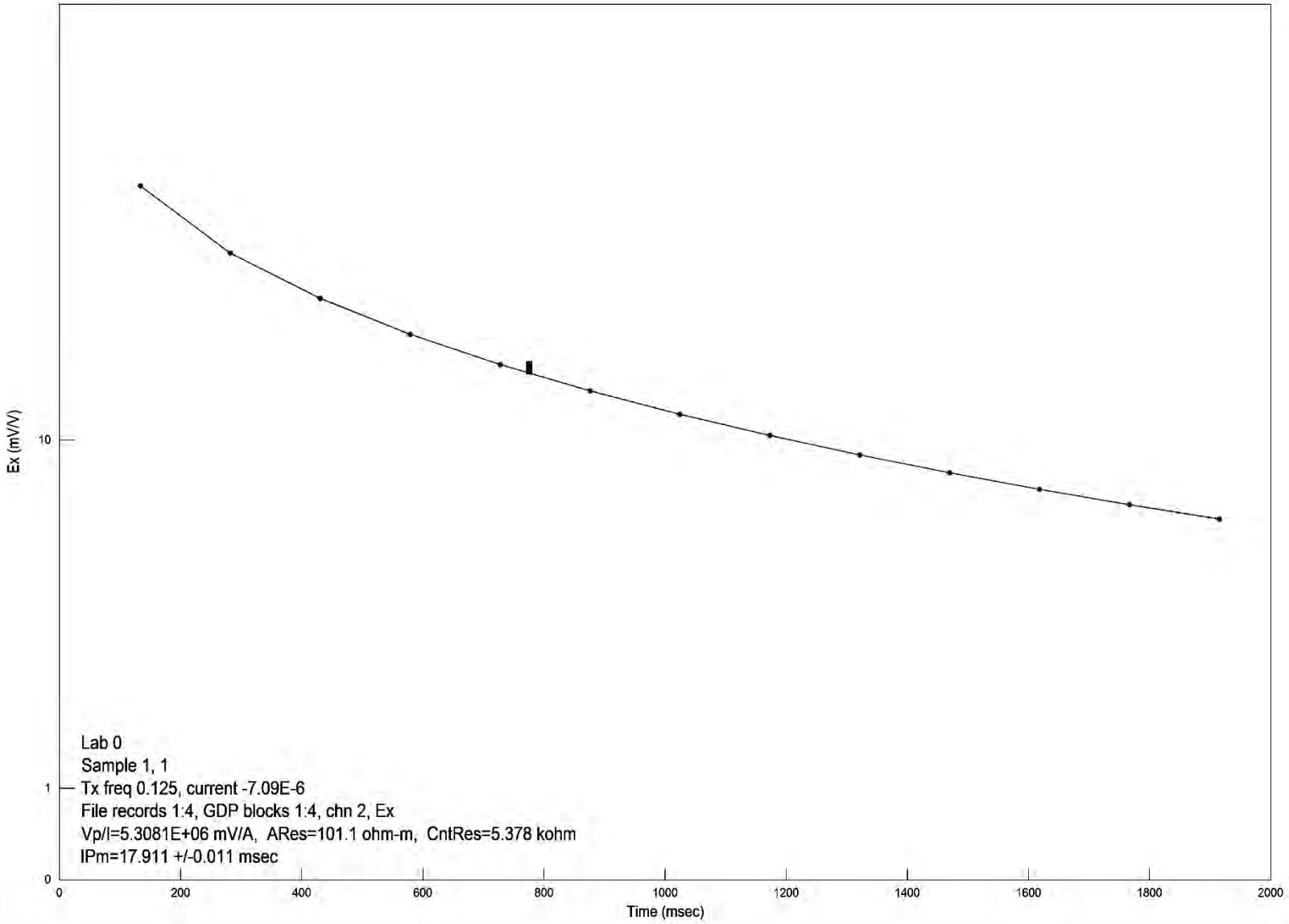

Figure 7.6. IP response from TDIP results for sample 001.

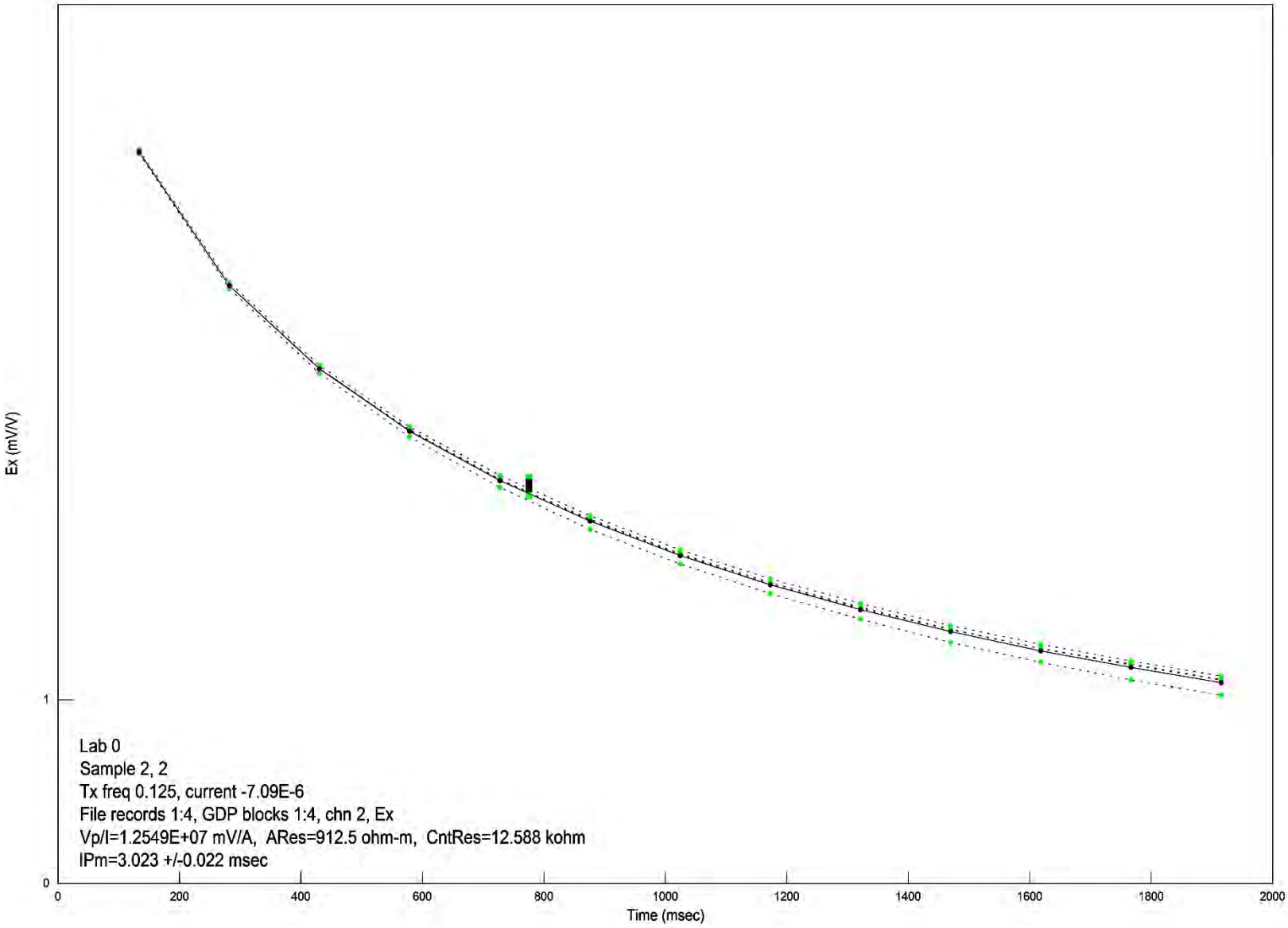

Figure 7.7. IP response from TDIP results for sample 002.

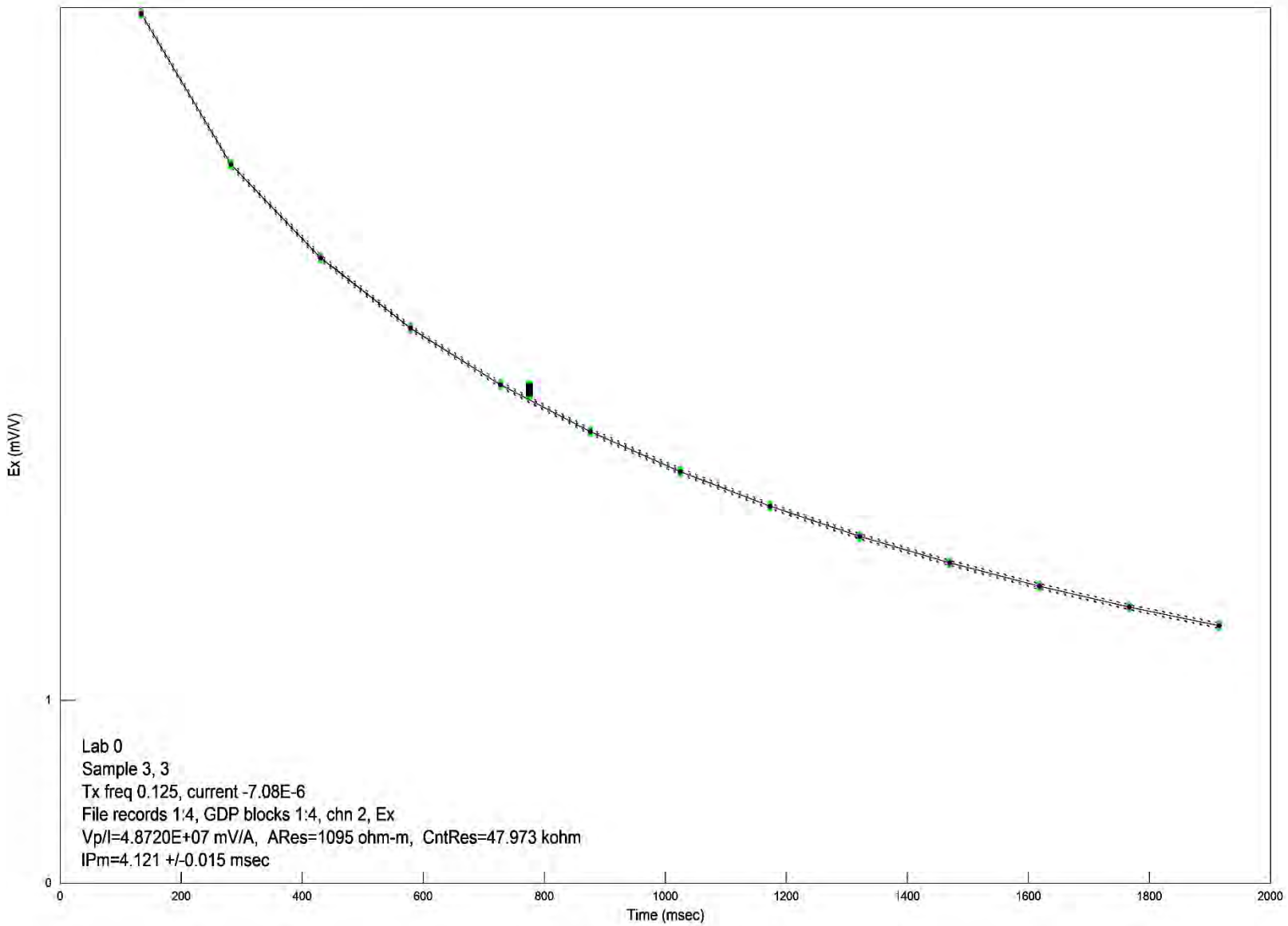

Figure 7.8. IP response from TDIP results for sample 003.

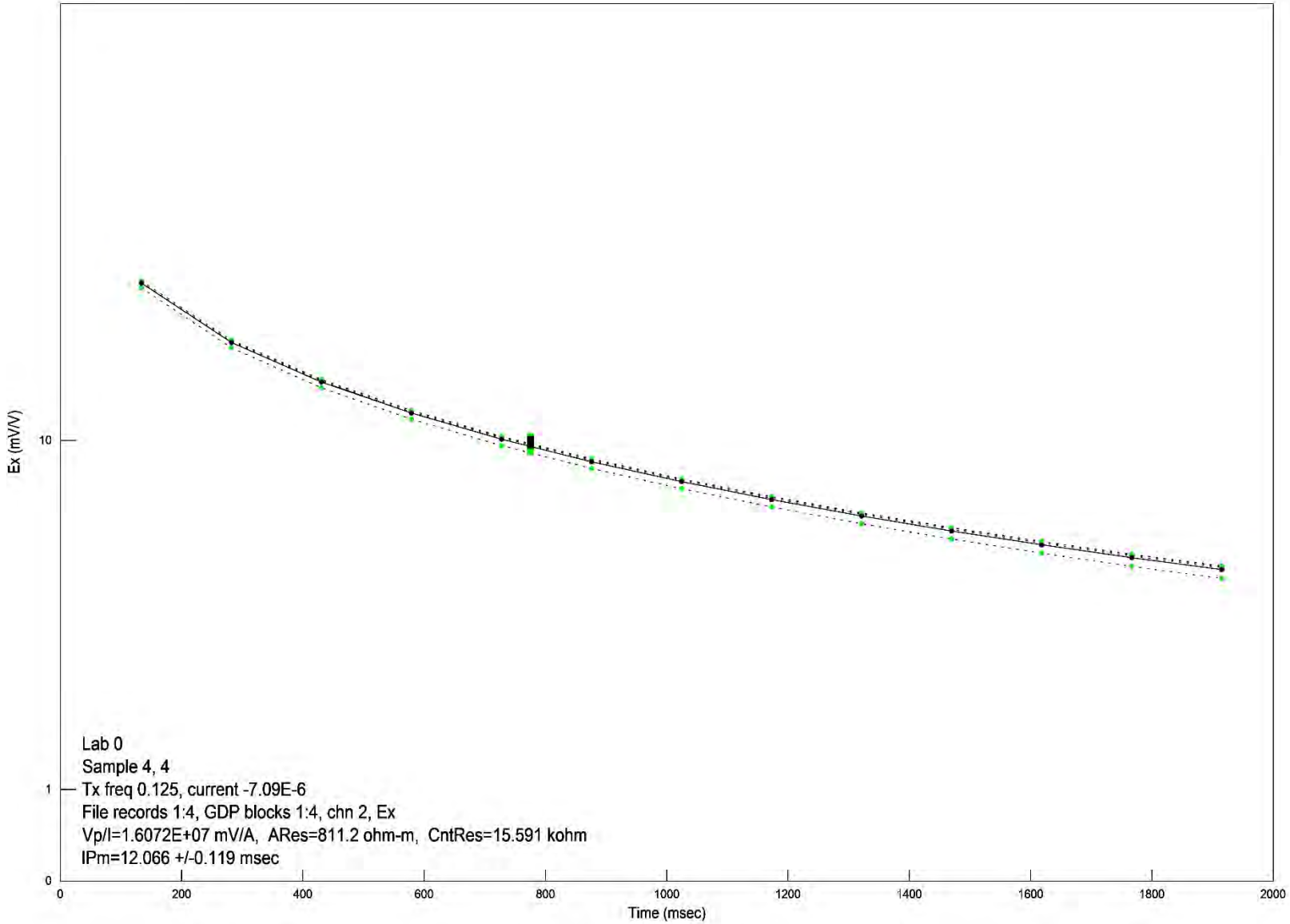

Figure 7.9. IP response from TDIP results for sample 004.

7.5 References

Zonge, K., J. Wynn, and S. Urquhart, 2005, Resistivity, induced polarization, and complex resistivity, Near Surface Geophysics, 261-296.

Zonge International, 2019, http://zonge.com/rock-properties-lab/lab-measurements/, accessed April 14, 2019.

8. Combined Analysis

8.1 Hydrology

Groundwater level analysis has to be performed through geophysical surveys as a result of the complex geology at the Blue Nose Mine. The interpreted Harshaw Creek Fault and any other such fault or fracture provide conduits for water transport into the regional subsurface storage system. In DC resistivity Line 1, a 250 – 500 Ohm-m amplitude anomaly is apparent 20 to 30 m from the eastern edge of the field site (Figure 8.2). A residual magnetic anomaly greater than 100 nT in amplitude appears at the same location (Figure 8.2). There exists a 250 Ohm-m amplitude anomaly on the 20 m TEM transect at 60 m from the eastern edge of the survey and 20 m below the surface (Figure 8.3). These anomalies are within close proximity of each other (Figure 8.1); however, without magnetic survey data for the eastern edge of the TEM transect, it is difficult to hypothesize the potential for groundwater in this fault system.

The interpreted groundwater anomaly is not only limited to DC Line 1 and the 20 m TEM loops, but is also apparent on DC resistivity Line 2 as an 800 – 2000 Ohm-m conductive unit on the eastern edge of the line (Figure 4.5). At transect distances -29 to 67 m and from 30 to 72 m below the surface, this unit is interpreted as surface water recharge into the subsurface. While collecting data in the field, the 50 m DC resistivity electrode was noted to have been placed in a stream feature. Water is hypothesized to follow Harshaw Creek from DC resistivity Line 2 to Line 1. Highly conductive units in Line 2, of amplitude around 10,000 Ohm-m, are hypothesized to be the result of hydrothermal mineralization.

Approximately 100 m downstream from the tailings piles, the stream feature emerges from shallow groundwater flow as a spring. This low flow is consistent from electrode spacing 50 to 40 m, where it recharges the groundwater. Suspended in the water, the contaminants flow in the stream feature until they infiltrate the subsurface, where a secondary hydrothermal mineralization feature occurs at 20 m below the surface (Figure 4.5). The more highly

conductive unit is interpreted to be caused by heavy metal contaminants which leached into the groundwater upstream near the tailings piles. Groundwater has a slightly laminar flow between DC resistivity Lines 1 and 2, where the top of the mineralization occurs at 15 m below the surface and at a distance of 28 m. Future hydrologic work in the area should include sampling pH, specific conductance, and metal concentrations. Sample well locations should be (1) up gradient from mining deposits and abandoned mine sites for use as background levels; (2) at livestock well 637238 in proximity to the Blue Nose Mine; (3) the deep adit located at Blue Nose Mine; and (4) in the Patagonia well field.

8.2 Tailings Material

By synthesizing all collected data, the dimensions of the tailings piles can be roughly determined. Based on field observations and 10 m TEM data, tailings start at the first loop and end at about the fifth loop, giving a total distance of 50 meters (Figures 3.3 and 3.5). The data shows that there is a highly conductive anomaly that extends to about 8 m depth. Similarly, according to EM-31/38, the tailings piles are 55 m in length and a depth of about 8 m. (Figure 5.13). Both models seem to agree on the depth to bedrock beneath the tailings piles; however, field observations give a depth up to 5 m. This suggests that the tailings piles are roughly 5 m deep with about 3 m of highly conductive and fractured bedrock beneath them. This 3 m of bedrock is likely contaminated by highly conductive metals that have been leached out of the tailings piles by water.

8.3 Geophysical Data Integration

Figure 8.2 shows the inverted resistivity depth section from DC Line 1 on the bottom and the interpolated magnetic field data correlated to the same transect above it. Figure 8.3 uses the same interpolation method but for the 20 m TEM station locations. The comparisons in these two figures allows for a more informed study of any significant correlations or discrepancies between the three datasets. Figure 8.1 displays magnetic survey data overlain by the station locations for the DC Lines 1 and 2 and the 20 m TEM array for spatial context when viewing these comparisons.

Trends from Figure 8.2 can be divided into three main sections, labeled Zones 1, 2, and 3. Zone 1 is characterized by a high-amplitude magnetic anomaly and moderately resistive values. The magnetic anomaly in Zone 1 shows a two-fold increase in amplitude when the pole correction is applied. This represents a somewhat more ordered distribution of magnetic dipole orientations, which results in a higher level of destructive interference due to the positive end of one dipole field being more aligned with the negative end of a neighboring dipole field. This order usually occurs when magma cools slowly enough such that magnetic minerals can align with the Earth's magnetic field. This is not the only way to form highly-ordered magnetism in minerals, but it is by far the most common. Resistivities in Zone 1 are mostly in the hundreds of Ohm-meters, with the notable exception of three small "pods" of more resistive material. These small features could be real, but could also be products of the inversion algorithm given their sizes and orientations. The geological environments which could produce these correlations are numerous, but some possibilities are more probable than others, given the geologic context of the field site. One of the most probable is that this zone is a late-phase intrusive dike rooted in a cupola of one of the larger granodioritic intrusions which drove mineralization in the area. The fact that this anomaly seems to correspond to the west side of the Harshaw Creek Fault also makes sense for a distal magmatic structure like a dike, because these structures commonly propagate along existing planes of structural weakness like bedding planes or faults.

Zone 2 is characterized by a very resistive subsurface beneath the topsoil and another high amplitude magnetic trend. This magnetic trend does not exhibit the same ordered behavior as the anomaly in Zone 1. It could represent magnetism resulting from a more distal alteration environment than the first zone. Incomplete melting and/or rapid mineral deposition can result in magnetic minerals that did not have a chance to fully align with an external field. In general, this produces anomalies which do not exhibit a large change in magnitude when subjected to pole correction. This may be due to hydrothermal mineralization related to the actual Blue Nose ore deposit. These base metal-replacement deposits are normally related to cooler and more distal mineralization which took place further from the main intrusive structures. This type of mineralization usually needs some type of structure to allow for metasomatic fluids to reach

lithologies with favorable chemistries for rapid deposition of base metal sulfides. For this reason, it is likely that there is an older, highly mineralized fault structure which separates Zones 2 and 3. This location correlates with the majority of the mine workings as evidenced from the surface; thus, it is very likely that this conductive area between Zones 2 and 3 hosts the actual deposit. The high resistivities in the center of Zone 2 may be less altered carbonate lithologies, which are further from the mineralized structure.

Lastly, the laboratory resistivity results should be compared to measured values of resistivity from other methods. When compared to the 20 m TEM survey data, the laboratory resistivity results (Table 7.1) of the exposed shale appear to correlate well with the large resistive anomaly that extends from the surface down to the limit of our depth of investigation. This resistive target is located between stations 11 and 12 of the TEM survey (Figure 3.2), which were separated by the sampled outcrop (Figure 7.1). This same feature is also observed in the inverted resistivity data from Line 2 of the DC resistivity survey (Figure 4.6). The granitic sample displayed a much lower resistivity of approximately 95 Ohm-m (Figure 7.6) compared to the shale samples and could be present in the survey area; however, the conductive target below TEM station 11 (Figure 3.4) appears significantly more conductive than 95 Ohm-m. Of the four samples collected at the site, none displayed a measured resistivity that correlated with the conductive target observed in the processed TEM data (Figure 3.4). Resultant values for the corrected magnetic susceptibility could only be measured from the granitic sample and the lower portion of the sampled outcrop. As a result, magnetic susceptibility variation throughout the bedding could not be measured. However, the low yet positive values measured from the two samples may indicate that these units are paramagnetic, resulting in strengthening of the magnetic field by these rocks.

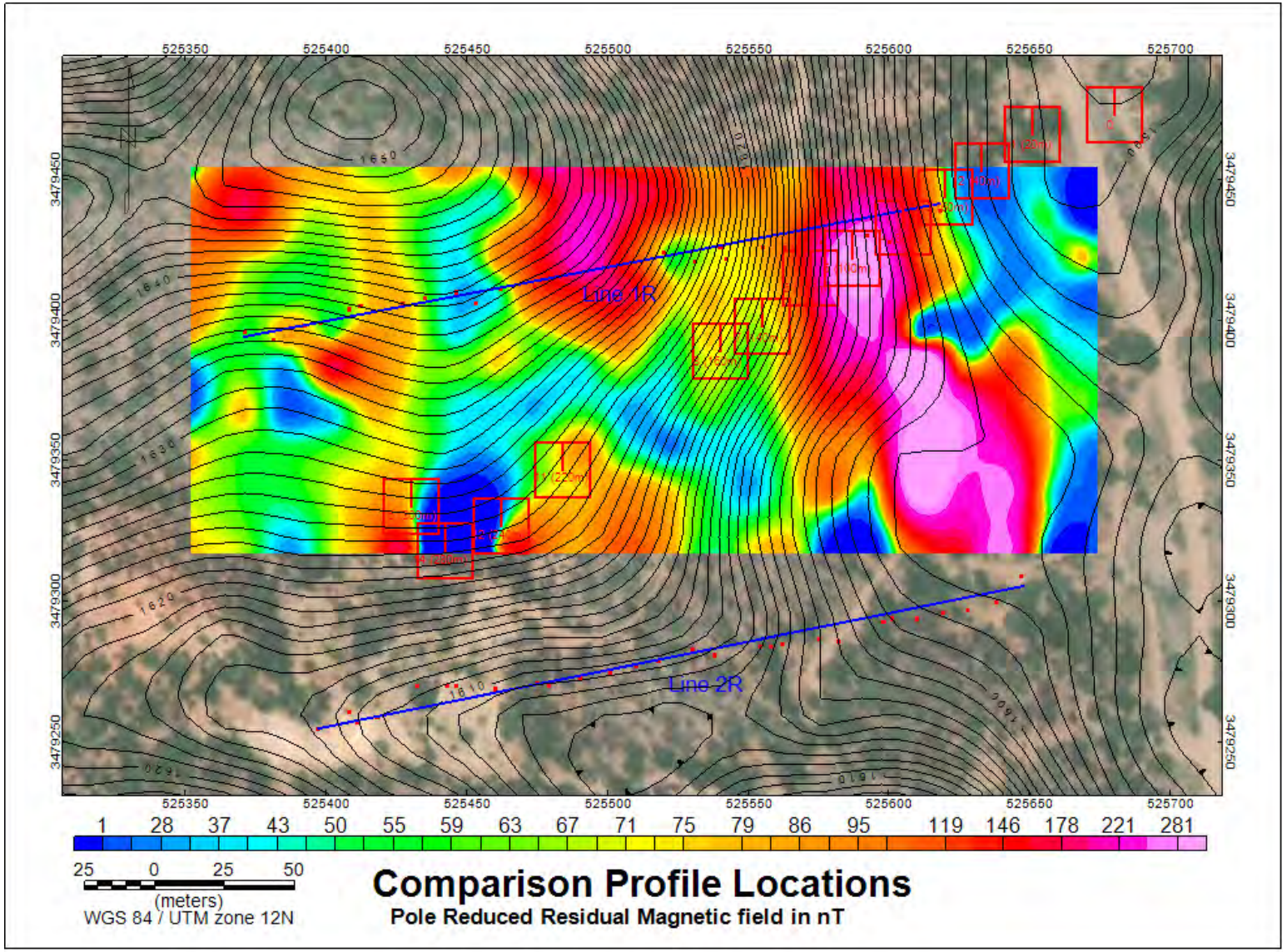

Figure 8.1. Map showing relative locations of ground magnetic survey (interpolated rectangle), DC resistivity surveys (blue lines), and 20 m TEM survey (line of red squares).

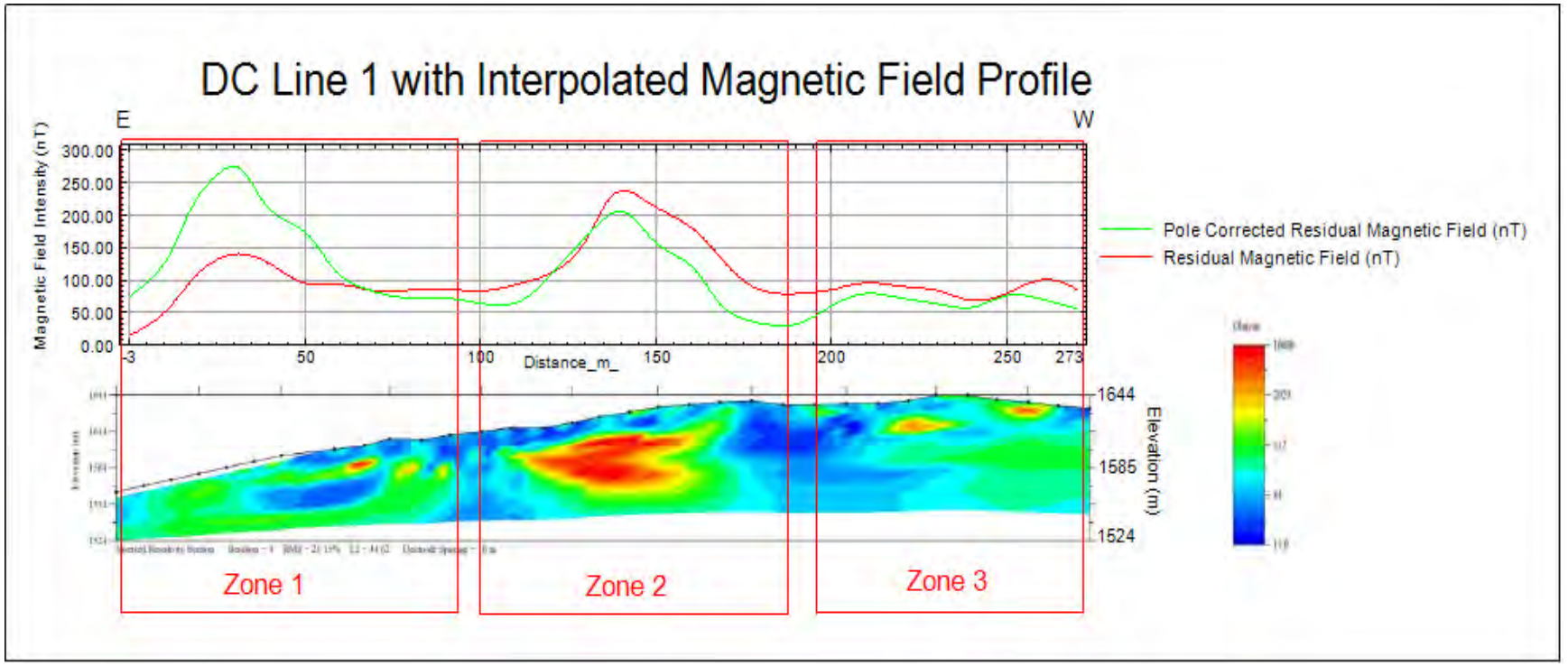

Figure 8.2. Comparison between magnetic survey data (top) and DC resistivity Line 1 (bottom). Magnetic survey data has been interpolated for both residual and pole corrected anomaly plots such that it aligns with the location of DC Line 1.

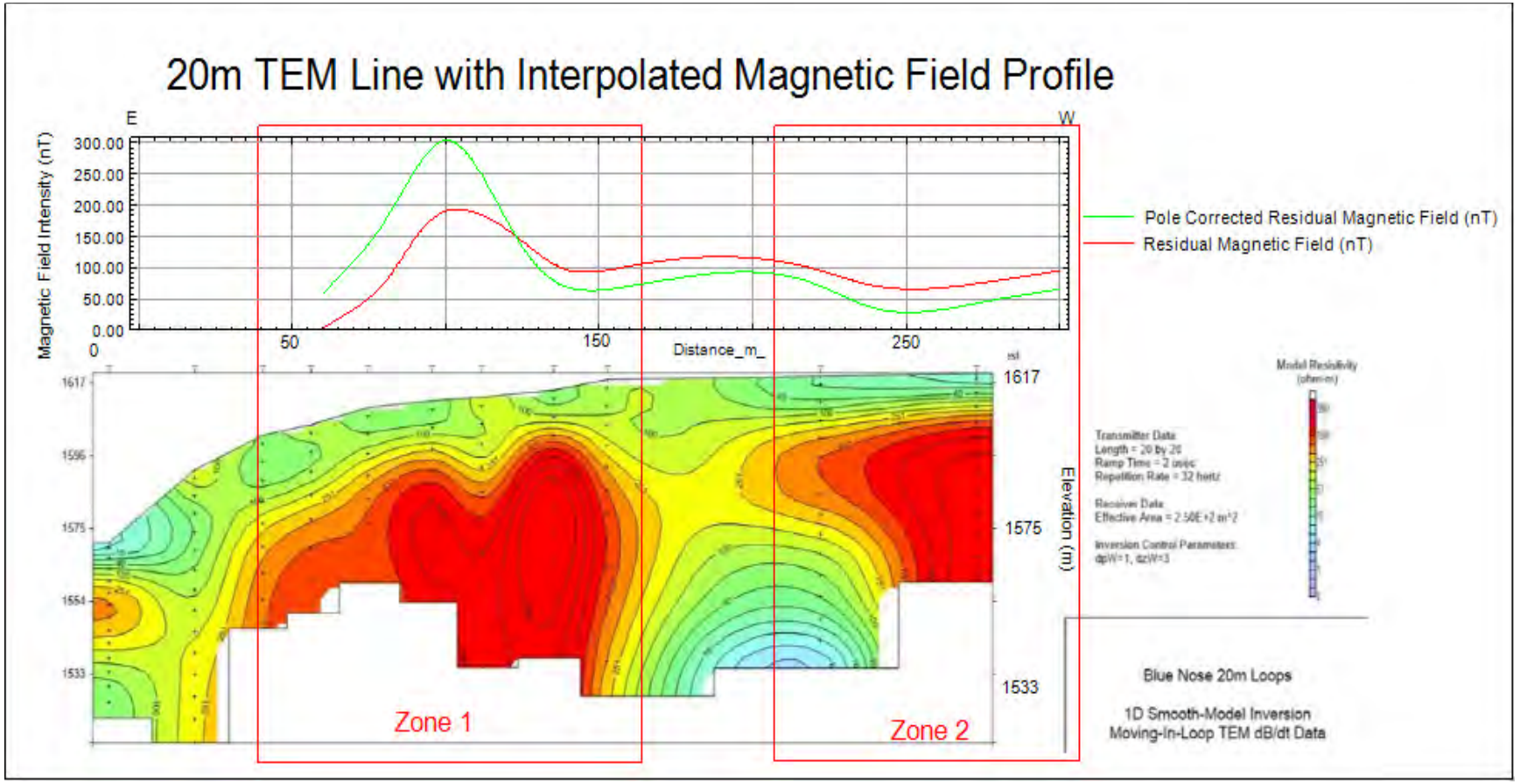

Figure 8.3. Comparison between magnetic survey data (top) and 20 m TEM survey (bottom). Magnetic survey data has been interpolated for both residual and pole corrected anomaly plots such that it aligns with the location of the 20 m TEM loop transect.